Search for age-dependent transcriptomic and epigenetic changes in murine cerebral endothelial cells

Dissertation

der Mathematisch-Naturwissenschaftlichen Fakultät

der Eberhard Karls Universität Tübingen

zur Erlangung des Grades eines

Doktors der Naturwissenschaften

(Dr. rer. nat.)

vorgelegt von

Kshitij Mohan

aus Deoghar, Indien

Tübingen

2020

Gedruckt mit Genehmigung der Mathematisch-Naturwissenschaftlichen Fakultät der Eberhard Karls Universität Tübingen.

Tag der mündlichen Qualifikation:	30.07.2020
Dekan:	Prof. Dr. Wolfgang Rosenstiel
1. Berichterstatter:	Prof. Dr. Alfred Nordheim
2. Berichterstatter:	Prof. Dr. Patrick Müller

यत्प्रज्ञानमुत चेतो धृतिश्च यज्ज्योतिरन्तरमृतं प्रजासु ।
यस्मान्न ऋते किञ्चन कर्म क्रियते तन्मे मनः शिवसङ्कल्पमस्तु ॥

"The mind, that manifests itself in the forms of knowledge,
thought and patience;
The indestructible mind, that is present as a guiding light in all the humans;
That mind, without which no work can be accomplished;
May that, my mind, be pure and full of benevolence.**"**

~ Yajurveda

Declaration

I, Kshitij Mohan, declare that all the work presented in the thesis has been performed by me under the supervision of Prof. Dr. Alfred Nordheim at the Interfaculty Institute of Cell Biology (IFIZ), University of Tübingen between September 1, 2015 and December 31, 2019. Wherever contributions of collaborators and colleagues are involved, every effort has been made to indicate this clearly at the end of the thesis in **Appendix A : Contributions**, with due acknowledgement of the collaborative research undertaken with various research groups. This thesis has been written by me and is a bona fide record of the original work done by me. This work has not been submitted in part or in full for a degree, a diploma or a fellowship to any other university or institute. All sources listed in the thesis have been included in **Bibliography**.

Abstract

Intracerebral hemorrhage (ICH) is associated with disruption of the blood-brain barrier (BBB) and rupture of blood vessels, leading to the leakage of blood into brain. In humans, increasing age is the biggest risk factor for ICH, with people above the age of 75 years being at the highest risk of developing the disease. Other risk factors for ICH include hypertension and cerebral amyloid angiopathy. Although hemorrhagic stroke is a leading global cause of death and disability, the mechanisms leading to blood-brain barrier dysfunction with age and development of ICH is poorly understood. The endothelial cells (ECs) constitute the core component of the BBB in the central nervous system vasculature and provide a physical barrier due to the presence of tight junctions, adherens junctions and basement membrane. This study in wild-type mice and mice having floxed, yet non-recombined *Srf* and *Mrtf* alleles, thereby having functional *Srf* and *Mrtf* genes (wild-type phenotype), demonstrates increased incidents of bleeding in brain with increasing age. Transgenic Cdh5-mT H2B-GFP mice were used to isolate pure population of ECs and RNA-seq was used to study the mRNA expression levels in ECs isolated from murine brains of increasing age – 2, 6, 12, 18 and 24 months. Linear regression analysis performed on the RNA-seq data reveal age-dependent dysregulation of 1388 genes, including many responsible for the maintenance of BBB and vascular integrity. However, no significant age-dependent changes in the expression levels of *Srf* and *Mrtf*, encoding two cooperating transcription factors whose endothelial knockout had previously been shown to cause hemorrhagic stroke-like symptoms, were observed. As epigenetic mechanisms are known to regulate gene expression, age-dependent changes at the CpG methylation and chromatin structure were investigated in this study. Reduced representation bisulfite sequencing (RRBS) was used to investigate change in CpG methylation with age. Interestingly, the older mice (18 months-old) show increased average CpG methylation. However, only two 1000 bp tiles annotated to *Arid5b* and *Adgrg1* genes show a significant age-dependent change in methylation level, with both the tiles showing decrease in methylation with age. Assay for transposase-accessible chromatin sequencing (ATAC-seq) performed to investigate changes at the level of chromatin structure reveals approximately 2290 peaks that undergo age-dependent changes in the chromatin structure with a majority of the peaks (2013) closing with age. Comparing RNA-seq and ATAC-seq data reveals 27 peaks associated with 25 genes that show a correlation between age-dependent changes in chromatin structure and changes in gene expression. The study finds

a strong age-dependent downregulation of the apelin receptor (*Aplnr*) gene, known to play a crucial role in positive regulation of vasodilation and implicated in vascular health. Also, the promoter of *Aplnr* gene shows an age-dependent reduction in chromatin accessibility as revealed by the ATAC-seq data. Interestingly, the study demonstrates an age-dependent reduction in the expression levels of apelin receptor protein in the brain, thereby suggesting a potential association of apelin receptor with increased risk of intracerebral hemorrhage.

Zusammenfassung

Intrazerebrale Hämorrhagien (ICH) sind assoziiert mit der Beeinträchtigung der Blut-Hirn-Schranke (BBB), sowie dem Bruch von Blutgefäßen, welches zum Austreten von Blut ins umliegende Gewebe verursacht. Der größte Risikofaktor in Menschen für ICH ist eine fortschreitende Alterung. Menschen ab einem Alter von 75 Jahren haben das höchste Risiko an ICH zu erkranken. Weitere Risikofaktoren sind Hypertonie und die Zerebrale Amyloidangiopathie. Trotz, dass hämorrhagische Schlaganfälle zu den weltweit führenden Ursachen für Behinderungen und dem Tod gehören, sind die Mechanismen welche zur altersbedingten Beeinträchtigung der BBB und final zu ICH führen, schlecht verstanden. Die Kernkomponente der BBB im zentralen Nervensystem (ZNS) wird durch Endothelzellen (ECs) gebildet, welche eine mit Hilfe von *tight*- und *adherence*- *junctions*, sowie der Basalmembran eine physikalische Barriere ausbilden. Diese Studie verwendet wildtypische Mäuse, sowie Mäuse mit einem gefloxten, nicht rekombinierten *Srf* and *Mrtf* Allelen welche funktionale *Srf* und *Mrtf* Gene kodieren (wildtypische Phänotypen). Diese Tiere zeigen eine erhöhte Inzidenz an Blutungen im Hirn mit steigendem Alter. Transgene Cdh5-mT H2B-GFP Mäuse im Alter von 2, 6,12 18 und 24 Monaten wurden verwendet um reine zerebrale EC Populationen zu isolieren. Weiterhin wurden die mRNA Expressionslevel dieser EC Populationen mittels RNA Sequenzierung analysiert. Eine lineare Regressionsanalyse wiesen auf eine altersabhängige Dysregulation von 1388 Genen hin. Viele dieser Gene stehen in direktem Zusammenhang mit der Aufrechterhaltung der BBB sowie der vaskulären Integrität. Eine vorherige Studie konnte zeigen, dass ein *knockout* der kooperativen Transkriptionsfaktoren SRF und MRTF zu Hämorrhagien, sowie Schlaganfall-ähnlichen Symptomen führen. Überraschenderweise konnte in der vorliegenden Arbeit keine altersabhängige Verringerung der *Srf* und *Mrtf* Expression beobachtet werden. Epigenetische Mechanismen sind bekannt für die Regulation der Genexpression, sodass auch in dieser Studie der altersabhängige Einfluss der CpG Methylierung und der Chromatinstruktur untersucht wurde. Hierzu wurde die *reduced representation bisulfite sequencing* (RRBS) Methodik verwendet, um altersabhängige Änderung der CpG Methylierung zu analysieren. Interessanterweise zeigten ältere Mäuse (18 Monate alt) eine erhöhte CpG Methylierung. Jedoch konnten nur zwei 1000 Basenpaare (BP) lange Abschnitte, assoziiert mit dem *Arid5b*- und dem *Adgrg1*-Gen, als signifikant altersabhängig im Methylierungsgrad identifiziert werden. Beide Abschnitte zeigen eine verringerte Methylierung mit steigendem Alter. Zur

weiteren Analyse der Chromatin Struktur, wurde der *assay for transposase-accessible chromatin sequencing* (ATAC-seq) durchgeführt. Dieser konnte ungefähr 2290 Peaks identifizieren, welche eine altersabhängige Änderung in der Chromatinstruktur zeigten. Die Mehrheit dieser Peaks (2013) zeigte eine Schließung mit steigendem Alter. Vergleicht man die RNA-seq und die ATAC-seq Datensätze miteinander, so kann ein Zusammenhang von 27 Peaks assoziiert mit 25 Genen identifizieren werden, welche sich altersabhängig ändern, sowie mit einer Änderung der Expression korrelieren. Des Weiteren kann diese Studie eine starke, altersabhängige Runterregulation des Apelin Rezeptor (*Aplnr*) Gens identifizieren, welcher eine essentielle Rolle bei der positiven Regulation der Vasodilatation, sowie bei der vaskulären Gesundheit spielt. Die ATAC-seq Daten konnten weiterhin zeigen, dass der Promotor des *Aplnr* Gens ebenfalls eine altersabhängige Reduktion in der Chromatin Zugänglichkeit zeigt. Zuletzt demonstriert diese Studie eine altersabhängige Reduktion in der Expression des Apelin Rezeptor Proteins im Gehirn. Dies lässt eine Assoziation des Apelin Rezeptors mit einem erhöhten Risiko an intrazerebralen Hämorrhagien vermuten.

Acknowledgements

I would like to express my sincere gratitude to Prof. Dr. Alfred Nordheim, my PhD advisor, for his continuous support, guidance and supervision during my PhD. It has been an honor to be his PhD student. I thank him for his insightful suggestions and incessant motivation at every stage since I joined his lab, which helped me immensely in completing this project. His tremendous knowledge, vast experience and astute mentorship have been of great help to me throughout my PhD.

I would like to thank my Thesis Advisory Committee members Dr. Patrick Müller, Prof. Dr. Ralf Sommer and Prof. Dr. Gáspár Jékely for their insightful comments, valuable inputs and constructive suggestions, which were of great help during all the stages of my PhD.

I thank the International Max Planck Research School (IMPRS) “From Molecules to Organisms” for providing me the opportunity to be a part of the PhD program. I am especially grateful to Dr. Sarah Danes, IMPRS program coordinator, who provided immense help and continuous assistance during my PhD. She assisted me in obtaining a visa for Germany, helped me with the matriculation process at the university and arranged an accommodation during my initial days in Tübingen. Every time I needed any assistance pertaining to administrative or bureaucratic issues in the last four years, she extended her help.

I thank Prof. Dr. Jörn Walter at the University of Saarland for his collaboration on the epigenetic studies involved in the project. Many thanks to Dr. Gilles Gasparoni and Abdulrahman Salhab in Prof. Dr. Jörn Walter’s lab, who played major part in the project by performing the sequencing (RRBS and ATAC-seq), processing and bioinformatic analysis of the data. I express my gratitude to Gilles for personally supervising me with preparing the Reduced Representation Bisulfite Sequencing (RRBS) and Assay for Transposase-Accessible Chromatin Sequencing (ATAC-seq) libraries for sequencing. The sequencing of samples and RRBS data analysis were performed by Gilles. I would like to thank Gilles for performing linear regression analysis on RNA-seq and RRBS data, which provided deep insight into the age-dependent changes in gene expression and methylation levels, respectively. I thank Abdulrahman Salhab for processing the sequencing data, analyzing the ATAC-seq data and integrating the ATAC-seq data with RNA-seq data. I express my earnest acknowledgement to Abdul for his continuous and prompt guidance in helping me interpret the ATAC-seq data and providing the required help with bioinformatics.

The FACS sorting of endothelial cells would not have been possible without the assistance, supervision and support of Dr. Stella Autenrieth, Dr. Kristin Bieber and all the members of the FACS Core Facility at the University Medical Hospital, Tübingen. I sincerely thank and appreciate them for their collaboration. I am grateful to Dr. Robert Geffers and his group at the Helmholtz Centre for Infection Research, Braunschweig for the collaboration on RNA sequencing. I would also like to thank Prof. Dr. Ralf Adams at the Max Planck Institute for Molecular Biomedicine, Münster for providing the transgenic Cdh5-mT H2B-GFP mice. I thank Dr. Stefan Liebner at the Universitätsklinikum Frankfurt for his insightful suggestions in the interpretation of endothelial RNA-seq data on ageing and Dr. Angele Breithaupt for her inputs on histology of brain sections, including performing the Berlin blue staining on mouse brain sections.

My colleagues in the Nordheim lab have contributed immensely to my academic and personal growth. I thank Michael Orlich for his invaluable help in the dissection of mice, preparation of single-cell suspensions from mouse brains and FACS sorting. Besides his inputs and collaboration on the project, he has been a great friend and an excellent company. I thank Dr. Siegfried Alberti for his constant guidance, technical assistance and help in various aspects of the project, especially mice handling and animal facility. I thank Heidemarie Riehle and Anke Biedermann for their wonderful technical support and timely assistance with various crucial issues in the lab. Ivana, Abhishek, Catrin, Moustafa, Cansu and Stella provided invaluable scientific inputs to the project and helped me at all the times. In addition to their suggestions for my project, I also thank them for being great companions in the lab and for all the amazing moments we had together, inside and outside the lab.

I would like to thank my parents and my younger brother Rakshit for being with me at every stage of life and inspiring me to excel. Their constant support, encouragement and motivation throughout my journey as a PhD student kept me going. I would like to express special appreciation for my dearest wife Srishti whose incessant love, unconditional support and unyielding faith in me during the final year of my PhD gave me immense strength to complete the project and write the thesis. I thank you dearest Srishti for being my pillar of strength for the last couple of years.

Contents

3. Results

4. Discussion

Chapter 1

Introduction

Chapter 1

Introduction

1.1 Intracerebral hemorrhage

1.1.1 Incidence and risk factors

Intracerebral hemorrhage (ICH) is caused by the rupture of blood vessels, leading to the leakage of blood into brain parenchyma. It accounts for 10-20% of all the strokes and is the second most common subtype of stroke after ischemic stroke[1]. With 3.4 million new incidents and 3.2 million deaths reported annually, hemorrhagic stroke is a leading global cause of death and disability[2]. ICH has a poor prognosis with the 30-day mortality rate being approximately 50%, of which about half the deaths occur within the first 24 hours of the initial hemorrhage[3]. Those who survive suffer from disabilities and only 12-39% survivors attain full functional recovery[4].

Increasing age is the biggest risk factor for ICH, with people above the age of 75 years being at the highest risk of developing ICH. The incidence of ICH has been reported to be 5.9 per 100,000 in the age group 35-54 years, 37.2 per 100,000 in the age group of 55-74 years and 176.3 per 100,000 in the age group of 75-94 years old[5]. Besides increasing age, other non-modifiable risk factors for ICH include male sex and African or Asian ethnicity[4]. The annual incidence rates for ICH per 100,000 people are 5.9 for men and 5.1 for women in the age group of 35-54 years old, 37.2 for men and 26.4 for women in the age group of 55-74 years, and 176.3 for men and 140.1 for women in the age group of 75-94 years[5].

The other important risk factors for ICH include hypertension (elevated blood pressure), cerebral amyloid angiopathy (CAA), high alcohol consumption and prolonged usage of oral anticoagulants. Hypertension accounts for 60-70% primary ICH incidences and the remaining are caused by CAA[3]. ICH caused as a result of hypertension tends to affect the deeper structures of the brain such as basal ganglia, thalamus, pons and cerebellum, while the CAA-related ICH tends to affect the superficial (lobar) regions[6].

The prevalence of hemorrhagic stroke is highest in the USA with an age-standardized rate of 232-270 per 100,000 persons; and the lowest (<39 per 100,000) in Africa, parts of Latin America, eastern Europe, Middle East and Russia. The southeast Asian countries,

China, Japan and Germany also have a high prevalence of hemorrhagic stroke (127-159 per 100,000). The mortality from hemorrhagic stroke is the lowest (0-32 per 100,000) in the USA, Canada, most parts of the western Europe, Japan, Australia and Russia, which can be attributed to advanced healthcare facilities in the developed countries. Madagascar and Mongolia have the highest mortality rates with age-standardized rate of 190-222 deaths per 100,000[2] (Figure 1.1).

1.1.2 Pathophysiology

ICH is caused by the rupture of small to medium-sized blood vessels having diameter in the range of 100 – 600 µm[7] and is typically a manifestation of cerebral small vessel disease (CSVD). Ageing causes structural, functional and mechanical changes in the walls of small blood vessels, which resemble the alterations in small vessels arising from chronic hypertension[8]. These changes lead to the degeneration of the vascular wall, known as lipohyalinosis; causing development of small aneurysms and microhemorrhages in the deeper structures of the brain[9].

CAA-related ICH is characterized by the deposition of amyloid-beta (Aβ) plaques in the walls of small vessels, causing degenerative changes in the vessel walls. The degeneration of vessel walls due to deposition of Aβ plaques leads to the loss of smooth muscle cells, thickening of the vessel wall, narrowing of the blood vessel, formation of microaneurysms and microhemorrhages[10].

The initial rupture of blood vessel and leakage of blood into brain parenchyma causes the formation of solid lump of blood clot called hematoma, which causes direct mechanical injury to the adjacent brain parenchyma within minutes[11]. After the initial hemorrhage, the volume of hematoma increases more than 33 percent during the first 24 hours in one-third of the patients[12]. The expanding hematoma leads to increased intracranial pressure and results in direct injury to the surrounding brain parenchyma, leading to neurological deterioration. The severity of neurological deterioration depends on the location of hematoma, initial hematoma volume and the rate at which hematoma subsequently expands[13].

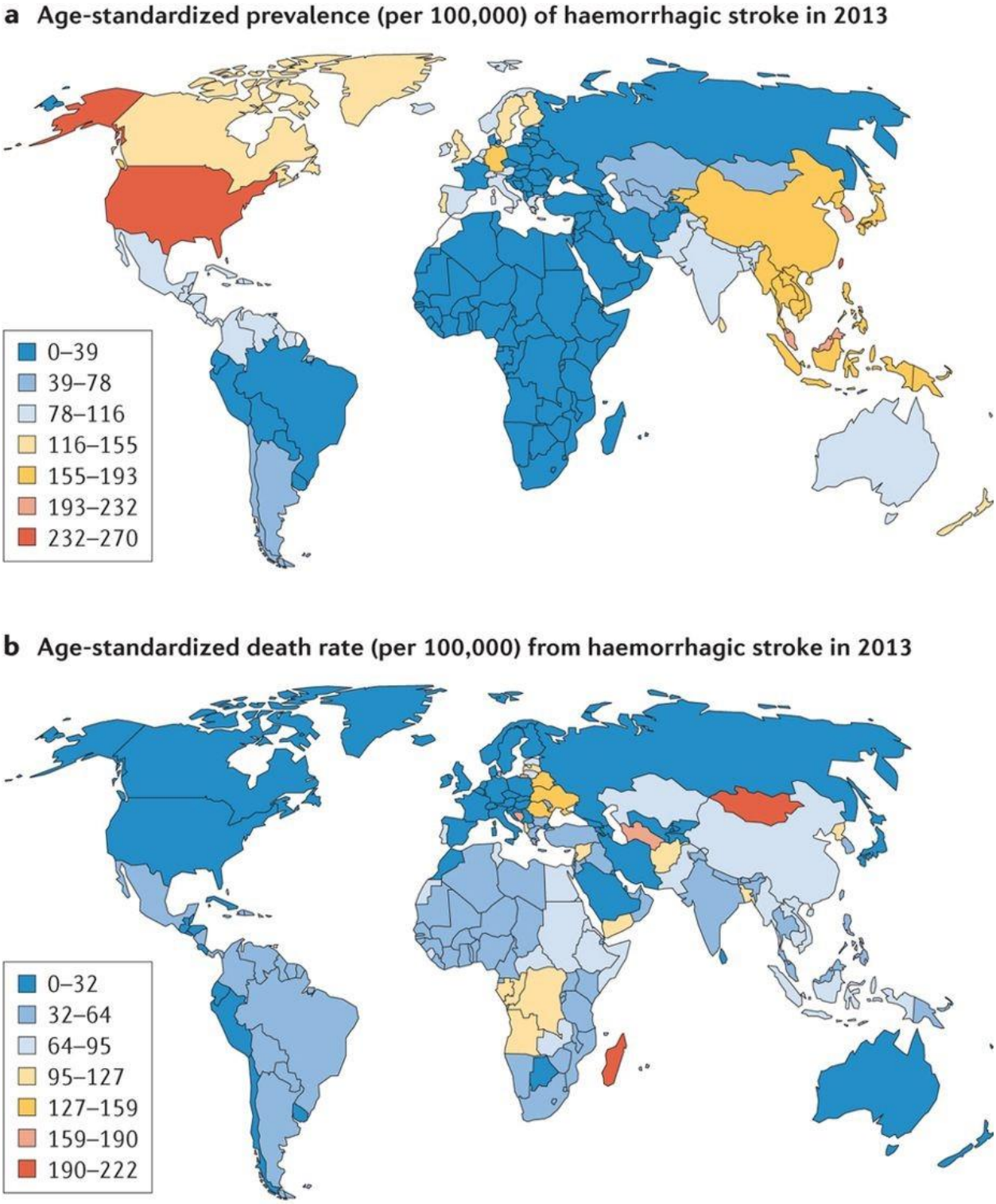

Figure 1.1 | Prevalence of hemorrhagic stroke and mortality figures in the world. Reprinted from Feigin et al., 2016[14]

After ICH, extravasated erythrocytes and plasma proteins mediate an inflammatory response and activate the coagulation cascade resulting in severe cytotoxic effects on the adjacent viable brain cells[15]. The lysis of extravasated erythrocytes in the accumulated hematoma leads to the release of cytotoxic hemoglobin and its subsequent degradation products heme and iron. The cytotoxicity of blood, inflammatory response, excitotoxicity and oxidative stress result in the death of brain cells, including the cells of the neurovascular unit[16, 17]. The death of cells constituting the neurovascular unit leads to further irreversible breakdown of the blood-brain barrier, causing perihematomal edema with massive brain cell death. The development of perihematomal brain edema starts within the first three hours of ICH, evolves over the next few days and peaks around 10 to 20 days[11].

1.1.3 Symptoms and diagnosis

The initial symptoms depend on the location and size of hematoma; and may include severe headache, nausea and vomiting due to the increased intracranial pressure. Patients may also have decreased level of consciousness, seizures, stupor, focal or generalized neurological symptoms, indicating ICH involving deeper structures of the brain such as thalamus and brainstem[18]. Since the symptoms and clinical presentations of ICH resemble ischemic stroke, neuroimaging is used to confirm the diagnosis[19].

Non-contrast computerized tomography (CT) scan is the most common neuroimaging method for a definitive diagnosis of ICH, and allows the estimation of hematoma location, hematoma volume, presence of edema surrounding the site of ICH and the development of mass effect[20]. Contrast-based CT may also show the pattern of bleeding and assist in determining the underlying cause of the ICH. Along with conclusive diagnosis, contrast-based CT may be used to predict hematoma expansion by observing the extravasation of the contrast into hematoma[21].

Magnetic resonance imaging (MRI) is equally powerful for the detection of ICH and is a better diagnostic tool to determine the characteristics of perihematomal brain edema. MRI is generally used as a follow-up technique to study perihematomal edema and identify underlying causes of ICH such as cerebral amyloid angiopathy (CAA), arteriovenous malformations (AVM) or tumor[22].

Additionally, computerized tomography angiography (CTA) is performed in appropriate cases to diagnose ongoing bleeding in the brain and evaluate vascular abnormalities such as aneurysms or AVM[23].

1.1.4 Management and treatment

ICH is a medical emergency and requires immediate intervention as delays in treatment result in worse prognosis. Patients with ICH often present with stupor or unconsciousness and are unable to protect the airway. Initial intervention requires urgent airway management, including endotracheal intubation and mechanical ventilation, in unconscious patients[24].

High blood pressure, common in patients suffering from ICH, is associated with increase in hematoma volume. An elevation of systolic blood pressure more than 140 mm Hg after ICH doubles the risk of death or disability, and hence monitoring and management of blood pressure is critical after ICH[25]. The American Heart Association/American Stroke Association (AHA/ASA) guidelines for blood pressure management in ICH patients recommend careful management of severely elevated blood pressure with continuous intravenous infusion of drugs such as labetalol, esmolol, enalapril, hydralazine or nicardipine to reduce blood pressure. The AHA/ASA recommends aggressive blood pressure reduction with the monitoring of blood pressure every five minutes if the systolic blood pressure in ICH patients is more than 200 mm Hg. In ICH patients with systolic blood pressure more than 180 mm Hg with no evidence of increased intracranial pressure, the AHA/ASA guidelines recommend reducing the systolic blood pressure to 160 mm Hg[26].

A critical step in the management of ICH involves prevention of continued bleeding[27]. Therapeutic options to arrest intracerebral bleeding include intravenous infusion of Vitamin K, fresh frozen plasma (FFP) and prothrombin complex concentrates (PCCs)[18]. Vitamin K plays an important role in the endogenous synthesis of coagulation factors and is the first line of treatment to control intracerebral bleeding. However, it takes approximately 6 hours for vitamin K to reach therapeutic levels and therefore, FFP or PCCs – that contain all coagulation factors – is infused urgently[28, 29]. The AHA/ASA guidelines recommend prompt intravenous infusion of Vitamin K (5 – 10 mg) administered slowly over 30 minutes in combination with FFP or PCCs[18, 26].

In patients with ICH involving severe neurological deterioration, brainstem compression and hydrocephalus, surgical evacuation of hematoma may be beneficial[30]. A large phase III clinical trial – the Surgical Trial in Intracerebral Hemorrhage (STICH) – compared the surgical evacuation of hematoma with non-surgical conservative treatment for patients and demonstrated that surgical hematoma evacuation provided no significant benefit in the outcome[31].

1.2 Blood-brain barrier

The human brain has an immensely high energy requirement, accounting for approximately 20% of the total oxygen metabolism at resting state[32]. The high metabolic demands of the brain require adequate oxygen and nutrients, which is achieved through an extensive, dense and well-regulated vascular network. While facilitating instantaneous delivery of nutrients and oxygen according to the energy demands of brain, the blood vessels of the central nervous system (CNS) possess unique properties of forming a heavily restricting barrier – known as the blood-brain barrier (BBB) – between the circulating blood and the brain[33]. The highly selective BBB plays an important role in brain homeostasis by tightly regulating paracellular and transcellular transport of ions, macromolecules, pathogens and cells of the immune system between blood and brain.

The BBB is present at all levels of the vasculature in the brain – the penetrating arterioles and arteries, the dense capillaries, and the draining venules and veins – protecting the CNS from pathogens, toxins and infiltration of immune cells into the healthy brain[34]. However, the capillary endothelium comprises the largest surface area of the blood-brain barrier since the length of capillary accounts for more than 85% of the total length of the blood vessel in the CNS[35, 36]. The regulation of cerebral blood flow (CBF) and the maintenance of BBB in the cerebral capillaries is achieved by various cellular and non-cellular components that together form the neurovascular unit (NVU). The NVU primarily comprises of a continuous monolayer of endothelial cells (ECs) that form the innermost wall of the blood vessels, pericytes that wrap around the ECs, basement membrane (BM) which surrounds the vascular tube, astrocytes whose end-feet cover the vasculature, and neurons (Figure 1.2)[37].

1.2.1 Endothelial cells

The endothelium monolayer forming the innermost wall of the cerebral blood vessels constitutes the core component of the BBB[35]. The lumen of large arteries and veins in the CNS are made up of several ECs connected to each other whereas the inner cellular lining of a cerebral capillary is made up of a single EC folding on to itself[38]. The ECs of CNS differ from the ECs in other tissues as they have continuous tight junctions (TJs) that form a physical barrier, preventing paracellular movement of molecules, cells and microbes across the EC layer in brain. The presence of continuous tight junctions in the BBB ECs impart them a very high electrical resistance of 1500-2000 $\Omega.cm^2$ in comparison to 3-33 $\Omega.cm^2$ in ECs in other tissues[39]. The CNS ECs also lack fenestrations and exhibit very low rate of transcytosis, which restricts the transcellular movement of molecules across the EC layer[40]. Another key property of the ECs in CNS is their extremely low expression of leukocyte adhesion molecules on their surface when compared to the ECs in other tissues. This provides additional barrier property to the blood vessels in the brain by strongly restricting the entry of immune cells into the CNS[38, 41]. The ECs in cerebral capillary express strong cellular polarity with distinct luminal and abluminal membrane transporters that regulate the movement of biomolecules between blood and brain[42, 43].

A

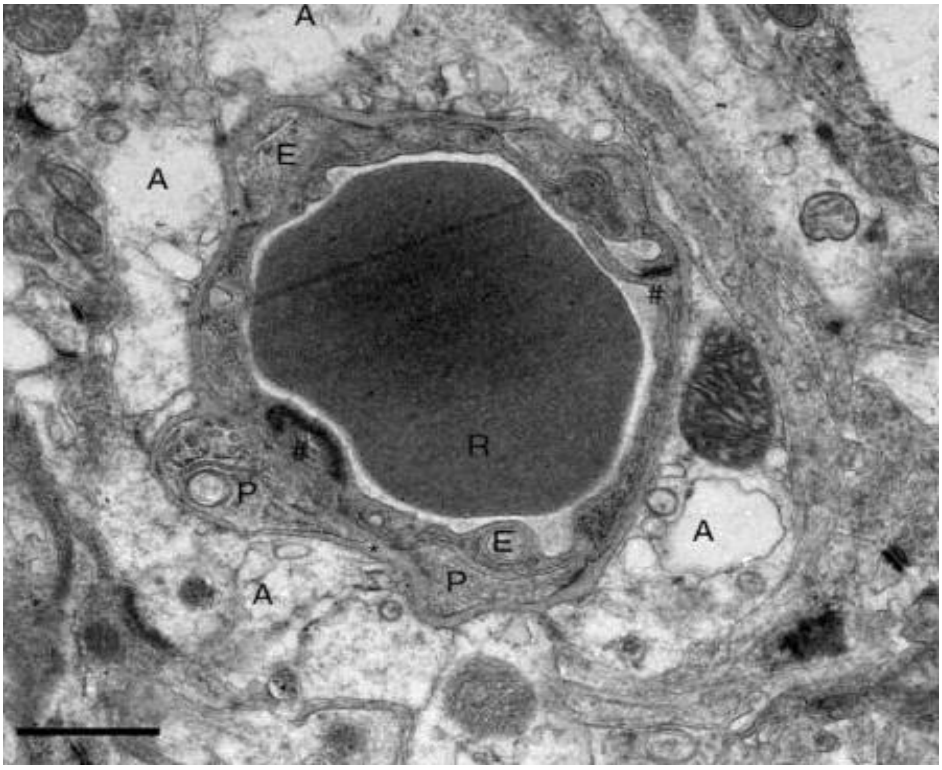

B

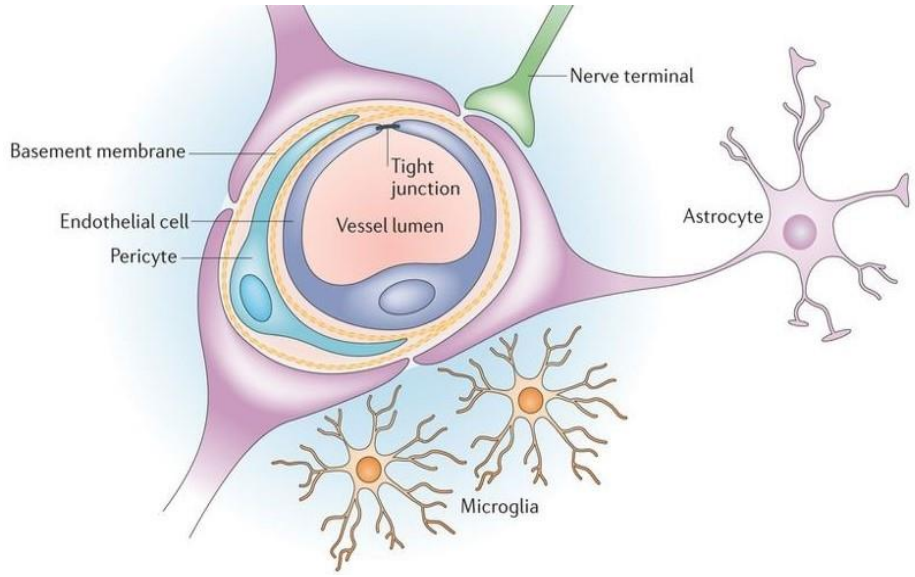

Figure 1.2 | The Neurovascular unit. A) Electron microscopic image of the neurovascular unit (NVU) in a brain capillary of an adult mouse. The symbols represent Astrocyte (A), Endothelial Cell (E), Pericyte (P), Erythrocyte (R), Tight Junction (#) and Basement Membrane (*). Scale bar 1µm. Reprinted from Vallon et al., 2014[44]. **B)** Schematic representation of the neurovascular unit and its cellular components. Reprinted from Leinenga et al., 2016[45].

1.2.2 Transport across the ECs

The movement of biomolecules across the ECs is very strongly regulated. The presence of continuous tight junctions between the ECs restrict the paracellular transport of lipophobic molecules. Small gaseous molecules such as oxygen and carbon dioxide, and small-sized solutes with a high lipid solubility passively diffuse through the cell membrane and cross the endothelium down their concentration gradient.

The CNS ECs show polarized expression of specific transporters present in the luminal and abluminal membrane of the cerebral ECs that facilitate the transport of nutrients, amino acids, proteins, nucleosides and other biomolecules from blood to brain; and remove waste products from the CNS into the blood[46]. The transporters may be passive, transporting the molecules down the concentration gradient, or active, transporting the molecules against their concentration gradient. These transporters include various proteins of the solute carrier (SLC) family that regulate the transport of polar solutes such as nutrients, amino acids, ions and nucleosides to the brain; and the proteins of ATP-binding cassette (ABC) transporter family to move biomolecules against a concentration gradient by utilizing the energy of adenosine triphosphate (ATP)[47]. The ABC family of transporters expressed in the ECs of the CNS include the multidrug resistance-associated proteins (MRPs) and P-glycoprotein (Pgp) that pump out toxic biomolecules present in the circulating blood that may passively diffuse into the ECs from blood[48].

Peptides and proteins such as insulin, transferrin, amyloid-beta, leptin, lipoproteins, glycosylated proteins and other macromolecules move across the BBB via receptor-mediated transcytosis. Plasma proteins such as albumin are transported across the BBB ECs via adsorptive transcytosis. The CNS ECs exhibit a very poor rate of adsorptive transcytosis but cationization of the macromolecules increases the uptake of albumin and other plasma proteins by the ECs. The important routes of molecular traffic across the blood-brain barrier is summarized in Figure 1.3.

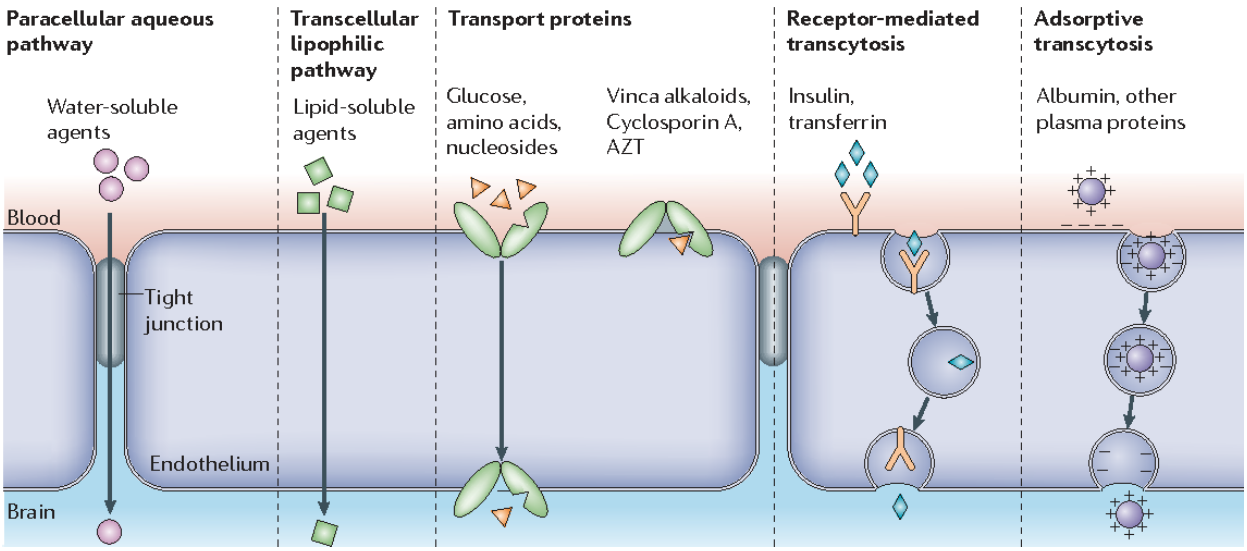

Figure 1.3 | Pathways across the blood-brain barrier. The schematic diagram shows important routes of molecular traffic across the blood-brain barrier. The tight junctions form a physical barrier and severely restrict the paracellular transport across the BBB. The ECs in the CNS contain transporters that move various molecules across the BBB. These transporters include various proteins of the solute carrier (SLC) family that regulate the transport of polar solutes such as nutrients, amino acids, ions and nucleosides to the brain; and the proteins of ATP-binding cassette (ABC) transporter family to move biomolecules against a concentration gradient by utilizing the energy of adenosine triphosphate (ATP). Another key pathway across the BBB involves receptor-mediated endocytosis and transcytosis of proteins such as insulin and transferrin. Reprinted from Abbott et al., 2006[37]

1.2.3 Molecular components of the blood-brain barrier

1.2.3.1 Tight Junction

CNS ECs are connected to each other by continuous tight junction (TJ) complexes localized along the lateral membrane that seal the interendothelial cleft and form a high-resistance physical barrier[49]. TJs strongly restrict the paracellular movement of molecules, cells and microbes across the EC monolayer in the brain and form the primary molecular component of the BBB. The TJ complex is composed of transmembrane proteins that form strong adhesion complexes between adjacent ECs via homophilic or heterophilic interaction; and are linked to the actin cytoskeleton through their interaction and association with various cytoplasmic adaptor proteins that play a crucial role in intracellular signal transduction. The actin cytoskeleton forms a key component of the TJ complex as it provides the necessary physical support to the TJ complex[50].

The transmembrane proteins of the TJ complex include claudins and occludin, which are integral membrane proteins; and junction adhesion molecules (JAMs), that are cell adhesion molecules belonging to the immunoglobulin superfamily[51] (Figure 1.4) . Claudins are the main barrier-forming proteins and constitute the primary structural component of the endothelial TJ complex[49]. More than 25 isoforms of claudin have been identified in mouse and human, with each isoform showing tissue-specific expression[52, 53]. All the claudins have similar structure, which include a tetraspanning transmembrane region, two extracellular loops and two cytoplasmic termini – a very short N-terminus and a longer C-terminus[54]. Claudin-5 is the major claudin expressed in the CNS ECs, but claudins 1, 3 and 12 are also expressed in the ECs of brain microvessels[55, 56]. The transcript levels of claudin-5 is about 600-fold higher than the levels of claudins 1, 3 or 12 in brain microvessels[57, 58]. Recently, the presence of claudins 4, 11, 20 and 25 have also been established at the BBB in human microvessels[59].

Claudin-5 deficient mice (*Cldn5*$^{-/-}$) show post-natal lethality and die within 10 hours of birth. The *Cldn5*$^{-/-}$ mice display normal vasculogenesis during embryonic development, lack any vascular abnormalities and do not exhibit any bleeding or edema in the brain at birth when compared to the wild-type mice. However, *Cldn5*$^{-/-}$ mice have a severely compromised BBB as established by tracer experiments and MRI.

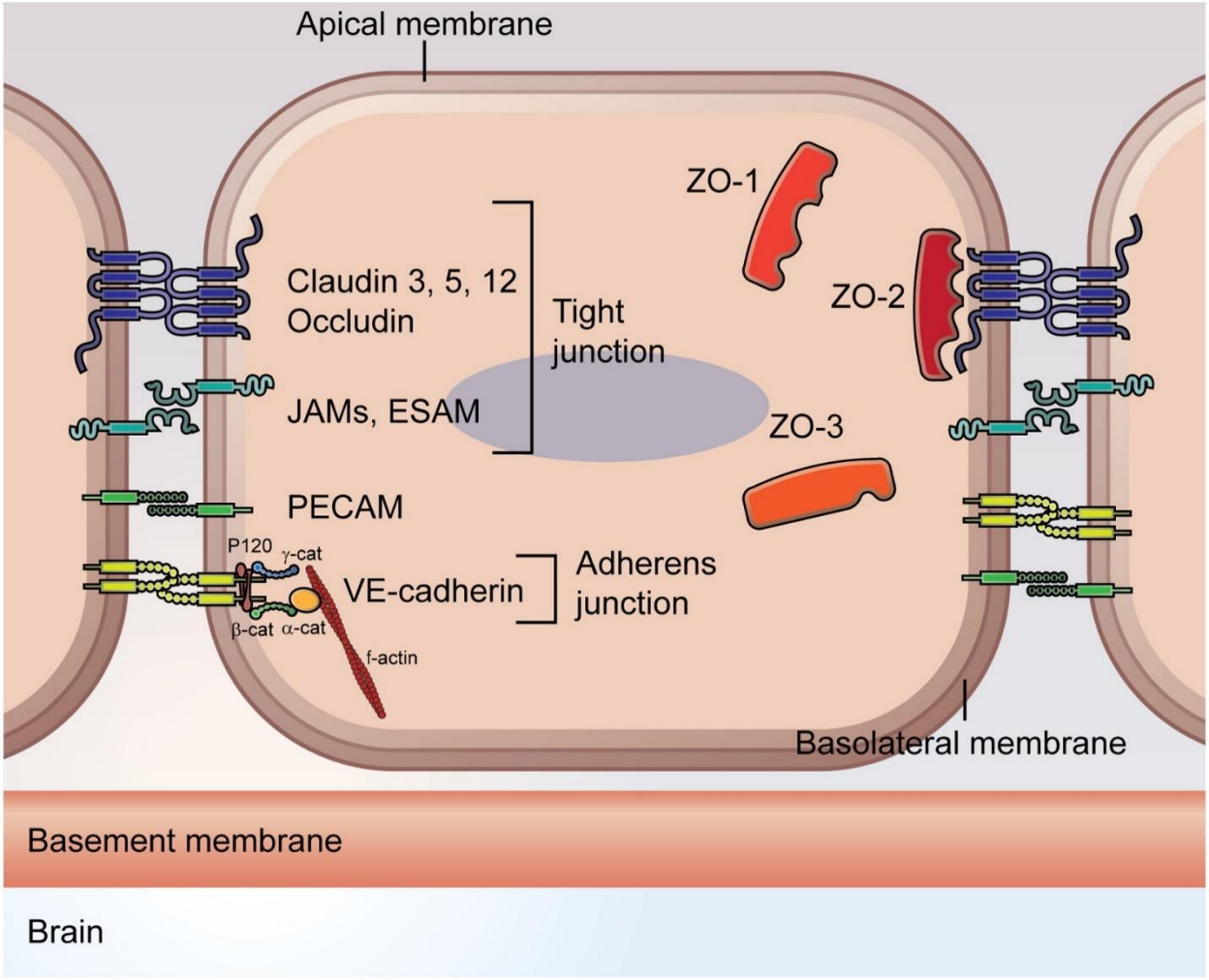

Figure 1.4 | Molecular composition of the CNS endothelial cell-cell junction. The endothelial cell-cell junction in the CNS is primarily composed of tight junction, of which the claudins and occludin are the major structural constituents. Junction adhesion molecules (JAMs) and endothelial selective adhesion molecule (ESAM), which belong to the immunoglobulin superfamily, are known to play a key role in the formation and maintenance of TJs. VE-Cadherin, β-Catenin and p120 form the adherens junction complex. Beside various transmembrane components of the BBB, a number of scaffolding proteins such as ZO-1, -2, and -3 provide structural integrity to various junction complexes. Reprinted from Claudio et al., 2016[60]

The *Cldn5*$^{-/-}$ mice display size-selective impairment of the BBB integrity. While the molecules up to a size of approximately 800 Daltons cross the BBB in *Cldn5*$^{-/-}$ mice, larger molecules are still unable to cross the BBB[56]. Greene et al. (2017) generated inducible claudin-5 knockdown mice, where expression of claudin-5 was suppressed in the BBB of adult mice. Continuous suppression of claudin-5 expression in adult mice severely affected the lifespan and all the mice died within 40 days. These inducible claudin-5 knockdown mice also display hampered learning, seizures and a compromised BBB[61].

Occludin is a transmembrane protein and a key component of the TJ complex in the cerebral ECs. Occludin was identified as the first component of the TJ complex and is highly expressed in the ECs of CNS as compared to the ECs in other tissues[58, 62]. Occludin has a tetraspanning transmembrane domain, two extracellular loops of equal length that mediate cell-cell interaction, a short cytoplasmic N-terminus, and a long cytoplasmic C-terminus which interacts with cytoplasmic adaptor proteins and cytoskeleton[63]. Occludin deficient mice (*Ocln*$^{-/-}$) have normal TJ complex and display an intact BBB. Moreover, occludin does not form TJ complexes on its own and is predominantly associated with claudin-5 based strands, indicating a regulatory role of occludin in stabilizing the TJ complex[63, 64].

The junctional adhesion molecules (JAMs) – JAMs A, B, C and endothelial cell-selective adhesion molecule (ESAM) – are the third group of transmembrane proteins of the TJ complex in the CNS ECs[65]. JAMs are cell adhesion molecules belonging to the immunoglobulin superfamily, consisting of a single membrane-spanning domain, an IgG-like extracellular domain, an extracellular N-terminus that plays a crucial role in dimerization and a cytoplasmic C-terminus that interacts with the TJ scaffold proteins[66]. The JAMs contribute towards adhesion between cells via both homophilic and heterophilic interactions, and are principal molecules implicated in the establishment and stabilization of TJ complexes via association with cytoplasmic TJ adaptor proteins[67, 68]. ESAM is a recently discovered transmembrane protein specifically expressed at the TJ complex and has a similar structure to JAMs. ESAM plays an important role in endothelial cell-cell interaction during vascular development. ESAM is critical for the extravasation at TJs and *Esam*$^{-/-}$ mice displayed reduced leukocyte extravasation[69].

The cytoplasmic adaptor proteins at the TJs constitute a large protein complex, which forms structural connections with the transmembrane TJ proteins on one side and the actin

cytoskeleton in the cytoplasm. These TJ scaffolding proteins can be broadly divided into PDZ-containing and PDZ-lacking proteins depending on the presence or absence of PDZ domain[70]. The PDZ-containing proteins have one or more PDZ domains that interact with the C-termini of transmembrane proteins, cytoplasmic proteins and PDZ domains of other proteins. The PDZ-containing scaffolding proteins, via their PDZ domains, associate with the C-termini of the transmembrane proteins and play a crucial role in clustering and anchoring of transmembrane proteins[65, 71]. The presence of PDZ domains in these proteins impart them their characteristic scaffolding properties, bringing together the cytoskeleton, signaling and integral proteins[72]. The principal TJ PDZ-containing scaffolding proteins include proteins of membrane associated guanylate kinases (MAGUK) family (ZO-1, ZO-2, ZO-3), partitioning defective proteins (Par3 and Par6) and afadin[71, 73].

The Zonula occludens-1, 2 and 3 (ZO -1, 2, 3) proteins, also known as tight junction proteins (TJPs) are key cytoplasmic components of the TJ complex at the BBB[74, 75]. In cerebral ECs, ZO-1 associates with transmembrane proteins through various PDZ domains it contains and mediates stabilization of TJs. ZO-1 associates with the claudins via PDZ1, JAM-A through its PDZ3 domain and occludin via GUC domain. The ZO-1 protein also forms a homodimer or a heterodimer with ZO-2 via PDZ2 domain[76, 77]. The C-terminus of ZO-1 contains the actin-binding region via which it associates with the actin cytoskeleton and regulates signal transduction[75, 77]. ZO-1 also plays an important role in stabilizing adherens junction, angiogenesis and barrier formation in ECs[78]. ZO-2 is structurally similar to ZO-1 and it imparts stability to the TJ by interacting with claudins, occludin and actin cytoskeleton[65, 79].

The partition defective proteins Par3 and Par6 play an important role in establishing polarity in the cerebral ECs and establishment of junction complexes at the BBB. Afadin, another key component of the cytoplasmic plaque, binds to ZO-1, JAM-A and actin-binding proteins, and is crucial for the assembly of tight junction and adherens junction at the BBB. Some other cytoplasmic proteins of the TJ complex in the CNS ECs include disk large homolog 1 (DLG1) and membrane protein palmitoylated 1, 5 and 7 (MPP1, 5 and 7). However, their functions and roles in the cerebral ECs have not been fully established.

The PDZ-lacking cytoplasmic components of the junctional complex in the CNS ECs include cingulin, Rab3, Rab13, RhoA, PKCλ, PKCζ, heterotrimeric G protein, junction associated coiled-coil protein (JACOP) and 7H6[65, 70]. Cingulin is involved in anchoring the TJ

complex proteins to actin cytoskeleton and regulates the stability of TJs[80]. The Rab proteins play an important role in assembly and remodeling of the TJ; and regulates docking and fusion of transport vesicles at the TJ in CNS ECs[55]. Other cytoplasmic proteins associated with the TJ complex include RhoA, PKCλ, PKCζ, heterotrimeric G proteins and junction associated coiled-coil protein (JACOP), which mediate various signaling pathways to regulate the assembly and maintenance of junctional complexes at the BBB[65].

1.2.3.2 Adherens Junction

Adherens Junctions (AJs) are organizationally similar to the TJ and form another major component of the junctional complex contributing towards the BBB[49]. The AJ complex in the CNS ECs consist of cadherins, which are transmembrane proteins responsible for endothelial cell-cell adhesion, and cytoplasmic scaffolding proteins that associate with cadherins and interact with actin cytoskeleton of the ECs to regulate signal transduction[81] (Figure 1.4).

Cadherins are transmembrane proteins that mediate Ca^{2+}-dependent cell-cell adhesion through homophilic interaction with cadherin molecules present on the adjacent cell. The primary cadherin in the CNS ECs is vascular endothelial cadherin (VE-Cadherin). Besides VE-Cadherin, CNS ECs also express lower amounts of neuronal cadherin (N-Cadherin) and epithelial cadherin (E-Cadherin)[82]. Mice lacking VE-Cadherin (*Cdh5*$^{-/-}$) display defective vascularization and die by embryonic day 11.5 (E11.5)[83]. Although *Cdh5*$^{-/-}$ mice have normal de novo blood vessel formation at E8.5, the vessels disassemble by E9.5 leading to impaired angiogenesis and a severely compromised vasculature. The *Cdh5*$^{-/-}$ mice exhibit compromised organization and death of ECs in cerebral blood vessels, suggesting that VE-Cadherin is crucial for the survival of the ECs, angiogenesis, and maintaining stability of the newly formed blood vessels[84, 85]. Transgenic mice with EC- specific deletion of N-Cadherin (*Cdh2*) display impaired vasculature and are embryonic lethal. These mice also show reduced expression of VE-Cadherin in the endothelium, suggesting a critical role of N-Cadherin in vascular morphogenesis[86].

The cytoplasmic plaque of AJ mediates the interaction between VE-Cadherin and actin cytoskeleton, and comprises of proteins belonging to catenin family, primarily β-catenin, plakoglobin (γ-catenin), α-catenin and p120[49]. The cytoplasmic domain of VE-Cadherin associates with β-catenin and p120 which are linked to α-catenin and afadin, which, in turn,

mediate the link to actin cytoskeleton. VE-Cadherin also mediates the link to intermediate filaments through associating with plakoglobin (γ-catenin)[49, 87].

1.2.3.3 Cytoskeleton

The cytoskeleton is primarily composed of actin filaments, intermediate filaments and microtubules. It constitutes an important structural component of the BBB and has a crucial role in the establishment and maintenance of junctional integrity in the cerebral ECs[88, 89]. The change in the organization of the actin cytoskeleton lead to change the tensile strength of the ECs, thereby affecting the adhesive properties of the junctional complex and resulting in the disruption of barrier properties in ECs[90]. The association of actin filaments with the TJ and AJ complexes, primarily mediated through the association of actin cytoskeleton with ZO-1 and cytoplasmic plaque proteins, is critical for barrier properties of ECs[78, 91, 92] (Figure 1.5). The actin cytoskeleton is a dynamic structure and is regulated via approximately 100 actin-binding proteins which regulate polymerization, depolymerization, cross-linking and organization of the cytoskeleton[65, 93]. Proteins belonging to the Rho family of GTPases – RHOA, RAC and CDC42 – regulate the reorganization of the actin cytoskeleton via more than 60 effector proteins that are downstream of RHOA, RAC and CDC42. While RHOA modulates the reorganization of stress fibers, RAC1 and CDC42 play a role in the reorganization of lamellipodia and filopodia, respectively[94, 95]. Other major actin-binding proteins that are present in cerebral ECs include ARP2/3, cortactin and vasodilator-stimulated phosphoprotein (VASP) that mediate the process of actin polymerization[96, 97].

1.2.3.4 Basement Membrane

The Basement Membrane is a specialized three-dimensional network of extracellular matrix (ECM) that provides structural support to the vasculature in CNS and contributes to the BBB integrity. It is composed of ECM proteins that are synthesized and deposited collectively by the ECs, the pericytes and the astrocytes of the neurovascular unit. The major components of the basement membrane are collagen IV, isoforms of laminin, nidogen and heparan sulfate proteoglycan 2, also known as perlecan[98]. The three-dimensional network of the basement membrane is composed of collagen IV and laminin, which self-assemble, and are interconnected by nidogen and perlecan[99].

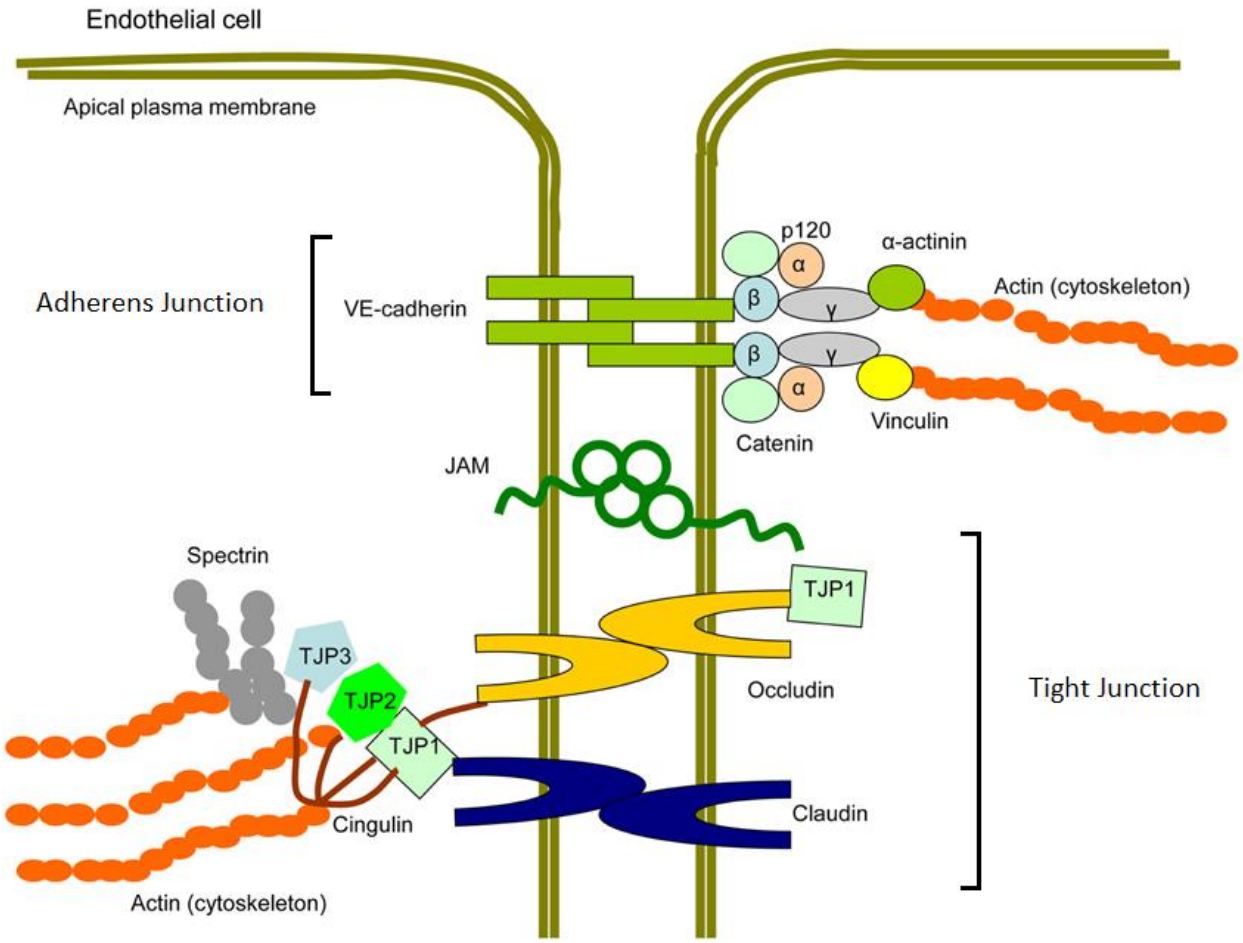

Figure 1.5 | The association of actin filaments with the tight junction and adherens junction complexes. The tight junctions and adherens junctions are linked to the actin cytoskeleton through their interaction and association with various cytoplasmic adaptor proteins. At the adherens junction, VE-Cadherin is associated with β-catenin, which forms a complex with p120, α-catenin, plakoglobin and α-actinin, linking it to the actin cytoskeleton. The association of transmembrane tight junction claudins and occludins with actin cytoskeleton is mediated by cytoplasmic plaque proteins such as the TJPs (also known as ZOs), partitioning defective proteins (Par3 and Par6), afadin and cingulin. The actin cytoskeleton forms a key component of the tight junction and adherens junction complexes as it provides the necessary physical support to the junctions. Reprinted from Chistiakov et al. (2015)[100]

The most abundant component of the basement membrane is collagen IV, with α1 (*Col4a1*) and α2 (*Col4a2*) being the major subunits that together form a heterotrimer in the ratio 2:1, respectively. Mice lacking either *Col4a1* or *Col4a2* have normal deposition and assembly of basement membrane proteins during early development. However, these mice display varying degree of growth retardation, have structural deficiency in the basement membrane and die at E10.5 – 11.5, suggesting that *Col4a1* and *Col4a2* may not be necessary for the initial deposition of ECM, but is critical for the maintenance of basement membrane integrity[101]. Mice having functional mutation in both the alleles of *Col4a1* die around mid-gestation and show disrupted basement membrane. Heterozygous mutant mice having one functional *Col4a1* allele have reduced viability and about 50% die within a day of birth. The heterozygous mutant mice suffer from severe intracerebral hemorrhages and have compromised basement membrane structure[102]. Mutations in *COL4A1* and *COL4A2* genes have been implicated in ICH and cerebral SVDs in human patients as well[103, 104].

Laminins are a cruciform-shaped heterotrimeric protein, composed of α, β and γ chains, and constitute the second major component of the basement membrane. There are five chains of α-laminin, four chains of β-laminin and three chains of γ-laminin, which result in a large number of laminin isoforms[105]. The cells of neurovascular unit secrete different isoforms of laminin. While laminins α4β1γ1 and α5β1γ1 are specific to the ECs of BBB, laminins α1β1γ1 and α2β1γ1 are specifically expressed by astrocytes. Mice deficient for either of α5, β1 or γ1 subunits of laminin are embryonic lethal[106]. Laminin α4 is also critical for the vascular integrity and mice lacking laminin α4 (*Lama4*$^{-/-}$) have leaky vasculature. These mice display impaired microvessel maturation and suffer from hemorrhages during embryonic and neonatal period, but they are viable and reach adulthood[107]. Also, mice lacking laminin α5 specifically in the ECs do not show any defect in the vasculature and are perfectly healthy. This suggests that the normal phenotype of these mice may be a result of potential compensation between laminin α4 and laminin α5 in maintenance of vascular integrity[108].

Nidogens associate with laminins and collagen IV and play an important role in maintaining the structural integrity of the ECM and stabilizing the basement membrane. The most important isoform of nidogen present at the cerebral vasculature is nidogen-1, also known as entactin-1. Mice lacking nidogen-1 are viable and have a normal lifespan but display hampered neuromuscular function such as seizure-like symptoms and loss of muscle control in hind legs. The basement membrane in the cerebral microvessels of these mice show mild

structural alterations, indicating a role of nidogen-1 in maintenance of basement membrane integrity[109]. Another isoform nidogen-2 is also present at the basement membrane and is upregulated in nidogen-1 null mice. Mice lacking nidogen-2 have a normal lifespan and do not exhibit any visible defects. However, mice lacking both nidogen-1 and nidogen-2 die shortly after birth, indicating that the two isoforms may compensate for each other in maintenance of basement membrane integrity[110]. Heparan sulfate proteoglycan 2, also known as perlecan, is a large protein that binds to laminin and collagen and plays an important role in maintaining the structural integrity of the basement membrane. Perlecan knockout mice display severe cardiac, cerebral and skeletal defects; are embryonic lethal and die by E12[111].

1.2.3.5 Integrins

Integrins are transmembrane proteins involved in cell-ECM adhesion. However, a few integrins also mediate cell-cell adhesion – for example, integrin $\alpha_L\beta_2$ present on white blood cells that bind to ICAM1 present on vascular endothelial cells at the sites of infection. They are heterodimeric proteins composed of α and β subunits, that are non-covalently bound to each other. There are eighteen α subunits and eight β subunits, which combine together to form twenty-four functional isoforms of integrins. Through various interactions, integrins mediate stable adhesion of the cell with the basement membrane, cell migration along the basement membrane, modulate cell signaling cascades for cell survival, proliferation, differentiation and movement[112].

A number of integrins – αvβ3, α5β1, α6β1, α1β1 and α6β4 – have been primarily implicated in the BBB function. Integrin αvβ3 is one of the most important integrins present at the BBB and is highly expressed in the cells of neurovascular units – ECs, astrocytes and microglia. It plays an important role in angiogenesis and mice lacking either the αv or β3 subunit are lethal. Approximately 80% of αv knockout mice develop severe heart defects and die between E10 and E12. The remaining develop severe intracerebral hemorrhages and die shortly after birth[113]. Integrin α5β1 is another important isoform that is present on ECs and astrocytes; and is implicated in the maintenance of BBB. It plays a major role in angiogenesis during development, and α5 knockout mice die by E11 due to poor angiogenesis, leaky vasculature and severe defects in the neural tube[114, 115].

Integrins α6β1 and α1β1 are very highly expressed in the ECs of the CNS. In contrast to integrins αvβ3 and α5β1 that are primarily expressed during embryogenesis and early stages of development, the expression of integrins α6β1 and α1β1 in the vasculature increases in adulthood[113, 116]. Mice lacking α1 subunit of integrin are viable and do not display any visible defects, while integrin β1 subunit knockout mice show severe embryonic lethality with most of the mice dying around E6[114]. The embryonic lethality of mice lacking β1 subunits can be attributed to the fact that these mice lack various integrins having the β1 component – α5β1, α6β1, α1β1 – which play an important role during embryogenesis.

1.3 Genes associated with hemorrhagic diseases in human patients

In human patients, a number of genes have been implicated in various cerebrovascular diseases that affect the integrity of the vasculature in the brain and lead to hemorrhages (Table 1.1). These include several small vessel diseases (SVDs), many of which are heritable, such as cerebral autosomal dominant arteriopathy with subcortical infarcts and leukoencephalopathy (CADASIL), cerebral autosomal recessive arteriopathy with subcortical infarcts and leukoencephalopathy (CARASIL), cerebral amyloid angiopathy and retinal vasculopathy with cerebral leukodystrophy (RVCL). Patients having cerebral cavernous malformation (CCM) and intracranial aneurysms (IA) often develop severe intracranial hemorrhage due to weakening of the walls of blood vessel and subsequent leakage. Various genome wide association studies (GWAS) and candidate gene studies in the last few decades have yielded insights into the genes associated with these cerebrovascular diseases involving blood vessels of all sizes, that lead to the development of microbleeds, intracerebral hemorrhages or stroke in human patients[117].

Cerebral autosomal dominant arteriopathy with subcortical infarcts and leukoencephalopathy (CADASIL) is a disease that often manifests in early or late adulthood and is characterized by the presence of small subcortical infarcts. CADASIL is an inheritable genetic condition and follows an autosomal-dominant mode of inheritance. CADASIL patients develop subcortical ischemic lesions, migraine and cognitive impairment leading to partial or full cognitive disability.

Disease	Genes	Symptoms	References
Cerebral autosomal dominant arteriopathy with subcortical infarcts and leukoencephalopathy (CADASIL)	*NOTCH3*	Stroke, dementia, migraine, subcortical infarcts and psychiatric disturbances.	Joutel et al.[118]
Cerebral autosomal recessive arteriopathy with subcortical infarcts and leukoencephalopathy (CARASIL)	*HTRA1*	Stroke, dementia, deterioration in brain function, alopecia, multiple infarcts and spondylosis.	Hara et al.[119]
Cerebral Amyloid Angiopathy (CAA)	*APP* *BRI2* *CST3* *TTR* *GSN*	Accumulation of amyloid fibers in small to medium-sized vessels of brain, intracerebral hemorrhage and dementia.	Rovelet-Lecrux et al. [120] Vidal et al.[121] Ghiso et al.[122] Brett et al.[123] Ghiso et al.[124]
Retinal vasculopathy with cerebral leukodystrophy (RVCL)	*TREX1*	Retinopathy, stroke, dementia and psychiatric disturbances	Richards et al.[125]
Fabry's disease	*GLA*		Taguchi et al.[126]
COL4-related small vessel disease (SVD)	*COL4A1* *COL4A2*	Intracerebral hemorrhage, porencephaly and stroke.	Gould et al.[104]
Cerebral cavernous malformations (CCM)	*CCM1/KRIT1* *CCM2* *CCM3/PCDC10*	Vascular malformation, intracerebral hemorrhages and seizures.	Couteulx et al.[127] Liquori et al.[128] Bergametti et al.[129]
Intracranial aneurysms (IA)	*SOX17* *CDKN2A, B* *CNNM2* *KL/STARD13* *RBBP8* *EDNRA*	Weakening of the vessel wall, subarachnoid and intracerebral hemorrhage.	Bilguvar et al.[130] Yasuno et al.[131] Yasuno et al.[131] Yasuno et al.[131] Yasuno et al.[131] Yasuno et al.[132]

Table 1.1 | List of some cerebrovascular diseases in humans, genes associated with them, their symptoms and main references.

It is caused due to dominant mutation in *NOTCH3* gene, with more than 200 mutations have been reported in CADASIL patients[118, 133]. The cerebral vasculature of CADASIL patients shows thickening of the vessel wall, characterized by the presence of granular osmiophilic material (GOM) deposits of varying shape, size and morphology. The walls of the blood vessels of CADASIL patients have extensive accumulation of the extracellular domain of NOTCH3 protein. However, the molecular mechanisms leading to the disease are not yet understood[134].

Cerebral autosomal recessive arteriopathy with subcortical infarcts and leukoencephalopathy (CARASIL) is an extremely rare autosomal-recessive disease that manifests during early adulthood. The initial symptoms of CARASIL are gait disturbance and back pain, with the symptoms getting progressively worse with age. Approximately 25% suffer from stroke before the age of 40 and the incidence of strokes increases progressively in CARASIL patients, with some patients developing intracerebral hemorrhage[135, 136]. CARASIL has been associated with mutations in high-temperature requirement-A serine peptidase gene (*HTRA1)*, encoding a serine protease that regulates TGF-β signaling necessary for maintenance of vascular integrity. However, the detailed molecular pathways underlying *HTRA1* mutation and development of CARASIL is not properly known.

Cerebral amyloid angiopathy (CAA) is one of the largest risk factors of ICH with approximately one-third of the spontaneous incidents of ICH being a consequence of CAA[3]. It is common in the elderly and is characterized by the deposition of amyloid fibrils in the walls of small to medium-sized blood vessels of the brain. Based on multiple GWASs and candidate gene studies, a number of genes have been implicated in CAA – amyloid precursor protein (*APP*), integral membrane protein 2B (*BRI2*), cystatin C (*CST3*), transthyretin (*TTR*), gelsolin (*GSN*) and apolipoprotein-E (*APOE*)[117].

Cerebral cavernous malformations (CCMs) are the most common vascular lesions in the CNS, characterized by densely packed vascular sinusoids lacking the structural components of vessel wall and lacking necessary junctions with the neighboring cells of the CNS. These lesions can be present throughout the CNS and vary in size (1-5 cm). Although most of the CCMs are clinically silent, these lesions may leak in some patients and cause severe intracerebral hemorrhage[137]. CCMs are hereditary and caused by loss of function mutation in *CCM1*/*KRIT1*, *CCM2* and *CCM3*/*PCDC10* genes[127-129]. CCM proteins are highly

expressed in the ECs of the brain; and are critical for angiogenesis, development of vasculature and maintenance of EC integrity. While the constitutive deletion of *Ccm* genes are embryonic lethal, the postnatal deletion of individual *Ccm* genes in the ECs of mice lead to the formation of acute cavernous malformations in brain and retina, highly reminiscent of the symptoms observed in human CCM patients[138-140]. CCM proteins are cytoplasmic and occur together in a dynamic trimeric complex, where CCM2 acts as a scaffolding protein and physically associates with CCM1 and CCM3. The three CCM proteins also interact with a number of other proteins and mediate various signaling pathways suggested to be involved in cell proliferation, cell differentiation, angiogenesis, vascular development and maintenance of EC integrity[141]. The disruption of CCM protein functions leads to the activation of RhoA thereby modulating the actin cytoskeletal dynamics, but the mechanism leading to CCM still remains to be investigated[142].

1.4 Ageing-associated changes in vasculature

Ageing is a non-modifiable risk factor for a number of vascular diseases and is associated with functional, structural and mechanical changes that occur in the blood vessels with advancing age. Endothelial dysfunction, inflammation of the vasculature, calcification, deposition of amyloid fibrils in the small vessels of the brain and increased stiffness of vasculature are some major changes that accompany ageing. These age-associated changes in the blood vessel very closely resemble the changes that have been observed in the vasculature of young patients suffering from hypertension, indicating a very close association between biological ageing and hypertension[8].

One of the most significant age-associated changes observed in the blood vessels is the increased thickness of the vessel wall coupled with reduction in the luminal diameter. The vessel walls also show reduced elasticity and increased stiffness due to calcification of the vascular media with ageing[143]. Molecular mechanisms that have been implicated in age-associated calcification of vessels include the upregulation of transcription factor CBFA1 and BMP2, which regulate the expression of various osteogenic proteins such as osteonectin, osteocalacin and collagen-1; and downregulation of calcification inhibitors such as fetuin-A and osteopontin[144, 145].

Endothelial dysfunction is a common feature of an ageing vasculature and is associated with reduced vasodilatory response, leading to compromised endothelial-dependent dilation of the blood vessels in old rodents and humans. The endothelium of blood vessels in aged mice have reduced bioavailability of endothelial nitric oxide (NO), which is critical for the relaxation of ECs. Aged rodents show reduced levels of tetrahydrobiopterin, also known as BH4, which is a key cofactor necessary for the synthesis of endothelial NO by the enzyme endothelial nitric oxide synthase[146]. A number of molecular mechanisms and cell signaling pathways have been implicated in the age-dependent structural, functional and mechanical changes that occur in the vasculature (Figure 1.6).

Sirtuins are a family of nicotinamide adenine dinucleotide (NAD) -dependent deacetylases and ribosyltransferases, implicated in various cellular processes, mainly ageing, inflammation, metabolism and mitochondrial biogenesis. There are seven members of the sirtuin family and each of them has a distinct subcellular localization – SIRT1 and SIRT2 in cytoplasm, SIRT1, 2, 6 and 7 in nucleus and SIRT3, 4 and 5 in mitochondria[147]. Among these, sirtuin1 and 3 have been implicated in maintenance of vascular integrity in mice, with *Sirt3* $^{-/-}$ mice exhibiting accelerated vascular ageing indicated by hypertrophy and fibrosis[148]. Microvessels isolated from aged human and rodent brains have reduced expression of sirtuin1 at transcript and protein levels. In addition, brain EC-specific *Sirt1* knockout mice show reduced expression of claudin-5 expression and increased BBB permeability, indicating an important role of *Sirt1* in the maintenance of BBB[149].

Mitogen-activated protein kinase (MAPK) signaling pathway is a major regulator of various cellular processes such as growth, differentiation, survival, migration and inflammatory response. The primary targets of the MAP kinase pathway are transcription factors that regulate the expression of the target genes and modulate cellular functions. MAP kinase pathway has been found to be upregulated with ageing in vasculature, suggesting its role in various age-associated changes in the vasculature[150]. Oxidative stress is another important factor associated with age-dependent changes in the vasculature. Ageing leads to an increased accumulation of reactive oxygen species (ROS), thereby resulting in oxidation of several proteins, DNA and lipids. The ROS-mediated oxidative damage of biomolecules results in impaired molecular and cellular function, leading to the development of pathological disorders in the vasculature[151]. Increased accumulation of ROS in vasculature has been

directly implicated in reduced vascular levels of endothelial nitric oxide and impaired vasodilatory properties of blood vessels.

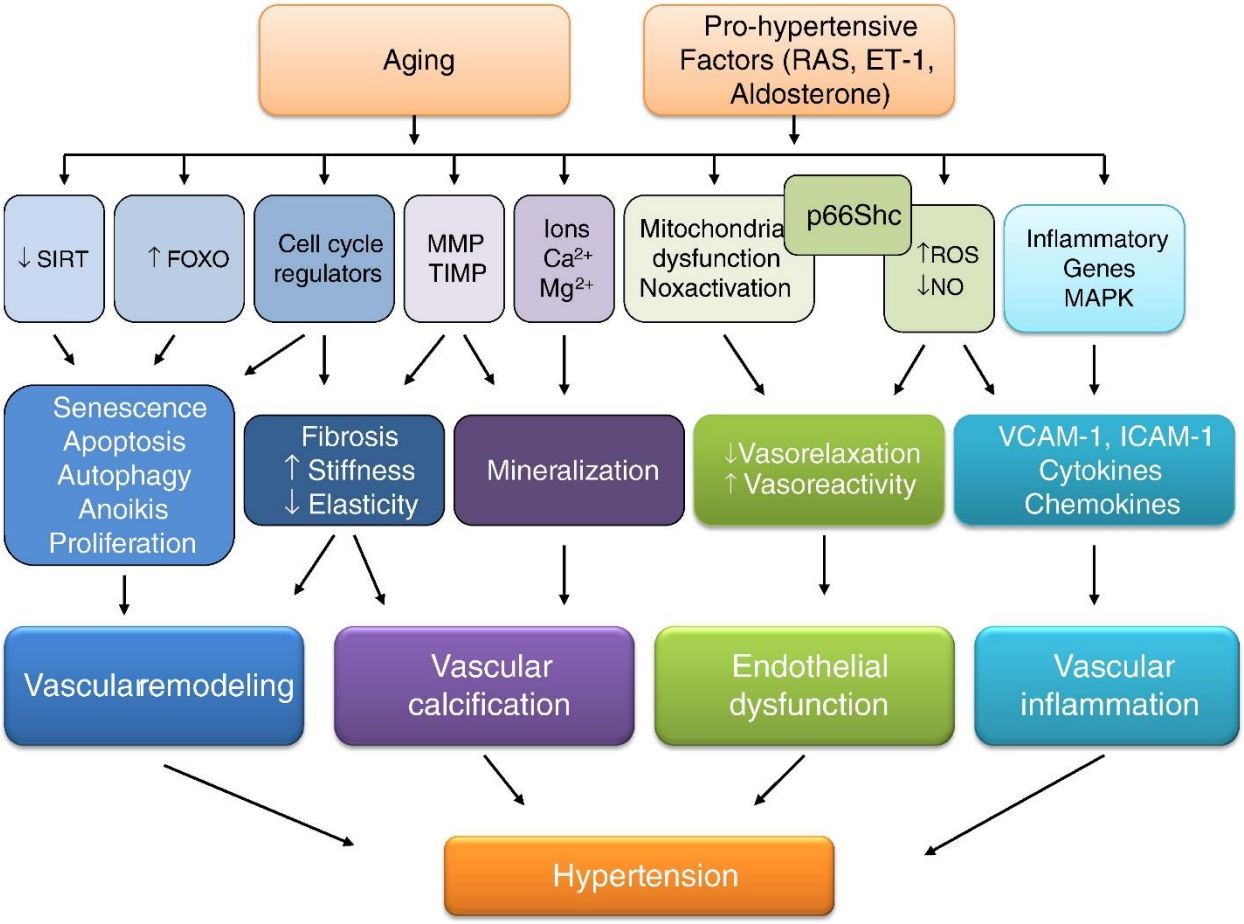

Figure 1.6 | Molecular and cellular mechanisms associated with vascular changes in ageing and hypertension. Activation of pro-fibrotic, pro-inflammatory, redox-sensitive and growth/apoptotic signaling pathways leads to changes in vascular structure, mechanics and function with resultant arterial remodeling, calcification, inflammation, stiffness and impaired vasoreactivity. These vascular alterations are common features during ageing and in hypertension. VCAM-1, vascular cell adhesion molecule-1; ICAM-1, intercellular adhesion molecule-1; MMP, matrix metalloproteinases; TIMP, tissue inhibitor of metalloproteinase; RAS, renin angiotensin system; ET-1, endothelin-1; NO, nitric oxide. Reprinted from Harvey et al., 2015[8]

Oxidative stress is also associated with increased pro-inflammatory response and activation of molecular pathways resulting in cell senescence and endothelium dysfunction[152]. Multiple oxidases including NADPH oxidases (Nox), xanthine oxidase and several mitochondrial oxidases generate ROS in the ECs. Increased accumulation of ROS in ageing organisms can be attributed to age-dependent dysfunction of mitochondria resulting in impaired metabolism and formation of free radicals[8, 153].

Renin-angiotensin-aldosterone system (RAAS) is the principal regulator of blood pressure and plays a crucial role in functional and mechanical changes that occur in vasculature. When the blood pressure is lower than normal, kidneys convert prorenin circulating the blood to renin and secrete it into the blood circulation. Renin converts angiotensinogen to angiotensin I, which is further converted to angiotensin II by angiotensin-converting enzyme (ACE) present on the cell membrane of the endothelial cells. Angiotensin II binds to its receptor AT_1R initiating a downstream signaling cascade that leads to vasoconstriction and increases the blood pressure. The expression of various components of RAAS, such as prorenin receptor, ACE, AT_1 receptor and angiotensin II, are significantly upregulated in the blood vessels of aged mice[154].

Endothelial apelin/apelin receptor signaling system consists of endothelium-derived peptide apelin and its receptor APJ, a rhodopsin-like G-protein coupled receptor (GPCR). Apelin receptor is known to play a crucial role in positive regulation of vasodilation by heterodimerizing with angiotensin II type 1 receptor (AT1R) leading to its inhibition, thereby negatively regulating the renin-angiotensin system and promoting vasodilation[155, 156]. Apelin/APJ system also plays a crucial role in angiogenesis[25], protection of BBB damage during ischemic stroke[157] and regulates fatty acid uptake in the endothelial cells[158].

Apelin/APJ system has been implicated in vascular health in humans, with human patients suffering from cardiovascular diseases having reduced levels of apelin in tissues and circulating blood[159]. The expression of apelin and its receptor decreases in several organs of ageing mice. *Apln*$^{-/-}$ and *Aplnr*$^{-/-}$ mice show pathological signs of accelerated ageing as evident from early-onset infertility, increased levels of blood glucose and impaired renal function. *Aplnr*$^{-/-}$ mice have normal blood pressure at birth, which starts to rise around 9 months and develop hypertension by the age of 12 months. Systemic restoration of apelin via infusion in *Apln*$^{-/-}$ mice reduces age-associated pathological symptoms and improves vital

metabolic parameters, indicating the role of apelin/APJ system in age-associated changes in vasculature[160]. In vitro studies have established the role of apelin receptor in regulating biomechanical and morphological properties of ECs. Apelin receptor is located at the cellular junctions and its activation regulates signaling pathways that mediate adaptation of ECs to the flow conditions by modulating EC morphology, elasticity, adhesion and spreading[161].

1.5 Serum Response Factor

Serum response factor (SRF) is one of the four founding members of the MADS-box family of transcription factors[162]. It is among the best-studied DNA-binding proteins and is known to regulate ~1000 genes[163, 164]. SRF activity is stimulated by either of its cofactors myocardin related transcription factor (MRTF) or ternary complex factors (TCF). While MAP kinase signaling-dependent activation of TCFs, encoded by the *Elk1*, *Elk3* and *Elk4* genes, induces the SRF-mediated transcriptional induction of immediate early genes; Rho/actin-dependent nuclear translocation of the MRTFs, encoded by the *Mrtfa* and *Mrtfb* genes, stimulates SRF-mediated transcriptional activation of genes encoding cytoskeletal proteins[165, 166]. Thus, SRF regulates a number of cellular processes like cell differentiation, proliferation, migration and survival, and plays a crucial role in organismal growth and development. Being one of the key regulators of mesoderm formation and angiogenesis, mice with SRF knockout are embryonic lethal[165]. Changes in SRF expression cause various pathologies, indicating that SRF has a role in pathogenesis of numerous diseases[167, 168].

SRF and its cofactors MRTF-A and MRTF-B play an important role in maintaining normal functioning of the CNS vasculature. EC-specific deletion of *Srf* or *Mrtf* at either postnatal or adult age induced cerebral hemorrhages in mice. Tamoxifen-induced EC-specific post-natal depletion of SRF in *Srf* ^{iECKO} mice resulted in behavioral abnormalities such as reduced exploratory behavior, difficulty in walking, hemiplegia and ataxia. These mice exhibited extremely reduced survival (17 days). Severe hemorrhages in various parts of the brain were observed upon hematoxylin-eosin (H&E) staining of paraffin-embedded brain sections (Figure 1.7).

Adult-depletion of SRF in *Srf* ^{iECKO} mice caused multifocal cerebral hemorrhages and mice succumbed to stroke-like symptoms. These mice exhibited an impaired basal

membrane structure and a significant reduction in the expression of the ECM protein collagen IV in the brain. The *Srf* ^{iECKO} mice showed reduced expression of tight junction protein claudin-5 in the brain. These mice also had significantly reduced mRNA levels of adherens junction protein cadherin-5 and tight junction proteins claudins-1, 3, 5, 12, ZO2 and ZO3 in the brain. These findings suggest that SRF directly or indirectly regulates the expression of target genes encoding proteins that are components of tight junctions, adherens junctions, basement membrane components and other crucial proteins involved in the maintenance of vascular integrity in the CNS. Thus, SRF and the MRTFs were implicated in the formation and the maintenance of a functional blood-brain barrier[169].

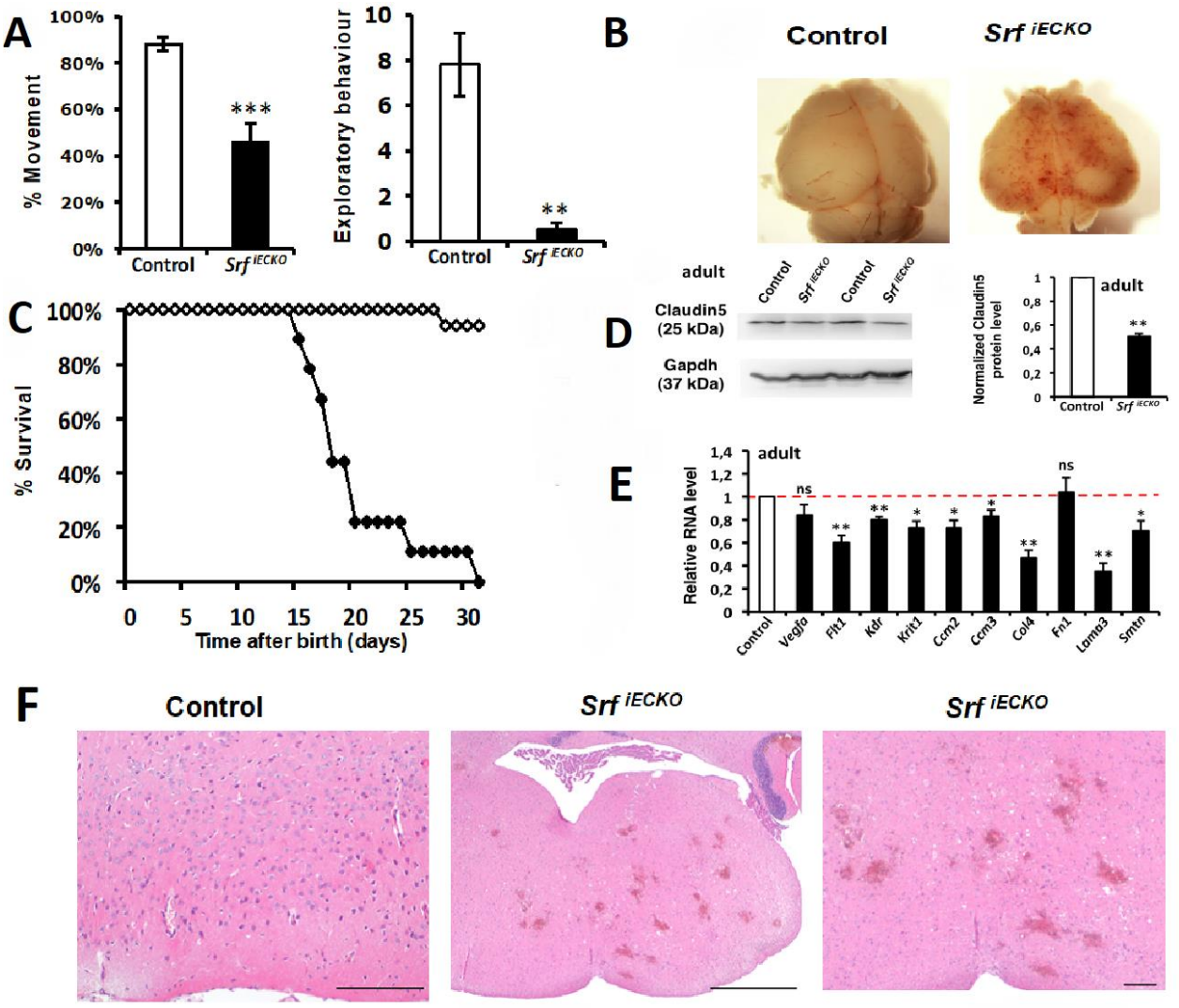

Figure 1.7 | *Srf* ^{iECKO} animals suffer from cerebral hemorrhages. **A)** *Srf* ^{iECKO} mice display compromised movement and exploratory behavior. **B)** Hemorrhages in the brain of *Srf* ^{iECKO} mice. **C)** Kaplan–Meier plot (percent survival) of control and *Srf* ^{iECKO} mice upon postnatal *Srf* deletion. **D)** Brain lysates from *Srf* ^{iECKO} mice have a reduced level of Claudin 5 expression in comparison to control mice, as detected by western blot. **E)** Relative RNA levels of *Vegfa*, angiogenic receptors, different CCMs, and components of the basement membrane in the whole brain of control vs. *Srf* ^{iECKO} mice **F)** H&E staining of adult control and *Srf* ^{iECKO} brain sections, revealing multiple hemorrhages in *Srf* ^{iECKO} brains [Scale bars, 200 µm (left), 1,000 µm (center) and 200 µm (right)], from Weinl et al., 2015[169].

1.6 Aims

Considering that intracerebral hemorrhages increase with age in humans, age-dependent changes in EC-specific expression of genes responsible for the maintenance of BBB may contribute to human ICH pathology. The study aims to investigate age-dependent changes in expression levels of genes responsible for maintenance of BBB integrity and elucidate underlying potential age-dependent epigenetic mechanisms in the cerebral ECs of ageing mice.

Age-dependent increases in cerebral bleedings were observed in mice with functional *Srf* and *Mrtf* genes, as well as in wild-type mice. Interestingly, unpublished data provided by Prof. Dr. Ralf Adams (Max Planck Institute for Molecular Biomedicine, Münster) suggested an age-dependent downregulation in the levels of *Srf* and *Mrtf* transcripts in retinal ECs. These data, along with hemorrhagic stroke-like phenotype exhibited by the EC-specific *Srf*-knockout mice, lead us to hypothesize that, in mice, increased intracerebral bleeding with increasing age may be caused by age-dependent downregulation of *Srf/Mrtf* gene expression and/or downregulation of SRF/MRTF-dependent target gene expression in cerebral ECs.

To obtain an insight into the expression levels of genes encoding major components of tight junction, adherens junction and basement membrane in the cerebral ECs of mice belonging to different ages, RNA-seq was used to study the mRNA expression levels in ECs isolated from murine brains of increasing age – 2, 6, 12, 18 and 24 months. Since age-dependent changes in the expression level of genes may be caused due to epigenetic mechanisms, an essential aim of the study was to investigate the possibility of age-dependent epigenetic regulation of gene expression in ECs of mouse brains.

Methylation of cytosine in CpG-rich promoter regions of genes is an important epigenetic modification associated with its transcriptional downregulation[170]. While ageing leads to global hypomethylation, many regulatory regions are known to be hypermethylated with age[171]. Reduced representation bisulfite sequencing (RRBS), a bisulfite conversion-based protocol that enriches CG-rich regions of the genome and converts unmethylated cytosines to uracil, was used to study age-dependent changes in CpG methylation of promoter regions. This method involves enrichment of genomic regions that contain CpG dinucleotides. HaeIII, a restriction endonuclease, cleaves genomic DNA at CC↓GG sites and generates DNA fragments of a size range of 40-300 bp that are rich in CpG dinucleotides.

These fragments contain a representative coverage of most promoter regions and CpG island regions in the genome. After selection of these fragments, they are ligated to adapters, followed by bisulfite treatment. The bisulfite-modified fragments which contain the majority of the promoter regions and CpG islands in the genomic DNA can be then sequenced. The RRBS does not provide 100% CpG dinucleotide coverage like the whole-genome bisulfite sequencing (WGBS), but captures the majority of the promoter and CpG rich regions[172].

Another mechanism of epigenetic regulation is at the level of chromatin modification. Assay for transposase-accessible chromatin sequencing (ATAC-seq), a method to assess the genome-wide chromatin accessibility, was used to study age-dependent changes in chromatin structure in the murine cerebral ECs. The process involves treating the chromatin with a hyperactive mutant of the enzyme transposase Tn5, which excises open chromatin not bound to nucleosomes and ligates adapters at the end of the excised fragments for high-throughput sequencing[173]. The excised DNA fragments with adapters ligated at the ends are amplified by PCR and sequenced. Sequencing results provide an insight into the open regions of chromatin, indicating the regions of active transcription.

The study promises to provide a better understanding of the molecular mechanisms contributing to age-dependent cerebral bleeding in mice, and further our understanding of the basic mechanisms underlying intracerebral hemorrhage in human patients. The insights obtained on the molecular mechanisms leading to the age-dependent ICH may have important clinical and therapeutic implications.

Chapter 2

Materials and methods

Chapter 2

Materials and methods

2.1 Materials

2.1.1 Standard labware

Cell strainer 70 µm (Falcon)
Cover slips (Thermo Scientific)
FACS sterile tube (Falcon)
Filter tips 10µL (Sarstedt)
Filter tips 20 µL (Sarstedt)
Filter tips 200 µL (Sarstedt)
Filter tips 1000 µL (Sarstedt)
Microscopy slides (Carl Roth)
Nitrile examination gloves (Halyard)
Pipetman micropipettes (Gilson)
PCR 8-strip tubes (Biozym)
PCR Soft tubes 0.2 mL (Biozym)
Syringe filters 0.45 µm (Carl Roth)
Tubes 15 mL (Sarstedt)
Tubes 50 mL (Sarstedt)
Tissue culture dish 100, standard (Sarstedt)
Tissue culture plate, 24 well (Sarstedt)
Tissue culture plate, 96 well (Falcon)
Tubes 0.5 mL (Sarstedt)
Tubes 1.5 mL (Sarstedt)
Tubes 2 mL (Sarstedt)

2.1.2 Technical equipment

Benchtop centrifuge, Biofuge Pico (Heraeus instruments)
Benchtop centrifuge, Megafuge 2.0R (Heraeus instruments)
Centrifuge, Rotanta 460R (Hettich)
CO_2 Incubator, BBD 6220 (Heraeus Instruments)
Electrophoresis power supply unit, PowerPAC 300 (Biorad)
Embedding machine, Shandon Histocentre 2 (Shandon)
Fluorescence microscope, Axiovert 200M (Zeiss)
Gel documentation systems (Axygen, peqlab)
Glass plates with 1.5 mm spacer (Bio-Rad)
Laminar flow hood (Tecnoflow)
MACS Octo Dissociator with heater (Miltenyi Biotec)
Magnetic rack (Thermo Scientific)
Microscope, Zeiss Axioplan 2 (Zeiss)
Mini-PROTEAN Gel casting frame (Bio-Rad)
Mini-PROTEAN Gel casting stand (Bio-Rad)
Optical microscope, Axiovert 25 (Zeiss)
PCR Thermocycler, TProfessional Trio (Biometra)
pH meter (Hanna)
Qubit 3.0 fluorometer (Invitrogen)
Refrigerator (Liebherr)
Rotary Microtome, Leica RM 2155 (Leica)
Thermomixer (Eppendorf)
Tissue processor, Shandon Citadel 1000 (Shandon)
Trans-Blot Turbo transfer system (Bio-Rad)
Ultra-low temperature freezer (New Brunswick)
Water bath (GFL)

2.1.3 Histology

Acetic acid (Sigma-Aldrich)

Adhesive microscope slides 76 mm x 26 mm x 1 mm (Marienfeld HistoBond®)

Entellan® New rapid mounting medium for microscopy (Merck)

Eosin-Y solution 0.5% in water (Carl Roth)

Ethanol (Sigma-Aldrich)

Hematoxylin solution according to Gill II (Carl Roth)

Hydrochloric Acid (Merck)

Macrosette processing/embedding cassettes with lid (Simport/Carl Roth)

Microscope cover glasses 24 mm x 55 mm (R. Langenbrinck)

Roti®-Histol (Carl Roth)

Surgipath Paraplast (Leica)

2.1.4 Genotyping of mice

Agarose LE (Genaxxon Bioscience)

dNTPs 10 mM each (Promega)

Lysis Buffer

(composition of lysis buffer is as follows)

1 M Tris (pH 8.3)	10 mL
0.5 M EDTA (pH 8)	1 mL
10% SDS	2 mL
4M NaCl	5 mL
H_2O	82 mL

Midori green Advance DNA stain (Nippon Genetics Europe)

PCR Buffer 10x (Thermo Scientific)

PCR tubes 0.2 mL (Biozym)

Primers (Sigma-Aldrich)

Primer	Sequence (5'→ 3')
SATM-VE-s1	AACCTCCCTCAGAGAAGCTGCGA
SA-MembTom-as1	TGCTCACCATGGTCTTGGAGA
PCR3	AAGAAGGGTCCGGCCCCGAAGATGCTGGGC
PCR4	CTGGATGCCCTCTCCTTCCCCGGAGCCCTG

Proteinase K solution 20 mg/ml (Genaxxon Bioscience)

Taq polymerase (Thermo Scientific)

2.1.5 Isolation of endothelial cells

Adult Brain Dissociation Kit (Miltenyi Biotec)

C Tube (Miltenyi Biotec)

DAPI (Applichem)

Dulbecco's Phosphate Buffered Saline (Sigma-Aldrich)

Dulbecco's Phosphate Buffered Saline (with Glucose, Pyruvate, Calcium and Magnesium)

Calcium Chloride 1M	450 µL
Magnesium Chloride 1M	250 µL
Glucose solution (225 gram/liter)	2.22 mL
Sodium Pyruvate 100 mM	1.65 mL
Dulbecco's Phosphate Buffered Saline (Sigma-Aldrich)	500 mL

FACS buffer (DPBS, 2%FCS and 2mM EDTA)

2.1.6 RNA isolation

RNeasy Micro kit (Qiagen)

RNAse ZAP (Thermo Fisher)

2-Mercaptoethanol, 50 mM (Life Technologies)

2.1.7 Assay for transposase-accessible chromatin sequencing (ATAC-seq)

Adapter Reverse (Nextera)

Adapter Forward (P506 Nextera)

AMPure XP Beads (Beckman Coulter)

cOmplete Protease Inhibitor Cocktail tablets EDTA-free (Roche)

DNase Buffer A

(The composition of DNase Buffer A is as follows)

Nuclease-free water	46 mL
KCl (1 M)	3 mL
Tris-HCl (1M, pH 8.0)	750 µL
NaCl (5M)	150 µL
EGTA (0.5M, pH 8.0)	50 µL
Spermidine (0.5 M)	750 µL

IGEPAL® CA-630 (Sigma)

Nextera DNA Sample Preparation Kit (Illumina)

Next High-Fidelity 2X PCR Master Mix (New England Biolabs)

Qiagen MinElute PCR Purification Kit (Qiagen)

Qubit dsDNA HS Assay Kit (Thermo Fisher)

Spermidine (Sigma)

2.1.8 Reduced representation bisulfite sequencing (RRBS)

Ampure XP Beads (Beckman Coulter)

ATP, 10M (New England Biolabs)

Centrifugal filter for nucleotide purification, Modified PES 30k (VWR)

Chloroform: Isoamyl 24:1 (Sigma Aldrich)

CutSmart Buffer 10x (New England Biolabs)

dATP 10 mM (New England Biolabs)

dNTPs 2.5 mM each (New England Biolabs)

Elution Buffer (Qiagen)

Ethanol – 100%, 80% and 70%

EZ DNA Methylation Gold Kit (Zymo Research)

Glycogen 20 mg/mL (Roche)

HaeIII restriction enzyme (New England Biolabs)

Hotstart PCR Buffer, 10x (Qiagen)

HotStart Taq Polymerase (Qiagen)

Klenow exo- 5 U/µL (New England Biolabs)

Lysis Buffer (10 mM TrisHCl, 5 mM EDTA)

$MgCl_2$ 25 mM (Qiagen)

Phenol: Chloroform: Isoamyl Mix 25:24:1 (Invitrogen)

Primer, forward (P5): 5'- AAT GAT ACG GCG ACCACC GAG ATC TAC AC – 3'

Primer, reverse (P7): 5'- CAA GCA GAA GAC GGC ATA CGA GAT – 3'

Proteinase K 20 mg/mL (Sigma Aldrich)

Qubit dsDNA HS Assay Kit (Thermo Fisher)

Solution A(1X) (25mM EDTA, 75mM NaCl)

Solution B (1X) (10 mM EDTA, 10 Mm Tris-HCl (pH 8), 1% SDS)

T4 Ligase 2000U/ µL (New England Biolabs)

Unique Molecular Identifier Adapters, TruSeq Single Index Set B (Illumina)

2.1.9 Illumina adapter indexes

Adapter ID	Sequence in Oligo	Sequence in Sequencing Read	Description	Chemistry
1	CGTGAT	ATCACG	Illumina_TruSeq_FirstIndexOnReversePrimer	Truseq
2	ACATCG	CGATGT	Illumina_TruSeq_FirstIndexOnReversePrimer	Truseq
3	GCCTAA	TTAGGC	Illumina_TruSeq_FirstIndexOnReversePrimer	Truseq
4	TGGTCA	TGACCA	Illumina_TruSeq_FirstIndexOnReversePrimer	Truseq
5	CACTGT	ACAGTG	Illumina_TruSeq_FirstIndexOnReversePrimer	Truseq
6	ATTGGC	GCCAAT	Illumina_TruSeq_FirstIndexOnReversePrimer	Truseq
7	GATCTG	CAGATC	Illumina_TruSeq_FirstIndexOnReversePrimer	Truseq
8	TCAAGT	ACTTGA	Illumina_TruSeq_FirstIndexOnReversePrimer	Truseq
9	CTGATC	GATCAG	Illumina_TruSeq_FirstIndexOnReversePrimer	Truseq
10	AAGCTA	TAGCTT	Illumina_TruSeq_FirstIndexOnReversePrimer	Truseq
11	GTAGCC	GGCTAC	Illumina_TruSeq_FirstIndexOnReversePrimer	Truseq
12	TACAAG	CTTGTA	Illumina_TruSeq_FirstIndexOnReversePrimer	Truseq
13	TTGACT	AGTCAA	Illumina_TruSeq_FirstIndexOnReversePrimer	Truseq
14	GGAACT	AGTTCC	Illumina_TruSeq_FirstIndexOnReversePrimer	Truseq
15	TGACAT	ATGTCA	Illumina_TruSeq_FirstIndexOnReversePrimer	Truseq
16	GGACGG	CCGTCC	Illumina_TruSeq_FirstIndexOnReversePrimer	Truseq
17	CTCTAC	GTAGAG	Illumina_TruSeq_FirstIndexOnReversePrimer	Truseq
18	GCGGAC	GTCCGC	Illumina_TruSeq_FirstIndexOnReversePrimer	Truseq
19	TTTCAC	GTGAAA	Illumina_TruSeq_FirstIndexOnReversePrimer	Truseq
20	GGCCAC	GTGGCC	Illumina_TruSeq_FirstIndexOnReversePrimer	Truseq
21	CGAAAC	GTTTCG	Illumina_TruSeq_FirstIndexOnReversePrimer	Truseq
22	CGTACG	CGTACG	Illumina_TruSeq_FirstIndexOnReversePrimer	Truseq
23	CCACTC	GAGTGG	Illumina_TruSeq_FirstIndexOnReversePrimer	Truseq
24	GCTACC	GGTAGC	Illumina_TruSeq_FirstIndexOnReversePrimer	Truseq

25	ATCAGT	ACTGAT	Illumina_TruSeq_FirstIndexOnReversePrimer	Truseq
26	GCTCAT	ATGAGC	Illumina_TruSeq_FirstIndexOnReversePrimer	Truseq
27	AGGAAT	ATTCCT	Illumina_TruSeq_FirstIndexOnReversePrimer	Truseq
28	CTTTTG	CAAAAG	Illumina_TruSeq_FirstIndexOnReversePrimer	Truseq
29	TAGTTG	CAACTA	Illumina_TruSeq_FirstIndexOnReversePrimer	Truseq
30	CCGGTG	CACCGG	Illumina_TruSeq_FirstIndexOnReversePrimer	Truseq
31	ATCGTG	CACGAT	Illumina_TruSeq_FirstIndexOnReversePrimer	Truseq
32	TGAGTG	CACTCA	Illumina_TruSeq_FirstIndexOnReversePrimer	Truseq
33	CGCCTG	CAGGCG	Illumina_TruSeq_FirstIndexOnReversePrimer	Truseq
34	GCCATG	CATGGC	Illumina_TruSeq_FirstIndexOnReversePrimer	Truseq
35	AAAATG	CATTTT	Illumina_TruSeq_FirstIndexOnReversePrimer	Truseq
36	TGTTGG	CCAACA	Illumina_TruSeq_FirstIndexOnReversePrimer	Truseq
37	ATTCCG	CGGAAT	Illumina_TruSeq_FirstIndexOnReversePrimer	Truseq
38	AGCTAG	CTAGCT	Illumina_TruSeq_FirstIndexOnReversePrimer	Truseq
39	GTATAG	CTATAC	Illumina_TruSeq_FirstIndexOnReversePrimer	Truseq
40	TCTGAG	CTCAGA	Illumina_TruSeq_FirstIndexOnReversePrimer	Truseq
41	GTCGTC	GACGAC	Illumina_TruSeq_FirstIndexOnReversePrimer	Truseq
42	CGATTA	TAATCG	Illumina_TruSeq_FirstIndexOnReversePrimer	Truseq
43	GCTGTA	TACAGC	Illumina_TruSeq_FirstIndexOnReversePrimer	Truseq
44	ATTATA	TATAAT	Illumina_TruSeq_FirstIndexOnReversePrimer	Truseq
45	GAATGA	TCATTC	Illumina_TruSeq_FirstIndexOnReversePrimer	Truseq
46	TCGGGA	TCCCGA	Illumina_TruSeq_FirstIndexOnReversePrimer	Truseq
47	CTTCGA	TCGAAG	Illumina_TruSeq_FirstIndexOnReversePrimer	Truseq
48	TGCCGA	TCGGCA	Illumina_TruSeq_FirstIndexOnReversePrimer	Truseq
N501	TAGATCGC	TAGATCGC	Nextera_i5_ForwardIndex_1	Nextera
N502	CTCTCTAT	CTCTCTAT	Nextera_i5_ForwardIndex_2	Nextera
N503	TATCCTCT	TATCCTCT	Nextera_i5_ForwardIndex_3	Nextera

N504	AGAGTAGA	AGAGTAGA	Nextera_i5_ForwardIndex_4	Nextera
N505	GTAAGGAG	GTAAGGAG	Nextera_i5_ForwardIndex_5	Nextera
N506	ACTGCATA	ACTGCATA	Nextera_i5_ForwardIndex_6	Nextera
N507	AAGGAGTA	AAGGAGTA	Nextera_i5_ForwardIndex_7	Nextera
N508	CTAAGCCT	CTAAGCCT	Nextera_i5_ForwardIndex_8	Nextera
N701	TCGCCTTA	TAAGGCGA	Nextera_i7_ReverseIndex_1	Nextera
N702	CTAGTACG	CGTACTAG	Nextera_i7_ReverseIndex_2	Nextera
N703	TTCTGCCT	AGGCAGAA	Nextera_i7_ReverseIndex_3	Nextera
N704	GCTCAGGA	TCCTGAGC	Nextera_i7_ReverseIndex_4	Nextera
N705	AGGAGTCC	GGACTCCT	Nextera_i7_ReverseIndex_5	Nextera
N706	CATGCCTA	TAGGCATG	Nextera_i7_ReverseIndex_6	Nextera
N707	GTAGAGAG	CTCTCTAC	Nextera_i7_ReverseIndex_7	Nextera
N708	CCTCTCTG	CAGAGAGG	Nextera_i7_ReverseIndex_8	Nextera
N709	AGCGTAGC	GCTACGCT	Nextera_i7_ReverseIndex_9	Nextera
N710	CAGCCTCG	CGAGGCTG	Nextera_i7_ReverseIndex_10	Nextera
N711	TGCCTCTT	AAGAGGCA	Nextera_i7_ReverseIndex_11	Nextera
N712	TCCTCTAC	GTAGAGGA	Nextera_i7_ReverseIndex_12	Nextera

Table 2.1 | Illumina adapter indexes with sequences of oligos, sequencing reads, their description and the chemistry involved.

2.1.10 Western blotting

Acrylamide, 40% (Applichem)

Ammonium persulfate, 10% w/v

Chemiluminescent HRP substrate (Millipore)

Immobilon-P PVDF transfer membrane, 0.45 µm (Merck)

Isopropanol (Sigma-Aldrich)

Loading buffer, 6X (50mL Upper-Tris, 40mL 100% Glycerin, 8g SDS, 4mL β-mercaptoethanol, 1 mL 1% bromophenolblue)

Lower-Tris buffer (1.5M Tris-Cl, 0.4% SDS, pH adjusted to 8.8)

Methanol (Sigma-Aldrich)

N,N,N',N' – tetramethylethylene diamine (TEMED)

Non-Fat Dry Milk (5% w/v in 1X TBST)

PageRuler™ Prestained Protein Ladder, 10 to 180 kDa (ThermoFisher)

Roti®-Quant, 5X concentrate (Carl Roth)

Running buffer (1X Transfer buffer, 0.1% SDS)

Sodium Dodecyl Sulfate, 10% w/v

TBS, 10X (0.2M Tris, 1.38M NaCl, pH adjusted to 7.6)

TBST (1X TBS, 0.1% Tween 20)

Towbin buffer (1X Transfer buffer, 0.04% SDS, 20% methanol)

Transfer buffer, 10X (1.92M Glycin, 0.25 M Tris, pH adjusted to 8.3)

Upper-Tris buffer (0.5M Tris-Cl, 0.4% SDS, pH adjusted to 6.3)

Primary antibodies :

- Anti-Aplnr, raised in rabbit (Invitrogen #711101)
- Anti-Cldn5, raised in rabbit (Invitrogen #34-1600)
- Anti-GAPDH, raised in mouse (Acris #ACR001P)
- Anti-Histone H3, raised in rabbit (Cell Signaling Technology #4499S)
- Anti-Itm2a, raised in rabbit (Invitrogen #PA5-87859)

Secondary antibodies :

- Anti-mouse IgG, HRP-linked whole antibody (GE Healthcare)
- Anti-rabbit IgG, HRP-linked whole antibody (GE Healthcare)

2.2 Methods

2.2.1 Processing of brain tissues for histology

Brains were harvested from both wild-type mice and mice having floxed, yet non-recombined *Srf* and *Mrtf* alleles, thereby having functional *Srf* and *Mrtf* genes (wild-type phenotype) and washed with ice-cold 1X PBS. Brains were fixed in 4% PFA solution at 4°C with gentle rotation for 72 hours. The brains were transferred to embedding cassettes and washed under running cold tap water for 3 hours in a beaker. The fixed brain tissues were further treated with increasing concentration of isopropanol, Roti®-Histol and paraplast to dehydrate the tissues; and prevent the hardening and brittleness of dehydrated tissues. The tissues were processed in in a Shandon Citadel 1000 tissue processor at following program:

50% Isopropanol	2 hours
75% Isopropanol	2 hours
90% Isopropanol	2 hours
100% Isopropanol	2 hours
100% Isopropanol	3 hours
100% Isopropanol	3 hours
Roti®-Histol	1.5 hours
Roti®-Histol	1.5 hours
Paraplast	1.5 hours
Paraplast	1.5 hours

The processed brain tissues were embedded in paraplast in a Shandon Histocentre 2 embedding machine. The cassettes containing embedded tissues were left to cool for the paraplast to solidify.

2.2.2 Histology

The excess paraplast around embedded brain tissues was manually removed and the tissues were coronally sectioned with a Leica rotary microtome RM 2155. Four consecutive sections, each with a thickness of 6 µm, were mounted on a Marienfeld HistoBond® adhesive microscope slide. Hematoxylin-eosin (H&E) staining was performed on every tenth slide to observe bleedings in the brain. The staining was performed with following steps:

Roti®-Histol	10 minutes
Roti®-Histol	10 minutes
100% Ethanol	5 minutes
96% Ethanol	5 minutes
80% Ethanol	2 minutes
70% Ethanol	2 minutes
Distilled water (running)	2 minutes
Hematoxylin	4 minutes
0.1% Hydrochloric acid	15 seconds
Distilled water (running)	5 minutes
Eosin (500µL acetic acid added to 250 mL 0.5% Eosin solution)	5 minutes
Distilled water (running)	2 minutes
70% Ethanol	1 minute
100% Ethanol	2 minutes
Roti®-Histol	2 minutes

Cover slips were mounted with Entellan as the mounting medium and the Hematoxylin-Eosin stained brain sections were observed under Zeiss Axioplan 2 microscope. Larger bleedings and smaller microbleeds were counted in every tenth slide.

2.2.3 Breeding of mice

The transgenic Cdh5-mT H2B-GFP mice express, under vascular endothelial (VE) Cadherin (also called cadherin 5 or Cdh5) promoter, membrane-targeted tandem-dimer tomato and a fusion protein histone2B-GFP. These mice express – specifically in the endothelial cells – red fluorescence in the cell membrane and green fluorescence in the nuclei. Two male transgenic Cdh5-mT H2B-GFP (heterozygous) mice having a C57BL/6J background were provided by Prof. Dr. Ralf Adams (Max Planck Institute for Molecular Biomedicine, Münster).

Breeding was initiated and the colony was expanded at the animal facility in the department of molecular biology (Interfaculty Institute of Cell Biology, Auf der Morgenstelle 15). The mice were maintained in Type II long polycarbonate cages and 2-5 mice were kept in each cage. The mice were kept under 12 hours day/night cycle, involving daytime from 6 a.m. to 6 p.m. with light and night from 6 p.m. to 6 a.m. without light. The temperature maintained inside the animal facility was 21°C and the Relative Humidity was 60%. The mice had unrestricted access to dried food pellets and water. The bottom of the cage was covered with wooden chips that acted as bedding for the mice and cellulose paper was provided to the mice for building nests. The cages containing female mice, additionally, received a wooden toy to keep them occupied. The cages having only one mouse also received the wooden toy. The cages were changed every week by the animal caretakers to maintain optimum hygiene. The mice were randomly checked for the presence of pathogens and infections every six months.

The mice were maintained according to the regulations pertaining to legal animal protection laws and the permissions to carry the experiments performed as part of this project were duly obtained from the concerning authorities at the district administrative office in Tübingen (Mitteilung nach § 4 Abs. 3 TierSchG, dated 18.10.2017).

2.2.4 Identification of mice and ear punching

The pups were weaned after 21 days of their birth and separated into new cages. After the pups had been separated into new cages, ear punching was done to assign a unique identity to each mouse. The mice were taken out of the cage, gently held by the neck and a small hole was made in the ear. The mice were named according to the scheme illustrated in Figure 2.1. A mouse with hole on the top of its right ear was designated the number 1, while the mouse having a hole on the bottom of its right ear was designated the number 3. A mouse with two holes – on top of both right and left ears was assigned the number 11 (1+10). The same principle of numbering and identifying the mice were followed depending on the holes in ears of the mice.

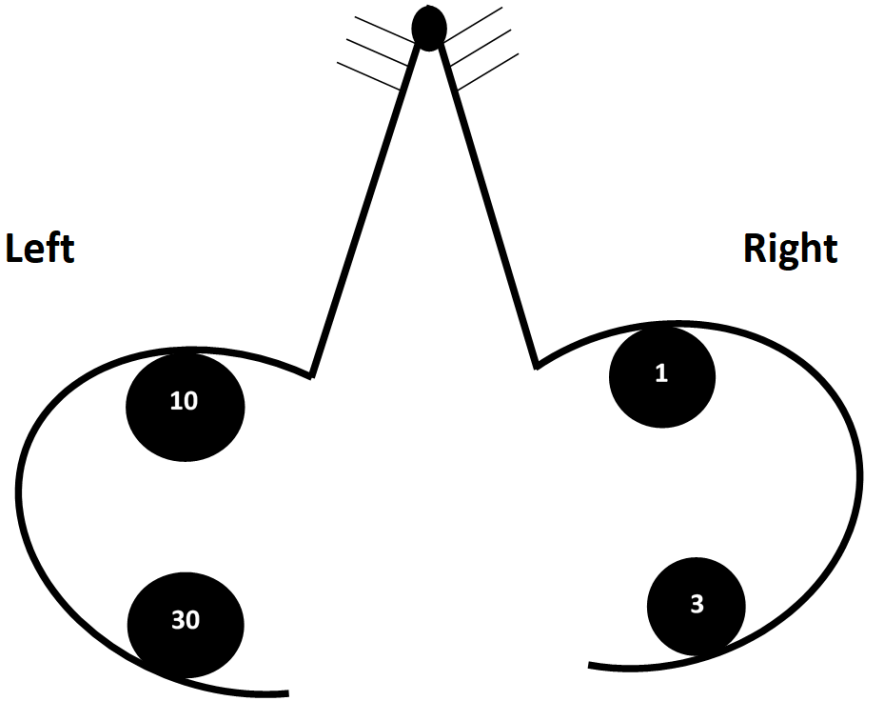

Figure 2.1 | Ear punching scheme to assign identification number to mice. Small punches were made in the ear of the mouse to assign a unique number to them for the purpose of their identification. A hole on the top (dorsal side) in right ear represents number 1, while the hole on the bottom (ventral side) in the right ear represents number 3. Similarly, the holes on top and bottom in the left ear represent 10 and 30, respectively. A mouse can have one or a combination of more than one holes to assign it a unique number.

2.2.5 Genotyping

The piece of tissue extracted during ear punching was used for the genotyping of mice. The ear tissue was lysed in 90µL lysis buffer and 10 µL Proteinase K solution. The lysis step was performed on an Eppendorf thermomixer overnight at 55°C and 750 rpm, followed by incubation at 98°C for 15 minutes to inactivate the Proteinase K. The lysate was centrifuged in a Heraeus Biofuge pico at full speed for 5 minutes to collect the debris at the bottom and a clear supernatant on top containing dissolved genetic materials, that was used for genotyping. For the polymerase chain reaction, 1 µL supernatant was added to 49 µL PCR mix in a 0.2 mL PCR tube. The PCR mix for a single reaction was prepared with the following composition:

dNTPs (10 mM each)	1 µL
10x PCR Buffer	5 µL
H_2O	36.5 µL
Primer SATM-VE-s1(10 µM)	1.5 µL
Primer SA-MembTom-as1(10 µM)	1.5 µL
Primer PCR3 (10 µM)	1.5 µL
Primer PCR4 (10 µM)	1.5 µL
Taq Polymerase	0.5 µL

The PCR machine was switched on and the tubes were transferred to the heating block once the lid attained a temperature of 80°C. The PCR involved 35 cycles of amplification. The program used for the PCR was as follows:

2 minutes at 94 °C
30 seconds at 94 °C
30 seconds at 55°C
60 seconds at 72°C
} 35 cycles
5 minutes at 72°C

2.25g of Agarose LE powder was dissolved in 150 mL of 1X TAE buffer to prepare 1.5% agarose gel. 5µL of Midori Green was added to the solution and the gel was let to solidify. The PCR products were loaded on the gel and electrophoretic separation was

performed for 75 minutes at a fixed voltage of 120 Volts and a current of 400 Amperes. 10 µL of 100 base pair (bp) DNA ladder was loaded as a marker.

The forward primer SATM-VE-s1 and the reverse primer SA-MembTom-as1 are specific to the 733 bp membrane-targeted tandem dimer tomato sequence present in the Cdh5-mT H2B-GFP transgene and amplify the fragment. The primers PCR3 and PCR4 are specific to the 530 bp fragment, corresponding to the LXR-β gene in the mouse genome and are used for the purpose of internal control.

The agarose gel was observed under ultraviolet light in Herolab EASY 429k gel documentation system. The presence of the band at 530 base pairs corresponding to LXR-β gene (PCR3/PCR4 internal control) in the agarose gel indicated that the PCR was successful. The presence of band at 733 bp indicated a transgenic mouse having Cdh5-mT H2B-GFP transgene and the absence of the band indicated a wild-type mouse lacking the transgene.

2.2.6 Isolation of endothelial cells

2.2.6.1 Dissection of mice

All possible efforts were taken to minimize stress faced by the mice during the procedure. The mice were transferred to the animal facility at FACS Core Facility Berg, Universitätsklinikum Tübingen (Otfried-Müller-straße 10) a day before the sacrifice to let them acclimatize overnight. The mice were sacrificed by exposure to CO_2 gas till the breathing stopped, followed by cervical dislocation. The body weight and brain weight of the mice were recorded. The brains were immediately harvested and washed in ice-cold 1X DPBS.

Adult Brain Dissociation Kit (Miltenyi Biotec) – that combines mechanical dissociation with papain-based enzymatic digestion of the brain tissues – was used to prepare single-cell suspension from adult mice brain. The components of Adult Brain Dissociation Kit (Miltenyi) are as follows:

Enzyme P	Ready to use; Aliquoted and stored at -20°C
Buffer Z	Ready to use; Stored at 4°C
Buffer Y	Ready to use; Stored at 4°C

Enzyme A (lyophilized powder)	Reconstituted by dissolving in 1 mL Buffer A and aliquots stored at -20°C
Buffer A	Ready to use; Stored at 4°C
Red blood cell removal solution (10x)	Ready to use; Stored at 4°C
Debris removal solution	Ready to use; Stored at 4°C

2.2.6.2 Digestion of brain tissue

1950 µL Enzyme mix1 (50 µL Enzyme P and 1900 µL Buffer Z) was prepared and added to the C tube (Miltenyi Biotec). Each brain was cut into 8 sagittal slices and transferred to the C tube containing the enzyme mix 1. Enzyme mix 2 (10 µL Enzyme A and 20 µL Buffer Y) was added to the C tube. The tube containing the brain tissue and enzymes were loaded on gentleMACS Octo Dissociator with heaters for digestion and the program 37C_ABDK_01 was started. After the completion of the dissociation, the tube was centrifuged for 30 seconds at 4°C to collect the samples at the bottom of the tube. The digested tissue was resuspended with a 1000 µL pipette tips and the sample was passed through 70 µm strainer placed on 50 mL tube. 10 mL of ice-cold DPBS (with calcium, magnesium, glucose and pyruvate) was added and the suspension was centrifuged for 10 minutes at 300g and 4°C. The supernatant was aspirated and discarded.

2.2.6.3 Removal of debris

The pellet was resuspended with 3100 µL of ice-cold DPBS (with calcium, magnesium, glucose and pyruvate) and the suspension was transferred to a 15 mL tube. 900 µL debris removal solution was added (for removal of debris from brain tissues of 18 and 24 months-old samples, 1050 µL debris removal solution was added) and the suspension was mixed with a 10 mL pipette to avoid the formation of air bubbles. 4 mL of DPBS (with calcium, magnesium, glucose and pyruvate) was layered on the top of the suspension by pipetting extremely carefully so that the cell suspension and DPBS phases did not mix. The suspension was centrifuged (with brakes applied for gradual acceleration) for 10 minutes at 3000g and 4°C. Three phases were formed. The top two phases consisting of debris were completely aspirated and discarded. 12 mL of DPBS (with calcium, magnesium, glucose and pyruvate) was added and the tube was gently inverted three times without disturbing the pellet. The

tube was centrifuged for 10 minutes at 1000g and 4°C and the supernatant was aspirated completely.

2.2.6.4 Removal of red blood cells

10x red blood cells removal solution was diluted 1:10 in ice-cold double distilled water to prepare a 1x working red blood cell removal solution. The cell pellet obtained was gently resuspended in ice-cold 1mL 1x red blood cell removal solution and incubated for 10 minutes in refrigerator (2 – 8°C). 10 mL of ice-cold PB buffer – 0.5% FCS in DPBS (with calcium, magnesium, glucose and pyruvate) – was added to the suspension and centrifuged for 10 minutes at 300g and 4°C. The supernatant was aspirated and discarded completely.

2.2.6.5 Preparation of single-cell suspension

The pellet was resuspended in FACS buffer (1X PBS, 2%FCS and 2mM EDTA) to prepare a single-cell suspension and 0.05 µg/mL DAPI was added to stain the dead cells. The single-cell suspension was filtered through a 70 µm cell strainer to exclude any remaining debris or cell aggregates.

2.2.6.6 FACS sorting of endothelial cells

The FACS sorting was performed by Dr. Kristin Bieber at the FACS Core Facility Berg, Universitätsklinikum Tübingen (Otfried-Müller-Straße 10). Cells double positive for tdTomato and GFP were sorted on a BD FACS AriaII sorter. Endothelial cells were directly sorted into RLT Buffer (Qiagen), a guanidine isothiocyanate-based lysis buffer. For RRBS and ATAC-seq, endothelial cells were sorted into FACS buffer (1X PBS, 2%FCS and 2mM EDTA) and the sorting was performed at 4°C.

Single-cell suspensions from brains of littermate wild-type mice lacking the Cdh5-mT H2B-GFP transgene were used as negative controls for FACS. The single-cell suspension from the non-transgenic, wild-type mice did not display a population of cells positive either for tdTomato or GFP.

2.2.7 Number of mice sacrificed for the project

	RNA-seq		ATAC-seq and RRBS	
Age	**Males**	**Females**	**Males**	**Females**
2 months	3	3	4	6
6 months	3	3	3	3
12 months	3	3	6	6
18 months	3	3	7	5
24 months	3	3	NA	NA

Table 2.2 | Number of mice sacrificed for the project. Male and female mice belonging to each of the 2, 6, 12, 18 and 24 months-old age groups were used for RNA-seq, ATAC and RRBS experiments. A total of 64 animals were sacrificed, of which 32 were males and 32 females. RRBS and ATAC-seq experiments could not be performed on 24 months-old mice due to unavailability of mice belonging to the 24 months-old cohort.

2.2.8 Extracting RNA from endothelial cells

Column-based extraction of RNA was performed with RNeasy Micro Kit (Qiagen) according to the manufacturer's instructions. The RNA isolation was performed in a hood cleaned with RNaseZAP to avoid any RNase contamination. The RNeasy Micro Kit consists of the following components:

RNeasy MinElute Spin columns
Buffer RLT
Buffer RW1
Buffer RPE
RNase-free water
1.5 mL collection tubes
2 mL collection tubes
DNase stock solution
Buffer RDD

2.2.8.1 Cell lysis

RLT Buffer (Qiagen) contains high concentration of guanidine isothiocyanate that promotes cell lysis and supports binding of RNA to the silica-based extraction columns. The endothelial cells were sorted directly into 1mL RLT Buffer containing 10 µL β-mercaptoethanol (to denature RNases and DNases) and vortexed for 1 minute to ensure complete lysis of the cells. 1 mL 70% EtOH was added to the lysate and mixed well by pipetting. The sample was transferred to RNeasy MinElute spin column placed in a 2 mL collection tube and centrifuged for 15 seconds at 8000g in a benchtop centrifuge. The flow-through was discarded. 350 µL Buffer RW1 was added to the column and centrifuged for 15 seconds at 8000g and the flow-through was discarded.

2.2.8.2 DNase digestion on column

10 µL DNase I stock solution was added to 70 µL Buffer RDD and the solution was mixed by gently inverting the tube. The 80 µL DNase I incubation mix was directly added to the column and incubated at room temperature for 15 minutes.

2.2.8.3 Ethanol washes

350 µL Buffer RW1 was added to the column and centrifuged for 15 seconds at 8000g in a benchtop centrifuge. The flow-through and collection tube were discarded. The column was placed in a new 2mL collection tube and 500 µL Buffer RPE was added to the column. The sample was centrifuged for 15 seconds at 8000g and the flow-through was discarded. 500 µL 80% EtOH was added to the column and centrifuged for 2 minutes at 8000g. The flow-through and the collection tube were discarded, and the column was placed in a new 2 mL collection tube. The lid of the column was opened and centrifuged for 5 minutes at 8000g.

The column was placed in a new 1.5 mL collection tube and RNA was eluted in 20 µL RNAse free water and stored at –80°C. The RNA samples were sent (on dry ice) to Dr. Robert Geffers at the Helmholtz Zentrum für Infektionsforschung, Braunschweig for subsequent library preparation and sequencing.

2.2.9 Sample details for RNA-seq

Sample ID	Age	Sex	Body weight	Brain weight	No. of ECs
18c1	2 months	Male	22.00 gram	0.54 gram	145,902
18c3	2 months	Male	25.10 gram	0.46 gram	196,228
18c4	2 months	Male	25.7 gram	0.43 gram	182,458
18c5	2 months	Female	22.47 gram	0.44 gram	159,018
18c6	2 months	Female	17.7 gram	0.40 gram	208,381
18c8	2 months	Female	22.36 gram	0.43 gram	175,190
12e1	6 months	Male	40.97 gram	0.46 gram	103,872
12e2	6 months	Male	33.04 gram	0.39 gram	178,277
12e3	6 months	Male	36.56 gram	0.45 gram	122,451
16a6	6 months	Female	28.90 gram	0.44 gram	34,838
20b4	6 months	Female	28.66 gram	0.47gram	47,375
20b6	6 months	Female	28.88 gram	0.45 gram	175,959
9a1	12 months	Male	43.82 gram	0.48 gram	56,648
12a1	12 months	Male	37.44 gram	0.48 gram	96,089
12a2	12 months	Male	39.10 gram	0.41 gram	109,328

13a6	12 months	Female	32.56 gram	0.47gram	70,164
13a7	12 months	Female	28.80 gram	0.47gram	54,134
13a9	12 months	Female	30.20 gram	0.44 gram	90,220
5e3	18 months	Male	34.91 gram	0.44 gram	47,483
5e4	18 months	Male	39.48 gram	0.46 gram	127,173
5e6	18 months	Male	36.52 gram	0.44 gram	133,178
6f6	18 months	Female	31.16 gram	0.49 gram	82,393
6f7	18 months	Female	31.85 gram	0.50 gram	220,753
6f8	18 months	Female	28.54 gram	0.51 gram	135,954
3a3	23 months	Male	34.54 gram	0.43 gram	160,203
3b3	23 months	Male	33.73 gram	0.47 gram	95,529
4b2	23 months	Male	38.12 gram	0.44 gram	104,188
3c5	22 months	Female	32.24 gram	0.48 gram	123,555
3c8	22 months	Female	36.53 gram	0.44 gram	105,776
3c9	22 months	Female	30.36 gram	0.49 gram	87,219

Table 2.3 | Details of mice sacrificed for RNA-seq. The table contains the sample ID (identification numbers of the mice), age, sex, body weight, weight of the brains and number of ECs isolated from each mouse.

2.2.10 Assay for transposase-accessible chromatin sequencing (ATAC-seq)

2.2.10.1 Preparation of nuclei from endothelial cells

Murine cerebral endothelial cells were sorted into FACS buffer (1X PBS, 2%FCS and 2mM EDTA) at 4°C and the suspension containing the sorted ECs was transferred to a 15 mL tube for ATAC-seq. The cells were centrifuged for 5 minutes at 500g and 4°C and the supernatant was discarded. The cell pellet was gently resuspended in 1 mL pre-cooled DNase buffer A containing protease inhibitor cocktail (PIC). 10 µL of 10% IGEPAL® CA-630 solution was added to the suspension to obtain a final concentration of 0.1% IGEPAL. The tube was very gently inverted 3-4 times and incubated on ice for 5 minutes to prepare nuclei from the endothelial cells. The principle behind isolating nuclei from cells involve treating the cells with low concentration of IGEPAL® CA-630, which lyses the cell membrane but does not lyse the nuclear membrane. The nuclei were centrifuged for 5 minutes at 500g and 4°C and the supernatant was discarded. The nuclei were very gently resuspended in 1 mL pre-cooled DNase buffer A containing protease inhibitor cocktail (PIC) with a tip whose end had been cut to increase the size of its orifice.

2.2.10.2 Tagmentation by Tn5 transposase

50,000 – 55,000 nuclei were transferred to a 1.5 mL tube and centrifuged for 9 minutes at 500g and 4°C. The supernatant was discarded, and the pellet was resuspended in 47.5 µL ATAC-premix containing 22.5 µL nuclease-free water and 25 µL 2X TD buffer (Illumina). 2.5 µL Tn5 transposase enzyme was added to the suspension and incubated at 37°C for 30 minutes. The clean-up was performed with MinElute PCR Purification Kit (Qiagen) and the library was eluted with 26 µL elution buffer.

2.2.10.3 Amplification of libraries

The ATAC library was amplified by polymerase chain reaction. For PCR, 20 µL template was added to 30 µL PCR mix (25 µL NEB Next High Fidelity 2X Master Mix, 1 µL each forward and reverse primers and 3 µL H_2O). The same forward primer (Adapter ID P506) was used for all the samples while unique reverse primers were used for each sample for the purpose of identification. The PCR reaction was performed with the following program:

72°C for 5 minutes

98°C for 30 seconds

98°C for 10 seconds

63°C for 30 seconds — 12 cycles

72°C for 1 minute

72°C for 5 minutes

2.2.10.4 Post-PCR cleanup

The PCR product was cleaned up with 0.8x volume of Ampure beads XP. 40 µL Ampure beads XP was added to the PCR product and uniformly mixed by pipetting 10-15 times. The sample was incubated at room temperature for 5 minutes and transferred to a magnetic rack for 2 minutes. The supernatant was carefully removed without disturbing the pellet attached to the wall. The pellet was washed twice with 80% EtOH for 30 seconds without removing the tube from magnetic rack. The tube was kept on the magnetic rack at room temperature for 10 minutes to ensure complete evaporation of ethanol. The pellet was resuspended with 22 µL of 0.1X TE buffer by pipetting 10-15 times and was transferred to magnetic rack for 2 minutes. 20 µL of supernatant was carefully discarded without disturbing the pellet and transferred to a new 1.5 mL tube. The amplified ATAC library was analyzed with an Agilent Bioanalyzer and sequencing was performed in the lab of Prof. Dr. Jörn Walter at the University of Saarland, Saarbrücken.

2.2.11 Sample details for ATAC-seq

Sample ID	Age	Sex	Body weight	Brain weight	No. of ECs
15b2	2 months	Male	25.82 gram	0.41 gram	60,378
15b3	2 months	Male	24.73 gram	0.40 gram	110,189
15b4	2 months	Male	25.70 gram	0.42 gram	60,600
17b5	2 months	Female	17.93 gram	0.42 gram	110,184
17b6	2 months	Female	22.09 gram	0.44 gram	110,155
17b9	2 months	Female	19.37 gram	0.44 gram	110,114
16a3	6 months	Male	39.87 gram	0.47 gram	105,159

20b2	6 months	Male	37.42 gram	0.41 gram	53,792
20b3	6 months	Male	41.59 gram	0.43 gram	105,121
18b5	6 months	Female	27.51 gram	0.46 gram	110,180
18b6	6 months	Female	26.06 gram	0.41 gram	110,223
19b11	6 months	Female	24.31 gram	0.42 gram	110,167
13a1	12 months	Male	35.88 gram	0.45 gram	110,105
13a2	12 months	Male	36.52 gram	0.42 gram	108,357
13a3	12 months	Male	36.3 gram	0.44 gram	55,111
12a6	12 months	Female	31.25 gram	0.50 gram	107,189
12a8	12 months	Female	31.51 gram	0.47 gram	110,173
12a9	12 months	Female	28.96 gram	0.46 gram	52,635
4g1	18 months	Male	36.91 gram	0.45 gram	115,219
4g2	18 months	Male	-	-	97,305
8b3	18 months	Male	41.47 gram	0.42 gram	52,141
7b7	18 months	Female	29.26 gram	0.44 gram	50,196
7b9	18 months	Female	39.33 gram	0.46 gram	61,698
8d9	18 months	Female	41.14 gram	0.51 gram	115,228

Table 2.4 | Details of mice sacrificed for ATAC-seq. The table contains the sample IDs (identification numbers of the mice) of the mice sacrificed for the ATAC-seq experiments, their age, sex, body weight, weight of the brains and number of ECs isolated from each mouse.

2.2.12 Reduced representation bisulfite sequencing (RRBS)

100,000 murine cerebral endothelial cells were sorted into FACS buffer (1X PBS, 2%FCS and 2mM EDTA) at 4°C and centrifuged for 5 minutes at 500g and 4°C. The supernatant was completely aspirated and discarded without disturbing the cell pellet. The cells were snap frozen by dipping the tube in liquid nitrogen and the snap-frozen cells were stored at –80°C till further processing.

2.2.12.1 Lysis of cells

200 µL each of solution A (25mM EDTA, 75mM NaCl) and solution B (10 mM EDTA, 10 Mm Tris-HCl, 1% SDS) were added to the frozen cell pellet. 10 µL Proteinase K (20 µg/µL) was added to the sample and briefly vortexed. The sample was centrifuged briefly to collect the materials at the bottom of the tube and incubated in a shaking thermomixer at 55°C.

2.2.12.2 Extraction of genomic DNA

400 µL Phenol-Chloroform-Isoamyl (25:24:1) mix was added to the sample and rotated overhead for 15 minutes. The samples were centrifuged at full speed for 5 minutes at room temperature and the upper, clear aqueous phase was very carefully transferred into a new tube. To this aqueous phase, 400 µL Phenol-Chloroform-Isoamyl (25:24:1) mix was added and the above steps were repeated. The upper, clear aqueous phase was very carefully transferred into a new tube.

400 µL Chloroform-Isoamyl (24:1) was added to the aqueous phase collected in new tube and rotated overhead for 15 minutes. The samples were centrifuged at full speed for 5 minutes at room temperature and the upper, clear aqueous phase was very carefully transferred into a new tube. 1.5 µL of Glycogen (20 µg/ µL), 0.1x volume (20 µL) of 3M Sodium Acetate and 2.5x volume (500 µL) of ice-cold 100% ethanol were added to the sample. The sample was inverted 8-10 times and incubated overnight at -20°C for the genomic DNA to precipitate in form of a pellet. The sample was centrifuged at 13,000 rpm for 45 minutes at 4°C and the supernatant was discarded without disturbing the pellet. The pellet was washed with 1 mL ice-cold 70% ethanol and centrifuged at 13,000 rpm for 45 minutes at 4°C. The washing with 1 mL ice-cold 70% ethanol was repeated, and the sample was centrifuged at 13,000 rpm for 45 minutes at 4°C. The pellet was dried at room temperature until the residual ethanol evaporated. The pellet was dissolved in 40 µL pre-warmed 1x Tris-EDTA (TE buffer)

at 45°C for 2 hours on a heat block. The concentration of DNA was measured on a Qubit fluorometer using a Qubit double stranded high sensitivity DNA assay kit according to the manufacturer's instructions.

2.2.12.3 Restriction digestion

To generate DNA fragments for bisulfite conversion, the isolated genomic DNA was treated with HaeIII – a restriction endonuclease that cleaves the genomic DNA at CC↓GG making blunt ends and generates DNA fragments of size 40-300 bp that are rich in CpG dinucleotides. 26 µL DNA template was used for the restriction digestion. 1 µL HaeIII restriction enzyme (New England Biolabs) and 3 µL 10x Cutsmart buffer (New England Biolabs) were added to the DNA template, and the contents were mixed by pipetting and inverting the tube 3-4 times. The tubes were briefly centrifuged to collect the sample at the bottom of the tube and were incubated overnight at 37°C.

2.2.12.4 A-tailing

The next step involves A-tailing, where the nucleotide Adenine is added to the 3' end of the DNA fragments to aid the Illumina adapters having thymine-overhangs get attached to the DNA fragments. 1 µL each of dATP (10 mM) and Klenow exo- (5 U/µL NEB) were added to the samples and mixed by pipetting. The samples were incubated at 37°C for 30 mins followed by further incubation at 75°C for 20 mins.

2.2.12.5 Adapter ligation

The mastermix for adapter ligation was prepared with the following components:

Nuclease-free H_2O	3.5 µL
Cutsmart (10x) Buffer	1 µL
ATP 10mM	2 µL
T4 Ligase (2000 U/µL)	0.5 µL

6 µL mastermix was added to each sample. To the sample containing A-tailed DNA fragments and mastermix, 1 µL of 10µM Illumina adapters were added such that each sample received a unique adapter. The sample was incubated overnight at 16°C, followed by incubation at 65°C for 20 minutes to inactivate the reaction.

2.2.12.6 Bisulfite conversion

EZ-DNA Methylation Gold Kit (Zymo Research) was used for the bisulfite conversion, a process which converts unmethylated cytosine to uracil while keeping 5-methylcytosine intact. Bisulfite conversion and subsequent cleanup was performed according to the manufacturer's instructions. The EZ-DNA Methylation Gold Kit (Zymo Research) has following components:

CT Conversion reagent
M-Dilution buffer
M-Dissolving buffer
M-Binding buffer
M-Wash buffer
M-Desulphonation buffer
Zymo-Spin™ IC Spin columns

700µL water, 300 µL M-Dilution buffer and 50 µL M-Dissolving Buffer were added to each tube of CT conversion reagent (for 10 reactions). The tube was shaken vigorously and incubated on a heat block at 50°C for 10 minutes to let the entire content dissolve. 110 µL of CT conversion reagent was added to 40 µL of DNA sample. The samples were placed in a thermocycler and the following program was started to initiate the bisulfite conversion reaction:

98°C for 10 mins
65°C for 2.5 hours
(Hold at 4°C for up to 20 hours.)

2.2.12.7 Cleanup after bisulfite conversion

600 µL M-Binding buffer was added to the Zymo-Spin™ IC Spin columns and the columns were placed into the provided collection tube. 150 µL of the sample was added to the column containing the M-Binding buffer and mixed by inverting 8-10 times. The sample was centrifuged at full speed (>10000g) for 30 seconds and the flow-through was discarded. 100 µL of M-Wash buffer was added to the column. The sample was centrifuged at full speed (>10000g) for 30 seconds and the flow-through was discarded. 200 µL of M-Desulphonation buffer was added to the column and incubated at room temperature for 15 minutes. The

sample was centrifuged at full speed (>10000g) for 30 seconds and the flow-through was discarded. 200 µL of M-Wash buffer was added to the column and centrifuged at full speed (>10000g) for 30 seconds. 200 µL of M-Wash buffer was added again to the column and centrifuged at full speed (>10000g) for 30 seconds. The flow-through was discarded and the columns were placed into a new 1.5 mL tubes. 24 µL nuclease-free water was added to the column to elute the DNA. The sample was centrifuged at full speed (>10000g) for 30 seconds, and the eluted volume containing the genomic material was collected.

2.2.12.8 PCR amplification

The PCR mastermix was prepared according to the following composition:

10x Hotstar PCR Buffer	3 µL
dNTPs 2.5 mM each	2 µL
$MgCl_2$ (25 mM)	1.2 µL
Forward Primer 10µM (P5)	0.6 µL
Reverse Primer 10µM (P7)	0.6 µL
Hotstart Taq Polymerase	0.6 µL

8 µL of the mastermix was added to 22 µL of sample in a PCR tube, and the PCR reaction was performed with the following program-

95°C for 15 minutes
95°C for 40 seconds
58°C for 1 minutes
72°C for 1 minutes
} 20 cycles
72°C for 12 minutes
4°C (hold)

2.2.12.9 Post-PCR cleanup

The PCR product was cleaned up with 0.8x volume of Ampure XP beads. 24 µL Ampure beads XP was added to the PCR product and was pipetted 10-15 times so that the beads were uniformly mixed with sample. The sample was incubated at room temperature for 5 minutes and transferred to a magnetic rack for 2 minutes. The supernatant was carefully removed without disturbing the pellet attached to the wall of the tube. The pellet was washed twice with 80% EtOH for 30 seconds without the tube being removed from the magnetic rack. The tube was kept on the magnetic rack at room temperature for 10 minutes to ensure complete evaporation of ethanol. The pellet was resuspended with 16 µL of 0.1X TE buffer by pipetting 10-15 times. The tube containing suspension was transferred to magnetic rack for 2 minutes. 14 µL of supernatant was carefully taken out without disturbing the pellet and transferred to a new 1.5 mL tube. The amplified RRBS library was analyzed with an Agilent Bioanalyzer and sequencing was performed by Dr. Gilles Gasparoni in the lab of Prof. Dr. Jörn Walter at the University of Saarland, Saarbrücken.

2.2.13 Sample details for RRBS

Sample ID	Age	Sex	Body weight	Brain weight	No. of ECs
15b2	2 months	Male	25.82 gram	0.41 gram	180,697
15b3	2 months	Male	24.73 gram	0.40 gram	201,535
15b4	2 months	Male	25.70 gram	0.42 gram	131,394
16e3	2 months	Male	28.77 gram	0.51 gram	251,438
17b9	2 months	Female	19.37 gram	0.44 gram	82,322
19e4	2 months	Female	22.48 gram	0.47 gram	276,792
19e5	2 months	Female	28.38 gram	0.43 gram	166,661
19e6	2 months	Female	22.01 gram	0.40 gram	152,248
16a3	6 months	Male	39.87 gram	0.47 gram	90,285
20b2	6 months	Male	37.42 gram	0.41 gram	105,192
20b3*	6 months	Male	41.59 gram	0.43 gram	89,506
18b5	6 months	Female	27.51 gram	0.46 gram	157,654
18b6*	6 months	Female	26.06 gram	0.41 gram	121,475

19b11	6 months	Female	24.31 gram	0.42 gram	164,534
12c1*	12 months	Male	41.22 gram	0.44 gram	201,097
12c2	12 months	Male	40.19 gram	0.46 gram	220,132
12d1	12 months	Male	33.84 gram	0.46 gram	220,126
12d3*	12 months	Female	26.52 gram	0.46 gram	220,114
12d4	12 months	Female	33.26 gram	0.48 gram	213,300
14c8	12 months	Female	27.92 gram	0.46 gram	220,287
13a1	12 months	Male	35.88 gram	0.45 gram	148,941
13a2	12 months	Male	36.52 gram	0.42 gram	78,585
13a3	12 months	Male	36.3 gram	0.44 gram	97,228
12a6*	12 months	Female	31.25 gram	0.50 gram	71,290
12a8*	12 months	Female	31.51 gram	0.47 gram	140,666
12a9	12 months	Female	28.96 gram	0.46 gram	80,041
8b1	18 months	Male	39.85 gram	0.45 gram	~30,000
8b2*	18 months	Male	35.03 gram	0.44 gram	~62,000
8c4	18 months	Male	45.71 gram	0.44 gram	80,751
3f2	18 months	Male	36.77 gram	0.45 gram	95,166
7b7	18 months	Female	29.26 gram	0.44 gram	~30,000
7b9	18 months	Female	29.19 gram	0.50 gram	~115,000
3f6	18 months	Female	27.89 gram	0.48 gram	118,663
8c10	18 months	Female	32.20 gram	0.45 gram	100,315

Table 2.5 | Details of mice sacrificed for RRBS. The table contains the sample IDs (identification numbers of the mice) of the mice sacrificed for the RRBS experiments, their age, sex, body weight, weight of the brains and number of ECs isolated from each mouse. Sequencing could not be performed on the samples marked * due to poor library quality.

2.2.14 RNA-seq analysis

The RNA-seq library was prepared and sequenced by Dr. Robert Geffers (Helmholtz Zentrum für Infektionsforschung, Braunschweig). Full-length cDNA libraries were prepared with the SMART-Seqv4 Ultra Low Input RNA kit (TaKaRa), which uses oligo(dT) priming and SMART (switching mechanism at the 5′ end of the RNA transcript) principle involving template switching reverse transcription. Nextera XT DNA Library Prep (Illumina) was used to prepare the libraries for sequencing. The libraries were sequenced on Illumina NovaSeq6000 sequencing system. The sequencing produced paired end reads with a length of 50 base pairs (PE50). On average, 44 million reads were sequenced per sample.

The raw sequencing files from RNA sequencing were obtained as FASTQ files and the preliminary quality control checks on the raw RNA-seq data were performed using FASTQC (v0.11.4) (https://www.bioinformatics.babraham.ac.uk/projects/fastqc/). The 3' adapter sequences (CTGTCTCTTATACACATCTGACGCTGCCGACGA) in the obtained sequencing reads were trimmed using Cutadapt[174] (v1.15), a command-line tool and quality control checks were again performed on the trimmed reads with FASTQC. The trimmed reads were then aligned to the mouse genome (GRCm38/mm10) using STAR aligner (v2.5.2b), an ultrafast universal RNA-seq alignment software[175]. The parameter *quantMode* was set to *GeneCounts* for the calculation of counts per gene. A comprehensive quality report for all the samples was generated with MultiQC[176] (v1.7) (https://multiqc.info/). The counts obtained after STAR alignment was used to study differential expression analysis using DESeq2[177] (v1.24.0).

The counts for transcripts for all the samples obtained from STAR aligner were sent to Dr. Gilles Gasparoni (University of Saarland, Saarbrücken) and the linear regression analysis was performed to study the age-associated changes in gene expression. The linear regression analysis was performed on TPM (transcripts per million) values, calculated by normalizing the raw read counts to the gene length and sequencing depth in each sample. Mathematically,

$$\mathrm{TPM} = \frac{\mathrm{RPK}_i \times 10^6}{\sum \mathrm{RPK}_i}$$

In the above equation, RPK_i is reads per kilobase for a gene *i*. $\sum \mathrm{RPK}_i$ is the sum of the RPK values of all the genes in a sample. The RPK value for a gene *i* is calculated as:

$$\mathrm{RPK}_i = \frac{\text{Raw read counts of a gene} \times 10^3}{\text{length of the gene (in bp)}}$$

Since TPM is calculated by normalizing the raw read counts to sequencing depth in addition to the gene length, the sum of TPM values of all the genes is same (=1,000,000) for each sample, thereby providing a robust comparison of transcript levels between samples.

2.2.15 RRBS analysis

The RRBS library was prepared as described (Section 2.2.12). RRBS sequencing was performed by Dr. Gilles Gasparoni on Illumina HiSeq 2500 sequencing system. Processing of the reads and subsequent data analysis were performed in the lab of Prof. Dr. Jörn Walter by Dr. Gilles Gasparoni (University of Saarland, Saarbrücken).

Raw sequencing reads obtained from RRBS were trimmed using the Trim Galore (v0.4.2) software (http://www.bioinformatics.babraham.ac.uk/projects/trim_galore/) to remove the adapter contamination and the 3' ends with base quality (PHRED score) of less than 20. The trimmed reads were then aligned to the mouse reference genome (GRCm38/mm10) using the BWA[178] (v0.6.2) wrapper methylCtools[179] (v0.9.2). Samtools[180] (v1.3) and Picard tools (v1.115) (http://broadinstitute.github.io/picard) were used for converting, merging and indexing of the alignment files. SNP aware realignment to identify single nucleotide polymorphisms (SNPs) for accurate identification of methylated cytosines and methylation calls were performed with the bisulfite SNP calling software Bis-SNP[181].

MethylKit[182] (v1.3.1) was used for the detection of differentially methylated sites. After both the strands were merged, methylation calls were filtered to include only those sites with at least 5x coverage. To determine the differentially methylated regions, 1000 base pair non-overlapping tiles were used. Differentially methylated sites were investigated in the 1000 bp tiles having at least 2 CpGs and a minimum average coverage of 5 across all the samples. Mitochondria, X and Y chromosomes were not excluded from the data. The resulting differentially methylated regions (DMRs) detected in the above analysis were annotated to Gencode gene models with the help of bedtools[183] (v2.20.1). Linear regression analysis was performed to investigate the age-dependent changes in the DMRs.

2.2.16 ATAC-seq analysis

The ATAC-seq library was prepared as described (Section 2.2.10). The sequencing was performed by Dr. Gilles Gasparoni on Illumina HiSeq 2500 sequencing system. Processing of the reads and subsequent data analysis were performed in the lab of Prof. Dr. Jörn Walter by Abdulrahman Salhab (University of Saarland, Saarbrücken).

The adapter sequence and 3' ends with base quality (PHRED score) of less than 20 in the FASTQ files obtained from the sequencing were trimmed with Trim Galore (v0.4.2) software. (Following adapter trimming and removing low quality nucleotides, the FASTQ files were mapped to the mouse reference genome (GRCm38/mm10) using the GEM[184] mapper. Duplicated reads found after alignment with GEM mapper were annotated with Picard tools (v1.115) (http://broadinstitute.github.io/picard). MACS2[185] (v2.1.0) was used to call Nucleosome Depleted Regions (NDRs). The parameters used in the MACS2 were: –shift -100, –extsize 200, –nomodel and –keep-dup all. TCseq, an R based package to analyze the sequencing data over a time course, was used to visualize age-dependent changes in the chromatin accessibility.

2.2.17 Western blotting

2.2.17.1 Preparation of brain lysates

Radioimmunoprecipitation assay buffer (RIPA buffer), which enables quick and efficient disruption of cell membrane, was used to prepare protein lysates from brain tissues of mice aged 2 and 18 months. RIPA buffer was prepared according to the following composition:

50 mM Tris HCl (pH 8)
150 mM NaCl
1% IGEPAL CA-630
0.5% Sodium deoxycholate
0.1% SDS
1 mM EDTA
Double-distilled water

A tablet of cOmplete™ Mini protease inhibitor cocktail was freshly added to 10 mL RIPA buffer before adding the brain tissue. The brains were dissected out from the sacrificed mice and immediately washed with ice-cold 1X DPBS. Using a sharp scalpel, the brain was dissected into two hemispheres. One hemisphere was transferred to an empty 2 mL tube, snap frozen in liquid nitrogen and stored at –80°C. The other hemisphere was transferred to a round-bottom tube containing 1 mL RIPA buffer. The tissue was homogenized mechanically with Polytron (2 x 20 seconds) and the tubes containing homogenized suspension was incubated on ice for 15 minutes. The tubes were centrifuged for 30 minutes at full speed in the cold room (4°C). The supernatant containing proteins was transferred to a fresh 2 mL tube and the pellet containing debris was discarded. The protein concentration in the lysate was measured using Bradford reagent and the lysate was stored at –80°C.

2.2.17.2 Western blotting

Lysates containing 30 µg protein from 2 and 18 months-old mice brains were mixed with loading buffer and incubated at 98°C on a heat block for 5 minutes, followed by incubation on ice for 5 minutes. The lysates were loaded on polyacrylamide gel (5% stacking, 12% resolving). Proteins were separated by SDS/PAGE (90V for 30 minutes, 110V for 60 minutes, 130V for 30 mins) and transferred onto 0.45 µm polyvinylidene difluoride transfer membrane using Bio-Rad transfer system (0.1 Ampere, 60 minutes).

For immunoblotting, the membranes were blocked in 5% nonfat dried milk in TBST on a shaking platform for 60 minutes and washed three times with 1X TBST. The membranes were incubated with corresponding primary antibodies overnight at 4°C (Aplnr – 1:300, Cldn5 – 1:300, Itm2a – 1:500, Gapdh – 1:50,000). Following incubation with primary antibodies, the membranes were washed three times with 1X TBST and incubated with corresponding HRP-conjugated secondary antibodies for 60 minutes at room temperature (anti-rabbit HRP-linked – 1:10,000, anti-mouse HRP-linked – 1:10,000). After washing the membranes three times with 1X TBST, Immobilon western chemiluminescent HRP substrate was added to the membranes. Membranes were imaged in the Fusion SL documentation system and quantification was performed using Fusion FX software (Vilber). Gapdh was used as loading control. For comparison, the expression levels of Aplnr was normalized to the expression levels of Gapdh in each sample.

Chapter 3

Results

Chapter 3

Results

3.1 Cerebral bleedings increase with age in wild-type mice.

Brains dissected from both wild-type mice and mice having floxed, yet non-recombined *Srf* and *Mrtf* alleles, thereby having functional *Srf* and *Mrtf* genes (wild-type phenotype) of different ages show an increase in the number of bleedings with advancement of age (Figure 3.1). The bleedings were of different sizes, observed in all regions of the brain and were not restricted to any specific region. The number of unique bleedings in a mouse brain was quantified by observing the leakage of erythrocytes, stained pink in the H&E staining, into the brain parenchyma.

The average number of bleedings recorded per brain in the 2 months-old mice (number of mice used in this age-group, n = 4) is 1.75 with a standard deviation (sd) of 0.96. In 6 months (n= 11), 12 months (n=11), 15 months (n=4) and 25 months-old mice (n=3), the average numbers of bleeding recorded are 2.73 (sd = 1.56), 7.72 (sd = 1.35), 13.75 (sd = 0.96) and 17 (sd = 1), respectively. One-way analysis of variance (ANOVA), followed by Tukey's HSD test were performed to compare all the possible pairs and test the statistical significance (Figure 3.1C). While there is no significant increase in the number of bleedings in the brains of the 6 months-old mice compared to the 2 months-old mice (adjusted p-value = 0.73), there is a significant increase in the bleedings that occur in the 12 months and 15 months-old mice, compared to the 2 months-old mice (adjusted p-value < 0.001).

These results suggest that the mice develop an age-dependent increase in the number of bleedings in the brain – with the incidence of increase becoming significantly higher after the age of 6 months.

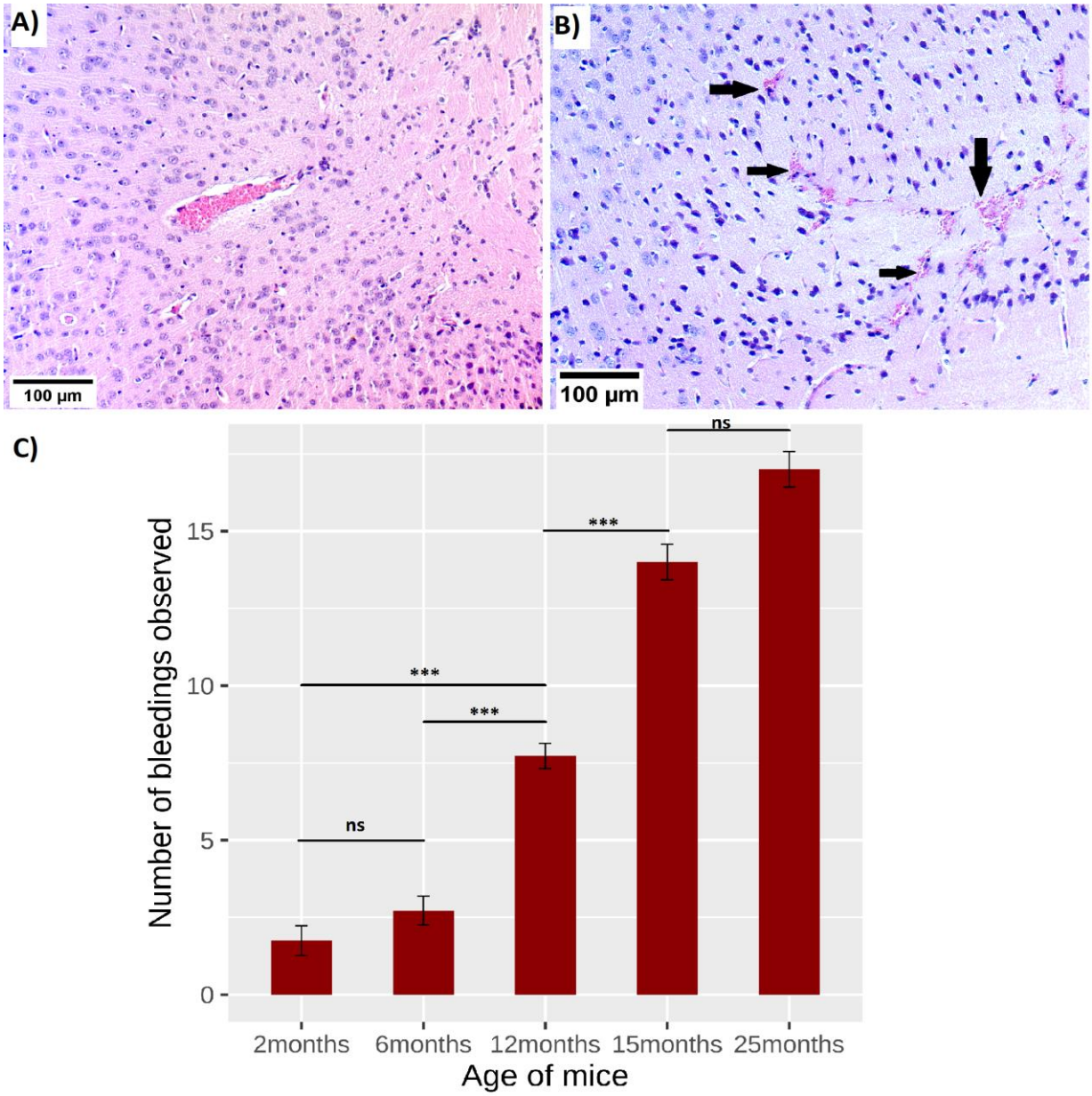

Figure 3.1 | The number of bleedings in the brain of mice increase with age. **(A)** An intact blood vessel. **(B)** bleedings from a blood vessel and the leakage of erythrocytes (arrows) stained pink by H&E stain in the brain parenchyma. **(C)** Quantification of bleedings indicates an age-dependent increase in the number of bleedings in the brain. The average number of bleeding recorded per brain in 2 months-old mice (number of mice, n = 4) is 1.75. In 6 months (n= 11), 12 months (n=11), 15 months (n=4) and 25 months-old mice (n=3), the average numbers of bleeding recorded are 2.73, 7.72, 13.75 and 17, respectively. Error bars represent mean ± se (standard error of the mean). One-way analysis of variance (ANOVA), followed by Tukey's HSD test were performed to compare all the possible pairs. (**ns** : non-significant, ******* : $p < 0.001$)

3.2 Cerebral microbleeds increase with age in wild-type mice.

Brains dissected from both wild-type mice and mice having floxed, yet non-recombined *Srf* and *Mrtf* alleles, thereby having functional *Srf* and *Mrtf* genes (wild-type phenotype) of different ages also show an increase in the number of smaller microbleeds with advancement of age (Figure 3.2). These smaller microbleeds were characterized by the presence of smaller number of erythrocytes (2-5) in the brain tissue and were observed in all regions of the brain. The number of unique bleedings in a mouse brain was quantified by observing the leakage of erythrocytes, stained pink in the H&E staining, into the brain parenchyma. Due to the very small size of a microbleed and a large number of slides per brain, the unique microbleeds were quantified every tenth slide, and the numbers do not represent the absolute number of microbleeds present in the brain.

The average number of microbleeds recorded per brain, quantified every 10^{th} slide, in the 2 months-old mice (number of mice used in this age-group, n = 4) is 4.5 with a standard deviation (sd) of 1.29. In 6 months (n= 8), 12 months (n=8) and 15 months (n=4), the average numbers of bleeding recorded are 8.75 (sd = 2.39), 13 (sd = 2.62) and 18.5 (sd = 3.11), respectively. One-way analysis of variance (ANOVA), followed by Tukey's HSD test were performed to compare all the possible pairs and test the statistical significance (Figure 3.2C). While there is no significant increase in the number of bleedings in the brains of the 6 months-old mice compared to the 2 months-old mice (adjusted p-value = 0.29), there is a significant increase in the bleedings that occur in the 12 months and 15 months-old mice, compared to the 2 months-old mice (adjusted p-value < 0.001).

These results suggest that beside larger bleedings, the mice also develop an age-dependent increase in the number of microbleeds in the brain – with the incidence of increase becoming significantly higher in mice older than 6 months.

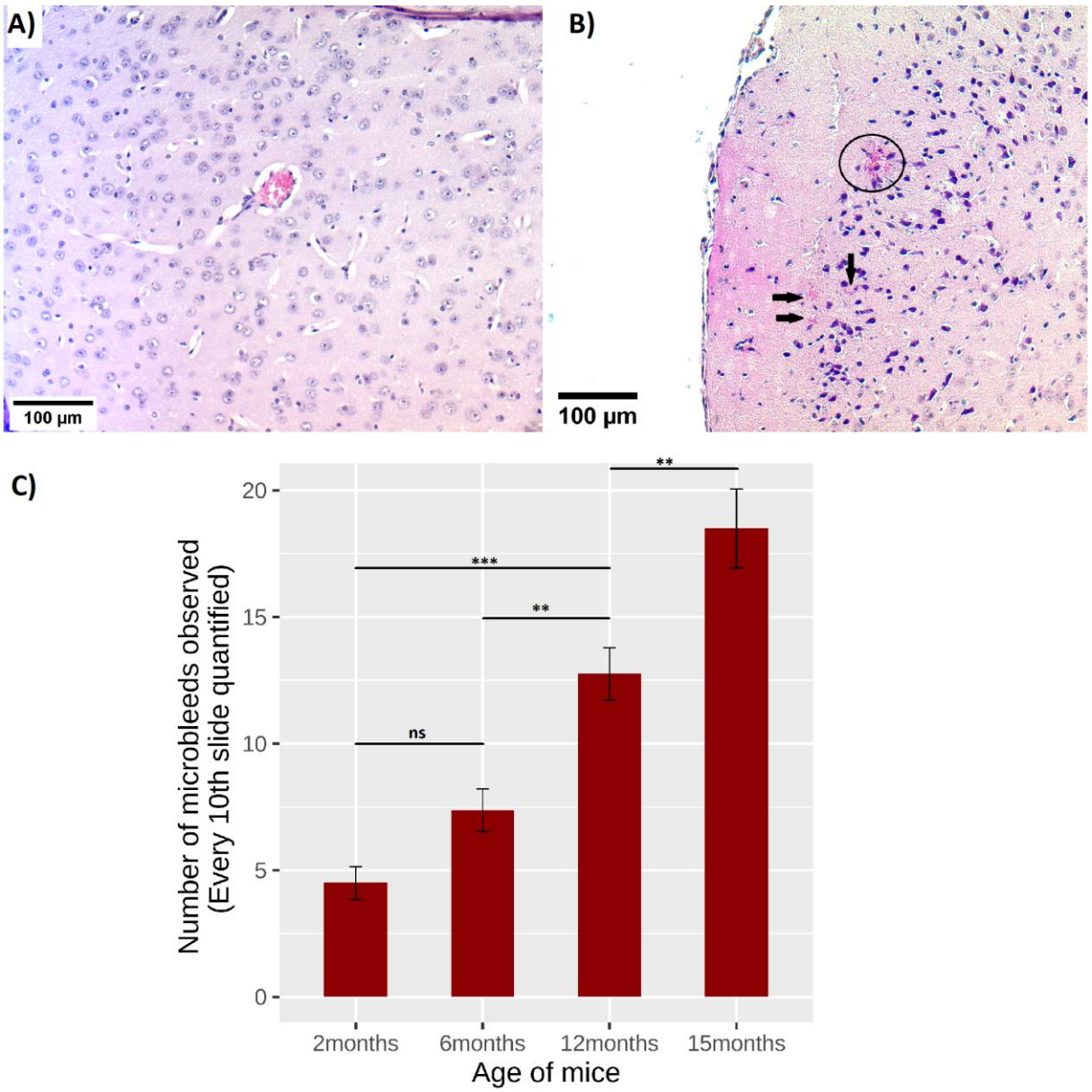

Figure 3.2 | The number of smaller microbleeds in the brain of mice increases with age. **(A)** An intact smaller blood vessel in the mouse brain. **(B)** microbleed from a blood vessel and the leakage of erythrocytes (arrows) stained pink by H&E stain in the brain parenchyma. A larger bleeding is encircled for comparison. **(C)** Quantification indicates an age-dependent increase in the number of microbleeds in brain. The average number of microbleeds recorded (every 10th slide was quantified) per brain in 2 months-old mice (number of mice, n = 4) is 4.5. In 6 months (n= 8), 12 months (n=8) and 15 months-old mice (n=4), the average numbers of microbleeds (every 10th slide was quantified) are 8.75, 13 and 18.5, respectively. Error bars represent mean ± se (standard error of the mean). One-way analysis of variance (ANOVA), followed by Tukey's HSD test were performed to compare all the possible pairs. (**ns** : non-significant, ****** : $p<0.01$, ******* : $p < 0.001$)

3.3 Isolation of pure population of endothelial cells from Cdh5-mT H2B-GFP mice using FACS.

To isolate a pure population of endothelial cells from murine brains, Cdh5-mT H2B-GFP transgenic mice were used that express membrane-targeted tdTomato (mT) and a fusion protein histone2B-GFP (H2B-GFP) under pan-endothelial vascular endothelial cadherin (Cdh5) promoter. These mice express red fluorescence in the cell membrane (membrane-targeted tdTomato) and green fluorescence in the nuclei (H2B-GFP) of ECs in all the organs.

Analysis of single-cell suspensions prepared from the brains of transgenic animals using FACS showed the presence of a cell population positive for both GFP and tdTomato, comprising approximately 7% of the cells in single-cell suspension. This double-positive GFP^+ $tdTomato^+$ cell population was absent in the single-cell suspension prepared from wild-type, non-transgenic mouse brains. The cells that were double-positive for GFP and tdTomato were sorted using FACS (Figure 3.3 A, B). To ascertain the purity of the sorted cell population, reanalysis was performed using FACS where the sorted cells are passed through the cytometer and sorted again. Reanalysis of the sorted cell population confirmed the purity of ECs to be approximately 99% (Figure 3.3 C).

The transcriptomics data obtained from RNA-sequencing of the GFP^+ $tdTomato^+$ sorted cells was used to compare the relative transcript levels of specific markers for various cells of the neurovascular unit and the brain. The expression levels of marker genes specific to endothelial cells (*Slco1a4*, *Slc1a2*, *Cldn5*, *Flt1* and *Vwa1*) were compared with the expression levels of marker genes specific to pericytes (*Pdgfrb*, *Mcam*, *Abcc9*, *Kcnj8* and *Cspg4*), astrocytes (*Slc1a2*, *Aqp4*, *Gfap*, *S100b* and *Aldh1l1*), microglia (*Tmem119*, *Cx3cr1*, *Aif1*, *Ptprc* and *Itgam*), oligodendrocytes (*Olig1*, *Mog*, *Olig2*, *Cldn11* and *Olig3*), neurons (*Eno2*, *Syp*, *Syt1*, *Rbfox3* and *Dlg4*) and Schwann cells (*Mobp*, *Mag*, *Gap43* and *Mpz*). The transcripts of EC-specific markers are very highly expressed (normalized counts > 100,000) in the population of sorted cells while the expression levels of the transcripts of markers of other cells of the neurovascular unit and brain are low (normalized counts ~ 1000) to absent (Figure 3.4).

The results of FACS-based reanalysis of sorted cell population and comparison of the expression of transcript levels of marker genes of various cell types confirm that the sorted

cells consist of about 99% pure EC population (purity determined by reanalysis of the sorted cells), and the contamination of other cells of brain such as pericytes, astrocytes, oligodendrocytes, microglia, neurons or Schwann cells in the sorted cells is approximately 1%.

Pure population of ECs was isolated from the single-cell suspension prepared from the brains of mice of different ages (2 months, 6 months, 12 months, 18 months and 24 months) for downstream analysis such as RNA-seq, ATAC-seq and RRBS.

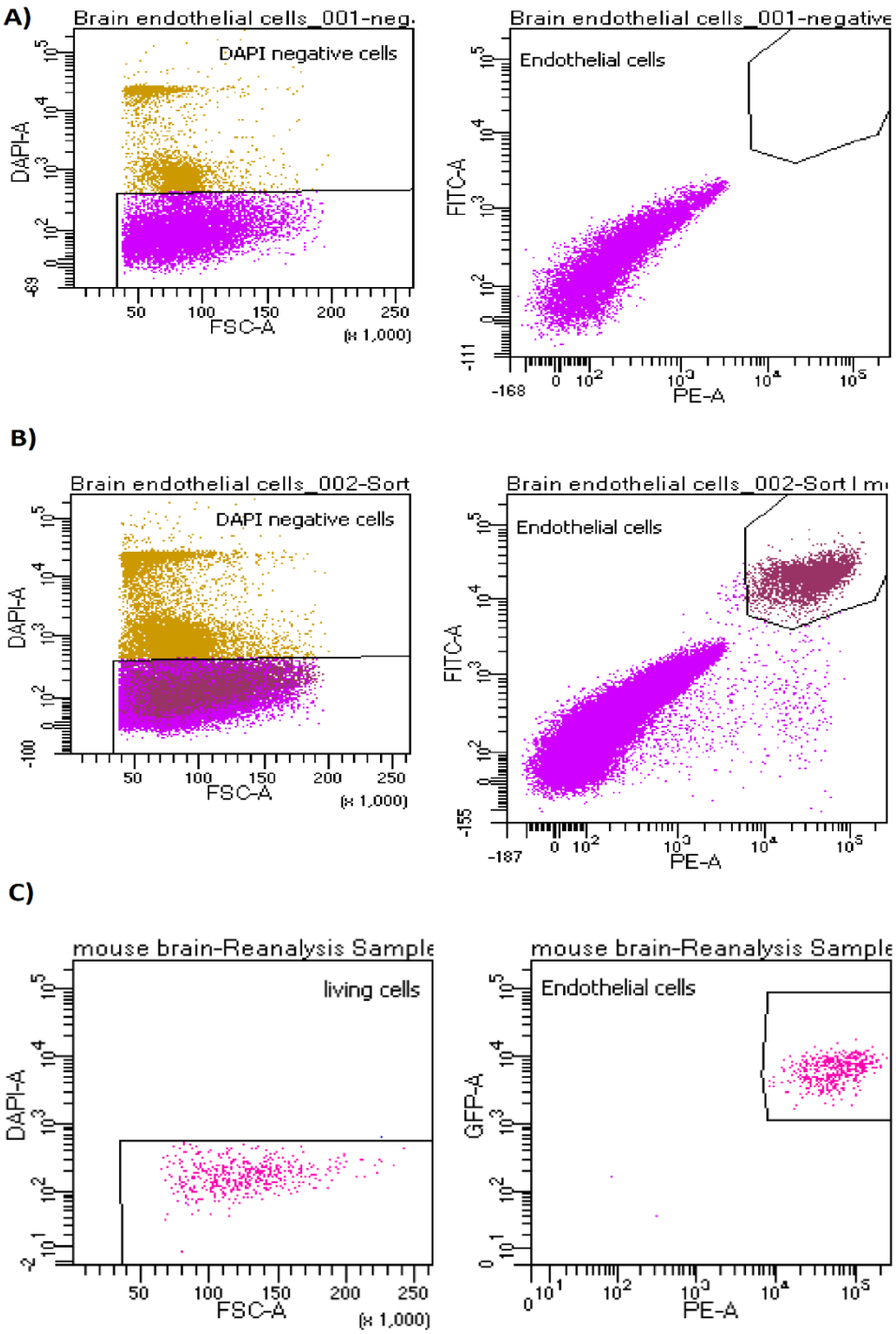

Figure 3.3 | FACS profile of sorted ECs. (A) The single-cell suspension prepared from a wild-type mouse brain does not show a population of cells positive for GFP and tdTomato, **(B)** while the single-cell suspension prepared from Cdh5-mT H2B-GFP transgenic mouse brain shows the presence of EC population double positive for GFP and tdTomato fluorescence. **(C)** The double positive cells (GFP^+ $tdTomato^+$) were sorted. The purity of sorted ECs was ~ 99% as confirmed by the reanalysis of the sorted cells.

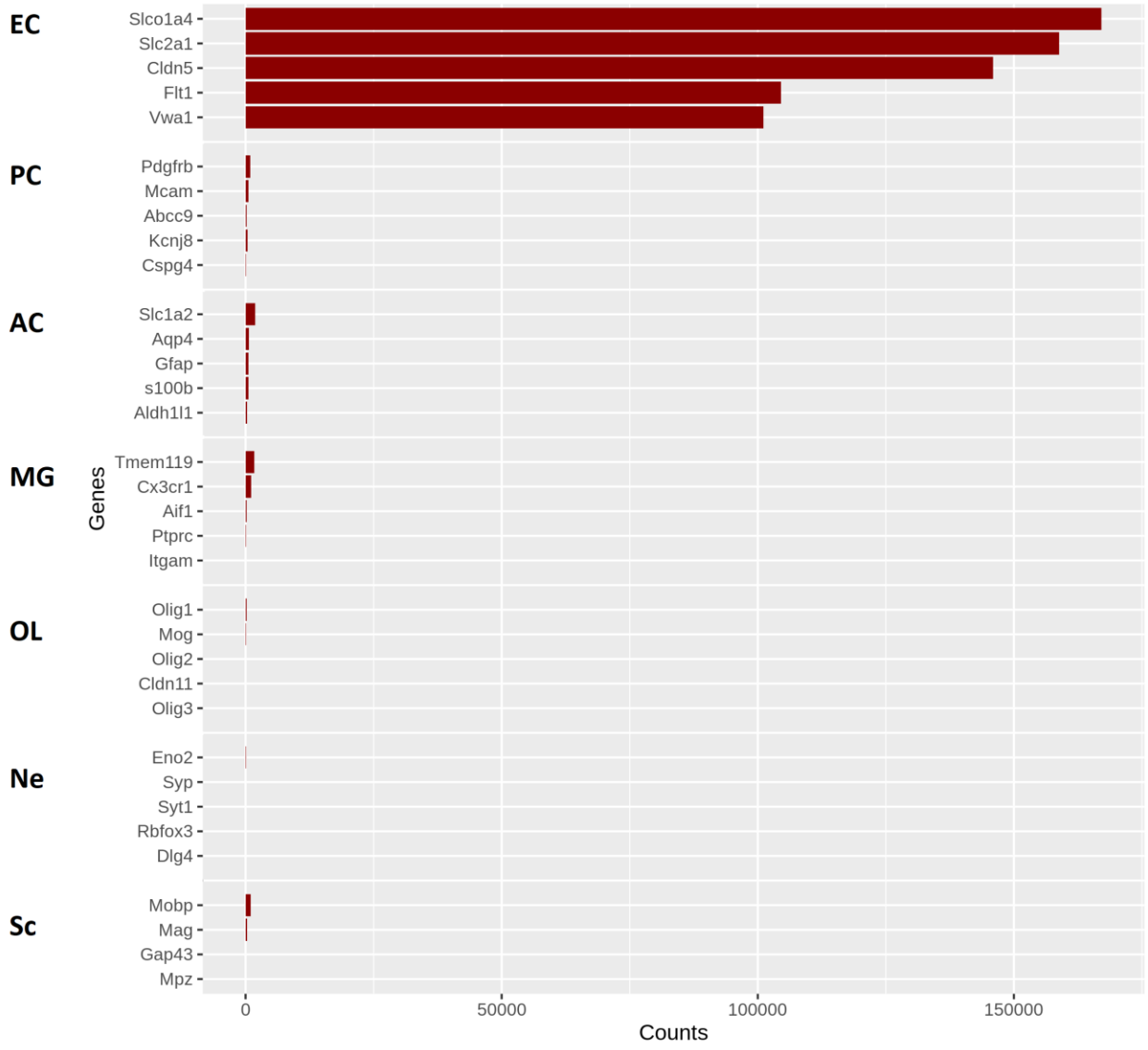

Figure 3.4 | The relative transcript levels of specific markers for various cells of the neurovascular unit and the brain. The specific markers for endothelial cells (ECs) are very highly enriched in comparison to the markers for other cells of the neurovascular unit, confirming the purity of the ECs sorted. (EC – endothelial cells, PC – pericytes, AC – astrocytes, MG – microglia, OL – oligodendrocytes, Ne – neurons, Sc – Schwann cells)

3.4 Number of ECs isolated from the mouse brain decrease with age.

The yield of endothelial cells from the brains of mice decreases with age. While an average of 220559 (sd = 52741) ECs were sorted from a brain of a 2 months-old mice (number of mice, n = 12), the number of ECs sorted from the brain of a 6 months-old (n=12), 12 months-old (n=18), 18 months-old (n=16) and 24 months-old mice (n=6) were 165505 (sd = 77175), 160108 (sd = 70983), 103516 (sd = 49352) and 112745 (sd = 26225), respectively (Figure 3.5). Whether the age-dependent decrease in the yield of ECs from brains of mice is due to the reduction in the number of ECs in the brains of ageing mice or because of technical reasons, such as varying efficiency of reagents for preparing single-cell suspension and the EC-isolation protocol from the mice of different ages was not investigated (discussed in section 4.3).

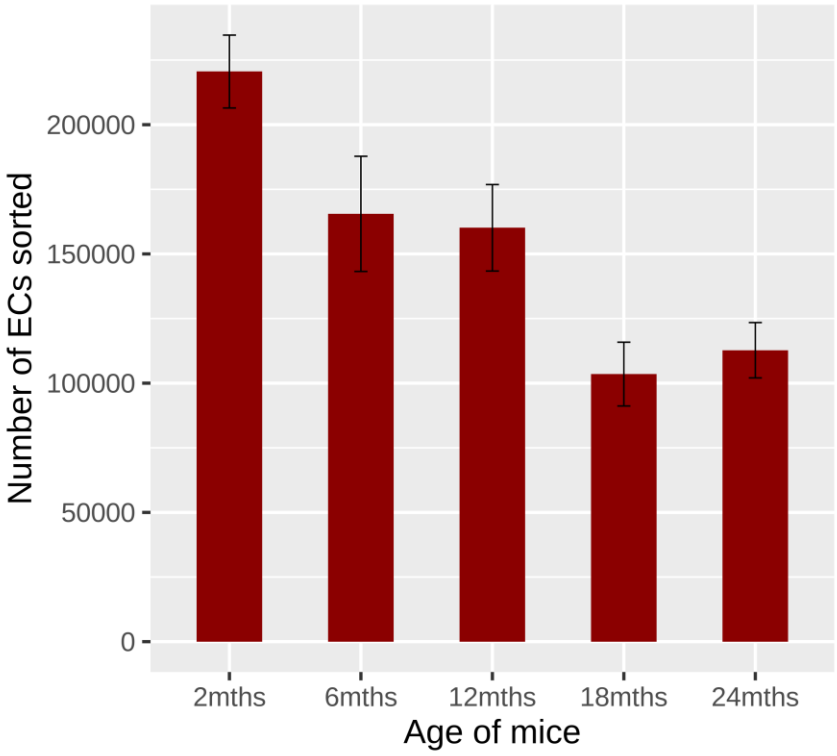

Figure 3.5 | The number of ECs isolated from (each brain of) mice belonging to different age. The yield of ECs sorted from the brain of older mice is less than the yield from younger mice. The average numbers of ECs sorted from each brain of a 2 months-, 6 months-, 12 months-, 18 months- and 24 months-old mouse were 220559 (sd = 52741), 165505 (sd = 77175), 160108 (sd = 70983), 103516 (sd = 49352) and 112745 (sd =26225), respectively. Error bars represent mean ± se (standard error of the mean).

3.5 The weights of various organs in mice do not change with age.

Before sacrificing the mice for isolation of the ECs, the body weight of each mouse was recorded (n = 6 males and 6 females of each age-group). An increase in the body weight of 6 months-old mice is observed in comparison to 2 months-old mice; however, there is no further significant change in the body weight of mice after the age of 6 months. The males of each age group have a slightly higher body weight than the females of the same age group.

The brain, heart and lungs of the mice were also weighed and recorded (Table 3.1). It was observed that the weights of the brains, lungs and heart do not change with age in mice. Apart from the 24 months-old mice, where the males and females show a significant difference in the weight of heart, no difference was observed in the weights of other organs among different age-groups (Figure 3.6). Also, no clear differences in the weights of various organs between males and females were observed. These observations suggest that ageing does not have any significant effect on the weights of various organs in mice.

Age	**Sex**	**Body weight (gram) Mean ± sd**	**Brain weight (gram) Mean ± sd**	**Heart weight (gram) Mean ± sd**	**Lungs weight (gram) Mean ± sd**
2 months	Male	25.76 ± 1.87	0.451 ± 0.046	0.165 ± 0.026	0.222 ± 0.031
	Female	21.64 ± 3.20	0.43 ± 0.217	0.171 ± 0.039	0.222 ± 0.057
6 months	Male	37.66 ± 3.31	0.438 ± 0.029	0.242 ± 0.036	0.248 ± 0.034
	Female	27.39 ± 1.86	0.443 ± 0.026	0.171 ± 0.049	0.223 ± 0.037
12 months	Male	38.18 ± 2.99	0.446 ± 0.029	0.25 ± 0.044	0.275 ± 0.028
	Female	30.41 ± 1.41	0.462 ± 0.022	0.214 ± 0.024	0.232 ± 0.030
18 months	Male	38.71 ± 3.68	0.442 ± 0.011	0.23 ± 0.081	0.256 ± 0.037
	Female	31.175 ± 3.65	0.478 ± 0.025	0.21 ± 0.051	0.237 ± 0.005
24 months	Male	35.46 ± 2.33	0.446 ± 0.02	0.315 ± 0.035	0.245 ± 0.035
	Female	33.04 ± 3.16	0.47 ± 0.026	0.216 ± 0.032	0.266 ± 0.032

Table 3.1 | Weights of different organs of mice belonging to different age-groups. The table contains the means and standard deviations of the body weights, weights of brain, heart and lungs of mice belonging to different age and sex. (n = 6 males and 6 females for the 2 months, 6 months, 12 months and 18 months-old cohorts ; n= 3 males and 3 females for the 24 months-old cohort).

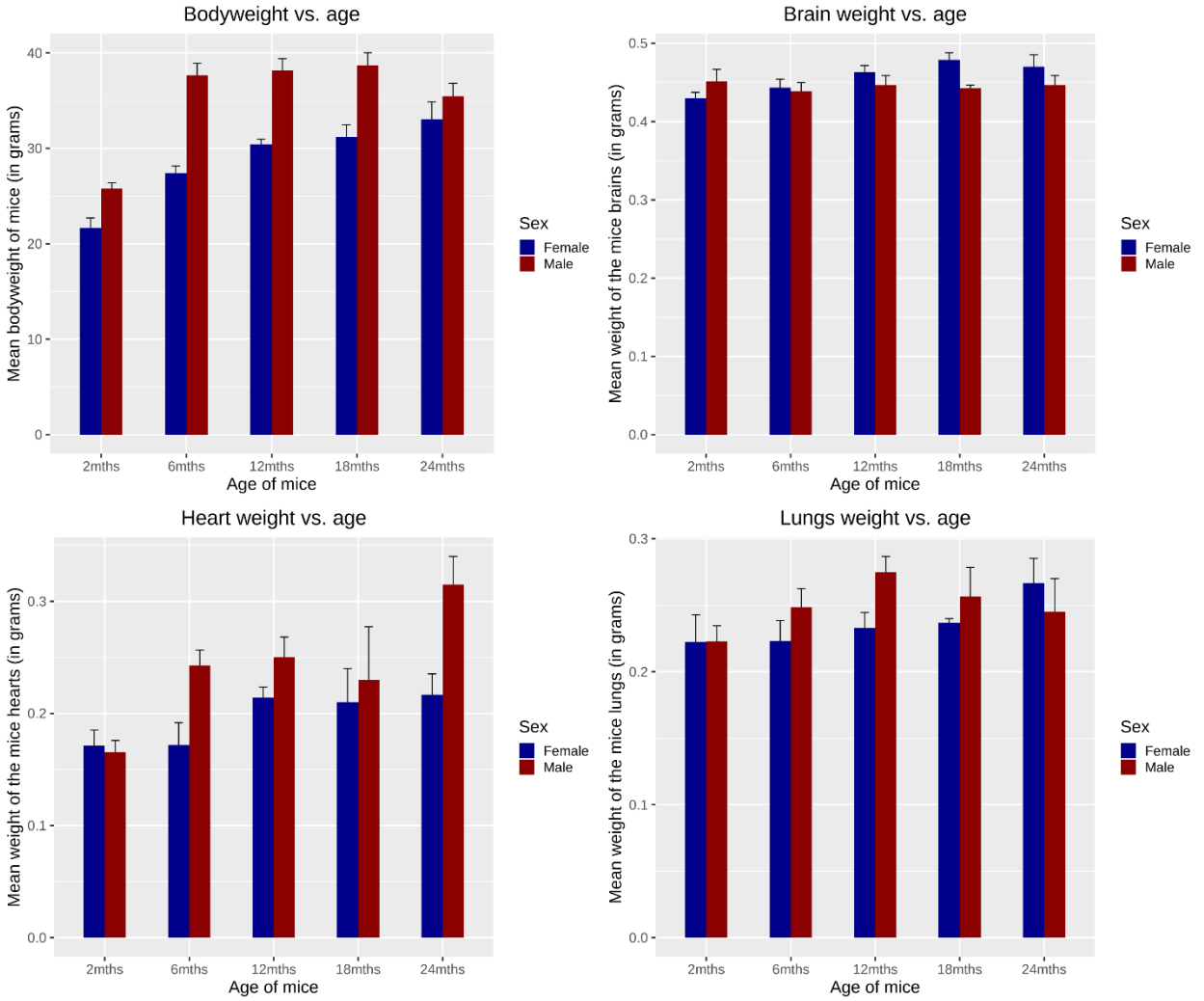

Figure 3.6 | Weight of body, brain, heart and lungs of mice as a function of age. The body weight of mice increases in the 6 months-old group as compared to the 2 months-old mice; however, there is no further significant change in the body weight of mice after the age of 6 months. Similarly, ageing has no effect on the weights of brains, lungs and heart in the mice as the weights of these organs do not change significantly with age. Error bars represent mean mean ± se (standard error of the mean). The mean weights and standard deviation (sd) of each group is summarized in Table 3.1. (n = 6 males and 6 females for the 2 months, 6 months, 12 months and 18 months-old cohorts ; n= 3 males and 3 females for the 24 months-old cohort).

3.6 The sequencing reads have consistently high quality across all the samples.

RNA-seq analysis of ECs purified from mice of 2, 6, 12, 18 and 24 months was performed to investigate the age-dependent changes in the transcriptome that may be a potential contributor to the incidents of age-dependent increase in cerebral bleedings in mice. Three males and three females belonging to each of the above-mentioned age-groups were used for the RNA-seq analysis.

The raw sequencing files from RNA sequencing were obtained as FASTQ files and the quality control checks on the raw RNA-seq data were performed using FASTQC. The average per base sequence quality scores (Phred quality score) across all nucleotide positions in all the samples were greater than 30, indicating a very high quality of sequencing. The Phred quality score Q is defined by $Q = -\log_{10}P$ (where P is the probability that an individual nucleotide has been incorrectly called in the sequencing). A Phred score of 30 means the probability that an individual nucleotide has been incorrectly called is 0.001. The per sequence quality scores also showed consistently high score (mean score > 28) across all the samples, indicating the high quality of the sequencing reads (Figure 3.7).

The 3' adapter sequences in the obtained sequencing reads were trimmed using Cutadapt, a command-line tool and were aligned to the mouse reference genome (GRCm38/mm10) using STAR (Spliced Transcripts Alignment to a Reference), an ultrafast universal RNA-seq alignment software[175]. An average of 85.99 % of all the RNA-seq reads across all the thirty samples mapped uniquely to the mouse genome and were subsequently used for the differential expression analysis to study the age-dependent changes in the transcriptome of the ECs (Figure 3.8).

Differential expression analysis was performed using DESeq2, available as an R package. DESeq2 uses a method that calculates log-fold changes in gene expression level between two conditions by fitting a generalized linear model (GLM) for each gene. Since RNA-seq experiments have a small sample size, i.e. three biological replicates per condition, the variability within the group tends to be high leading to variable dispersion estimates for each gene. The algorithm of DESeq2 assumes that the genes having similar expression levels have similar dispersion. DESeq2 uses an empirical Bayes shrinkage approach to estimate the dispersion estimate for each gene and calculate the log-fold change.

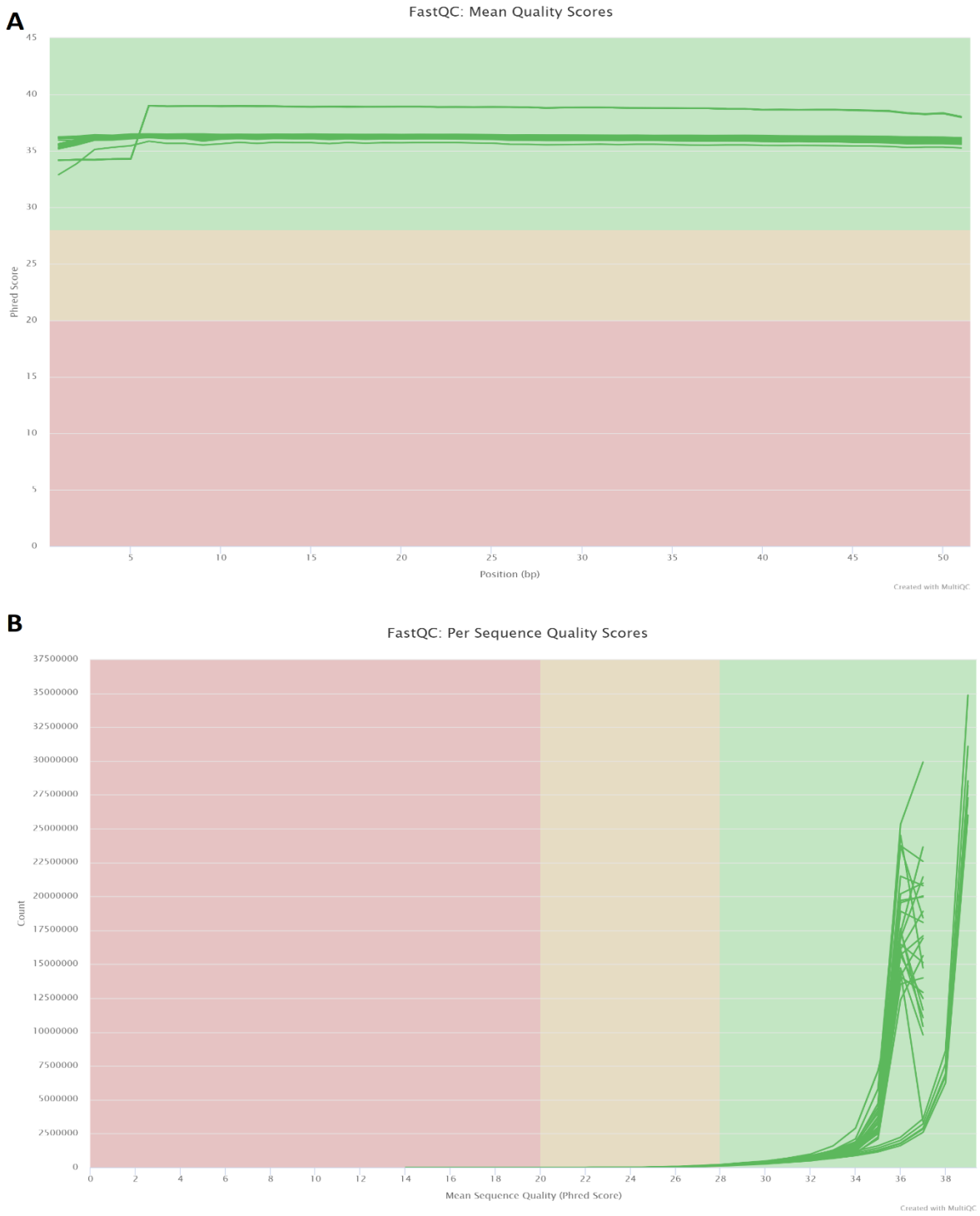

Figure 3.7 | The sequencing reads show consistently high quality across all the samples. (A) The average per base sequence quality scores across all nucleotide positions in all the samples are greater than 30. **(B)** The per sequence quality scores across all the samples are greater than 28. Both these parameters indicate a consistently high quality of the sequencing reads.

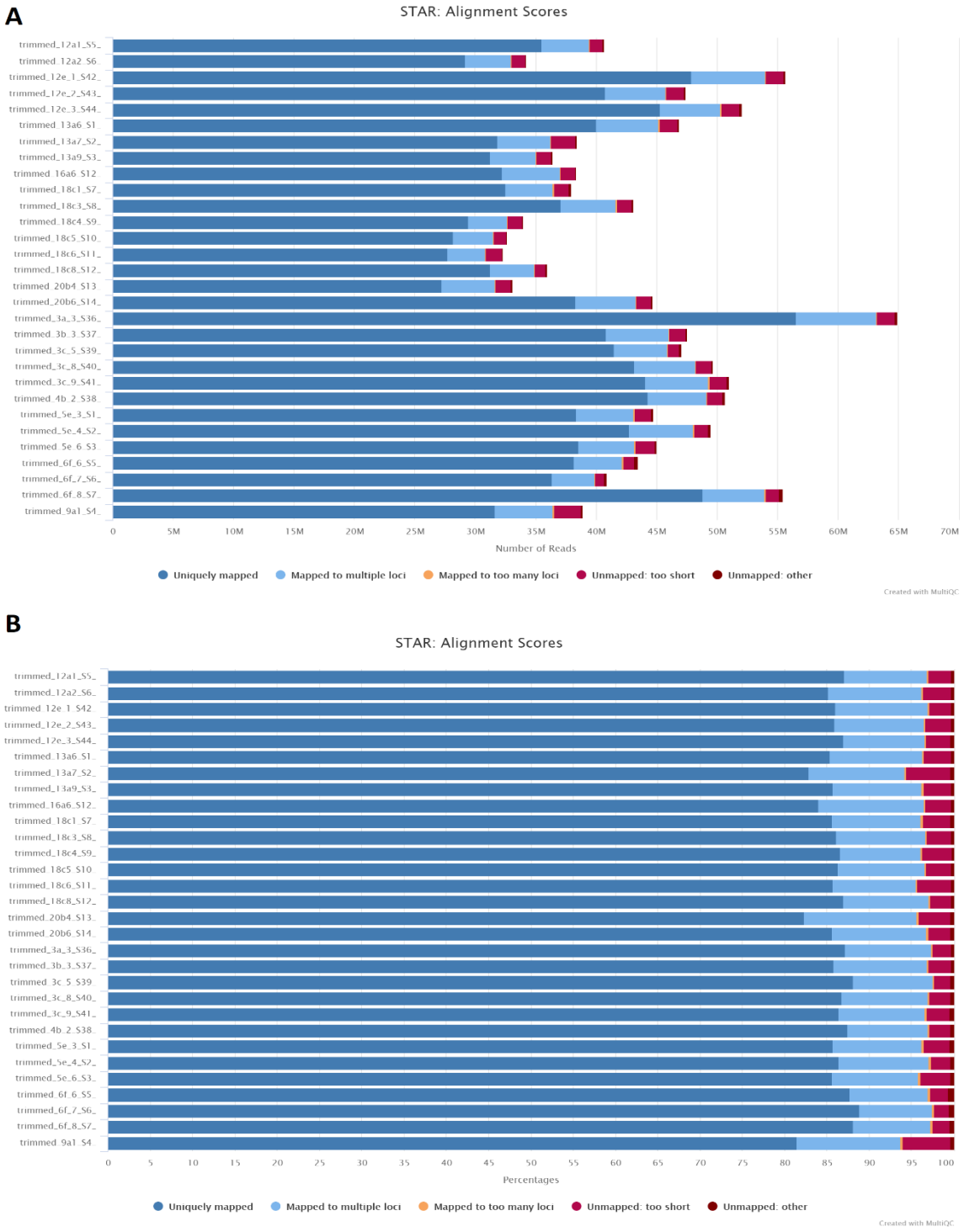

Figure 3.8 | STAR alignment statistics. (A) Number of reads across all the samples. **(B)** Percentage of reads in each sample that map uniquely, map to multiple loci, too many loci, reads that are too short and unmapped reads. An average of 85.99 % of all the RNA-seq reads across all the thirty samples map uniquely to the mouse genome.

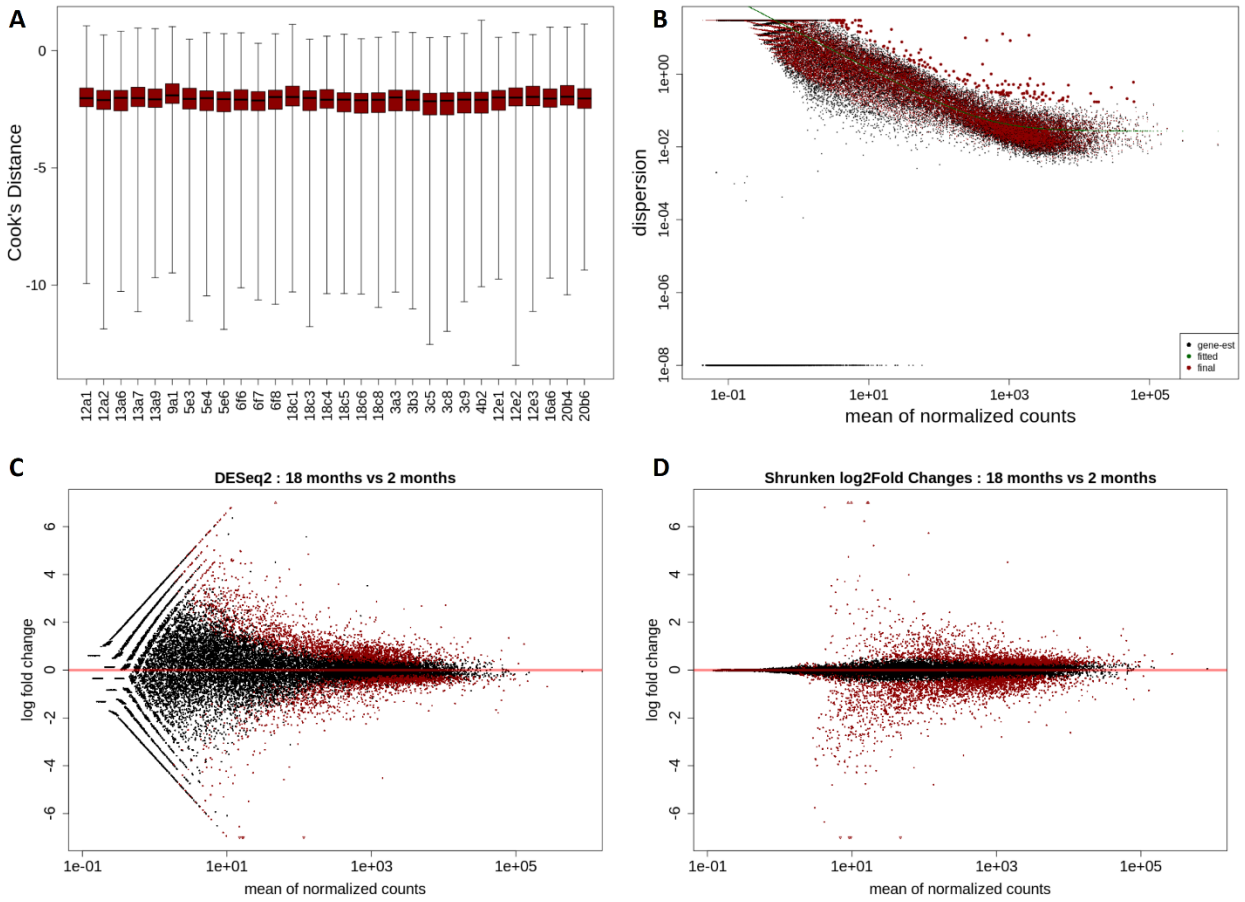

Figure 3.9 | The boxplot of Cook's distance and the dispersion plot of all the samples suggest no outliers among the samples. **(A)** All the samples used for RNA-seq study have a similar Cook's distance, indicating that there are no outliers. **(B)** The dispersion plot of the mean of normalized counts of all the genes across all the samples also suggest very few outliers. The gene-wise estimates are in black, the green line shows the fitted values and calculated final *a posteriori* estimates are shown in red. **(C)** MA-Plot shows the unshrunken log2 fold changes of genes over the mean of normalized counts. **(D)** MA-Plot shows the shrinkage of log2 fold changes due to the incorporation of zero-centered normal prior. The shrinkage for genes with low counts is higher while the shrinkage for genes with higher counts is less.

The first step involves the calculation of gene-wise maximum likelihood estimates and, accordingly, a curve is fit. The second step involves considering the fit as the prior mean, based on which the dispersion values are calculated. The dispersion plot of the mean of normalized counts of all the genes across all the samples show the gene-wise estimates, the fitted values and calculated final *a posteriori* dispersion estimates (Figure 3.9 A). The MA-plots show unshrunken log2 fold changes of genes over the mean of normalized counts and the shrinkage of log2 fold changes due to the incorporation of zero-centered normal prior. The shrinkage for genes with low counts is higher while the shrinkage for genes with higher counts is less (Figure 3.9 C and D). Cook's distance is a measure of the influence of an individual sample on the fitted coefficients for each gene and a sample having dissimilar Cook's distance compared to the other samples indicates that the sample is an outlier. The Cook's distance of all the samples used in the RNA-seq analysis is comparable (Figure 3.9A) indicating that there is no outlier among the samples.

3.7 The transcript profile of endothelial cells changes with ageing.

The principal component analysis (PCA) of the RNA-seq data obtained from the cerebral endothelial cells isolated from three male and three female mice belonging to 2, 6, 12, 18 and 24 months indicate that the transcript profile of the ECs changes with age. On average, the samples cluster together according to their age, as explained by the first principal component. Within a particular age-group, the samples cluster according to their sex, indicating that the transcript profile of ECs are different in the males and females of a particular age group.

Figure 3.10 shows the PCA plots for various groups of comparison suggesting that the first principal component (PC1), accounting for the largest variance in the data, is due to the age whereas the second principal component (PC2) that explains the factor accounting for the second largest variance in the data, is due to the sex. Figure 3.10 (A-D) shows PCA plots of pairwise comparisons between each of the 6 months-, 12 months-, 18 months- and 24 months-old samples with the 2 months-old samples, respectively. In each of the comparisons, the samples cluster very clearly according to age and sex, with the exception of sample 18c1 (2 months-old male) that shows a different profile in comparison to its 2 months-old male littermates. The largest difference in the transcript profile is observed in the 18 months-old samples (PC1 = 48%) and the least difference in the 6 months-old samples (PC1 = 38%), suggesting that the dysregulation of transcript levels in the cerebral ECs is maximum at the age of 18 months.

In the PCA plot for all the thirty samples, while the 2 months-old and 6 months-old samples cluster close to each other on the left side, the 18 months-old and 24 months-old samples cluster around each other, suggesting a difference in gene expression profile in the ECs of the young and old mice (Figure 3.10 E).

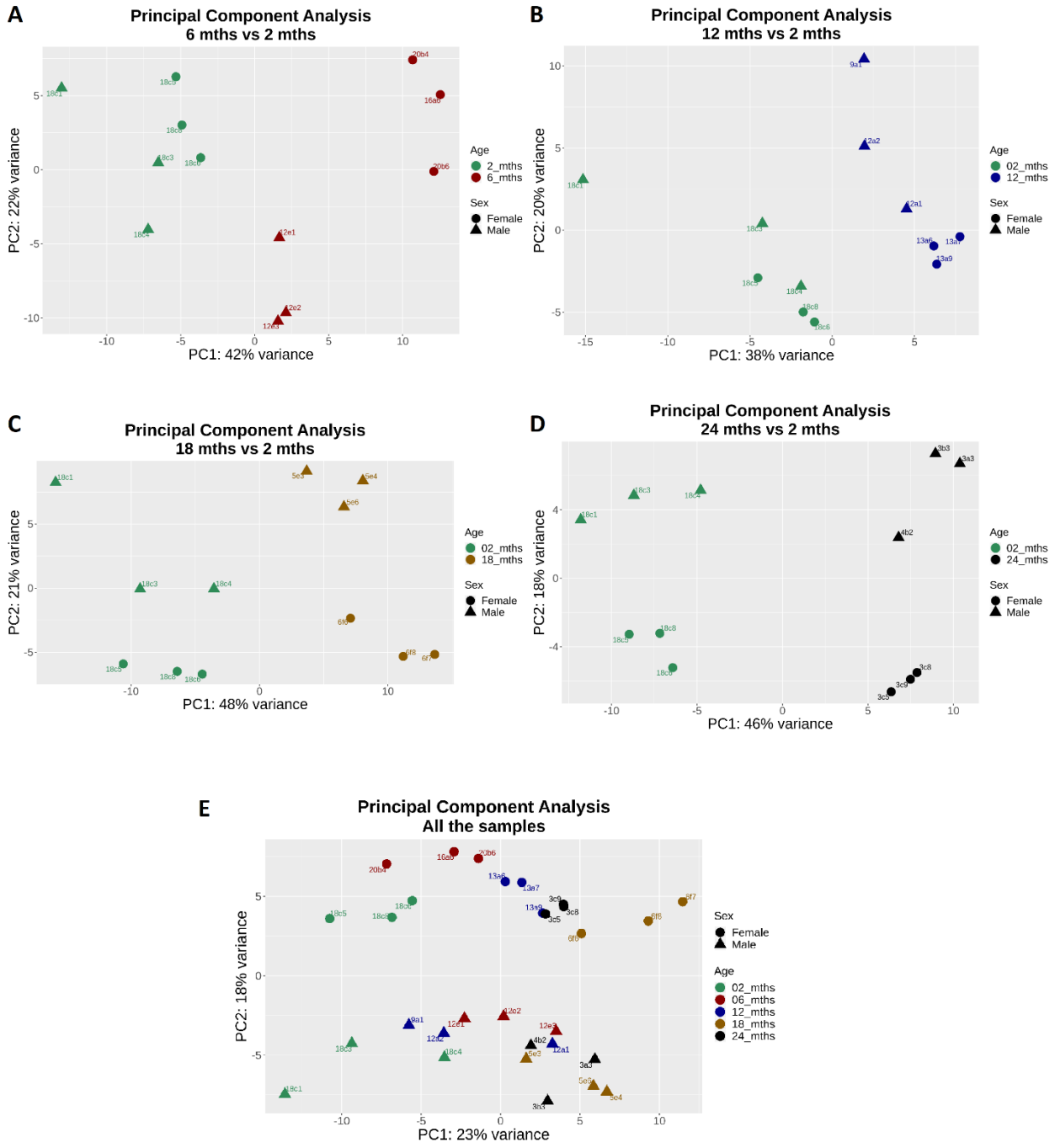

Figure 3.10 | Principal Component Analysis (PCA) plots suggest transcript profile of ECs changes with age. **(A-D)** PCA plots of RNA-seq dataset showing pairwise comparison between the 6 months, 12 months, 18 months and 24 months-old samples with 2 months-old. **(E)** PCA plot of RNA-seq dataset of all the samples. PC1: principal component 1, PC2: principal component 2.

3.8 RNA-seq data reveal age-dependent transcript level dysregulation in ECs.

The differential expression analysis for the pairwise comparisons between 6 and 2 months-old, 12 and 2 months-old, 18 and 2 months-old and 24 and 2 months-old samples were performed using DESeq2. The differential expression analyses were performed in three different conditions – a) including all the samples (three males and three females) of an age-group, b) only the males of each age-group and c) only the females of each age-group.

A total of 827 genes were significantly upregulated (log2-fold change >0 and adjusted p-value < 0.05) and 919 downregulated (log2-fold change < 0 and adjusted p-value < 0.05) in the cerebral ECs of 6 months-old mice when compared to the 2 months-old mice when the analysis was performed with mixed samples of male and female mice of 2 and 6 months-old cohorts, respectively. When only the males of these age-groups were considered, 133 genes were found to be upregulated and 256 downregulated in the 6 months-old group. In the analysis consisting only the female samples, 1861 genes were found to be upregulated and 2374 downregulated in the 6 months-old group. 404 genes were found to be significantly upregulated and 465 were significantly downregulated in the cerebral ECs isolated from 12 months-old mice. When only the males were considered, 95 genes were found to be upregulated and 77 downregulated. When the differential analysis was performed with only the females, 659 genes were upregulated and 476 downregulated.

In the RNA-seq dataset of cerebral ECs isolated from the 18 months-old mice, 2460 genes were significantly upregulated and 2085 were significantly downregulated when compared to the RNA-seq dataset of the 2 months-old group. When only the males were considered, 532 genes were found to be upregulated and 425 were downregulated. In the differential analysis consisting only the female samples, 2478 genes were upregulated and 2208 downregulated. In the 24 months-old cohort, a total of 1483 genes were significantly upregulated and 1519 were significantly downregulated. When only the males were considered for the differential expression analysis, 431 genes were found to be upregulated and 284 were downregulated. 1595 genes were upregulated and 1868 were downregulated in the analysis performed using the females only (summarized in Table 3.2).

Linear regression analysis, adjusting for the sex-specific effects, was performed on RNA-seq data for all the thirty samples across all time points (2,6,12,18 and 24 months) to identify the genes that are dysregulated with ageing. The linear regression analysis was

performed on the TPM (transcripts per million) values calculated for all the transcripts in each sample. After correcting for the multiple testing using Benjamini-Hochberg correction that accounts for the false discovery rate (FDR), 1388 genes were found to be dysregulated with age. Of these, 675 genes were found to be significantly downregulated (t.value.age < 0) while 713 were upregulated (t.value.age > 0) with age, having an adjusted p-value (p.value.age.fdr) less than 0.05.

Comparison	**Samples analyzed**	**Upregulated genes (Adjusted p-value < 0.05)**	**Downregulated genes (Adjusted p-value < 0.05)**
6 months vs. 2 months	All	827	919
	Males only	133	256
	Females only	1861	2374
12 months vs. 2 months	All	404	465
	Males only	95	77
	Females only	659	476
18 months vs 2 months	All	2460	2085
	Males only	532	425
	Females only	2478	2208
24 months vs 2 months	All	1483	1519
	Males only	431	284
	Females only	1595	1868

Table 3.2 | Summary of number of genes differentially regulated in the ageing cohorts.

Interestingly, in all the age-groups, the number of dysregulated genes in the females is much larger than the number of genes dysregulated in the males of the corresponding age-groups. The large variability in the results obtained from the differential expression analysis depending on the inclusion or exclusion of female mice can possibly be attributed to the fact that the female littermates of a particular age-group may have a different estrous cycle. The fluctuating levels of sex hormones estradiol and progesterone in female mice during the estrous cycle is known to affect the chromatin accessibility and the expression levels of various genes in the hippocampal neurons[186]. The fluctuating levels of sex hormones in the female littermates having different estrous cycles might also affect gene expression in the cerebral ECs, resulting in the differences between the transcript profiles of the males and females. Therefore, to identify the candidate genes whose dysregulation may contribute to the age-dependent increase in the incidents of cerebral bleedings, the genes found to be differentially expressed in the males were considered.

The maximum PC1 value of 48% (Figure 3.10) and the largest number of genes dysregulated in the cerebral ECs (Table 3.2) in the 18 months-old mice when compared to the 2 months-old mice suggest that the dysregulation of transcript levels in the cerebral ECs is maximum around the age of 18 months. The heat map depicting expression levels of top 500 differentially expressed genes from the RNA-seq dataset also suggests that the dysregulation of genes is maximum in the 18 months-old group and the expression pattern of the genes follow a slightly different trend in the 24 months-old group (Figure 3.11). In the heat map, each row represents a gene and each column represents a sample. The color and intensity of each box in the heat map depicts the expression level of the gene – from the lowest (deep blue) to the highest (deep red). For instance, expression of the genes in cluster 3 increases with age. The expression of the genes in this cluster is maximum at 18 months and decreases in the 24 months-old cohort. Similarly, while the genes in cluster 1 show a stronger downregulation effect in the 18 months-old cohort, the downregulation of those genes in the 24 months-old cohort is weaker. The effect may be due to an inadvertent bias resulting from selecting those ‘healthier’ mice which reach the age of 24 months. Since a large number of these mice (> 50%) died from natural ageing around the age of 19-20 months, those surviving and attaining the age of 24 months may be healthier and have a different transcript profile compared to the 18 months-old mice, thereby resulting in the bias observed in the RNA-seq data from 24 months-old cohort.

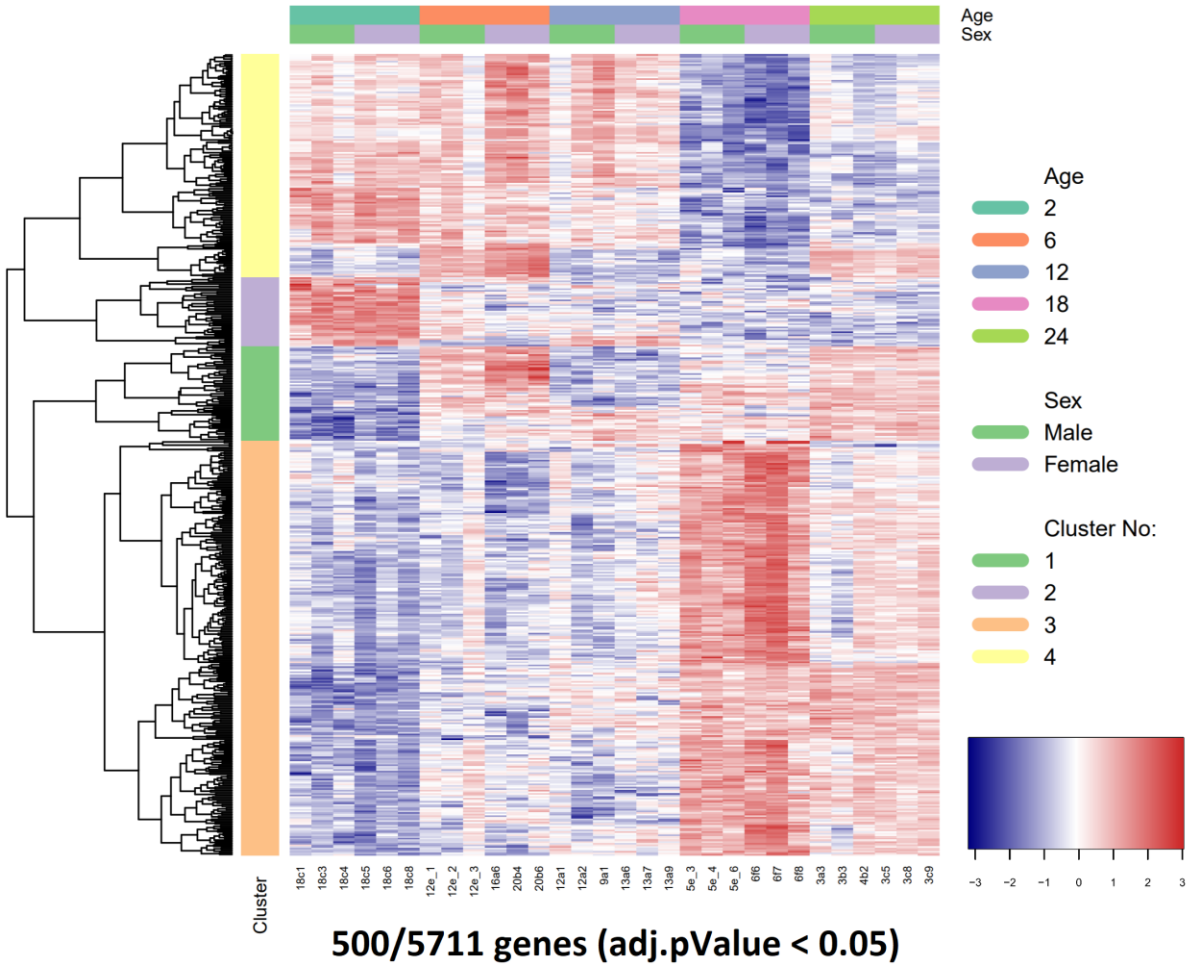

Figure 3.11 | Heat map of top 500 differentially expressed genes (adjusted p-value < 0.05). The heat map of the multivariate analysis performed on RNA-seq data of all age-groups shows the trend of top 500 differentially expressed genes across age (adjusted p-values < 0.05). The genes have been clustered according to their expression patterns across age. The largest number of genes are in cluster 3 and show a consistent upregulation with age. The expression of genes in the clusters 2 and 4 show a downregulation with age, while the genes in the cluster 1 do not show any specific trend. The expression scale shows the normalized Z-score, calculated as logarithm of counts per million (CPM) values. The dysregulation of genes is maximum in the 18 months-old group and the expression pattern of the genes follow a slightly different trend in the 24 months-old group, as evident from the higher intensity of red and blue in 18 months group. The scale extends from deep blue (-3) to deep red (3) indicating increasing level of expression of a gene. The multivariate analysis on the RNA-seq data was performed by Dr. Robert Geffers (Helmholtz Zentrum für Infektionsforschung, Braunschweig).

3.9 Gene set enrichment analysis reveals upregulation of inflammatory pathways in cerebral ECs with age.

Gene set enrichment analysis was performed using FGSEA[187], an R-package for fast pre-ranked gene set enrichment analysis (GSEA) to identify the pathways dysregulated in ageing mice. The Hallmark gene sets – that summarize and represent specific well-defined biological states or processes – from the molecular signatures database (MSigDB), was used for the analysis[188]. GSEA performed on the RNA-seq dataset comparing the 18 months-old group with the 2 months-old group (males only) revealed that several pathways implicated in inflammatory response were significantly upregulated (adjusted p-value < 0.05) with ageing. These include the pathways involving interferon alpha response, interferon gamma response, allograft rejection and TNFα signaling via NF-κB. Among the other pathways that were found to be significantly upregulated in the cerebral ECs of 18 months-old mice were apoptosis and dysregulation of pathways involved in response to ultraviolet (UV) radiation. The pathways that were significantly downregulated (adjusted p-value < 0.05) in the 18 months-old mice include pathways associated with oxidative phosphorylation, fatty acid metabolism and MTORC1 signaling (Figure 3.12).

The GSEA performed on the RNA-seq dataset comparing 24 months-old group with 2 months-old group (males only) yielded similar results, indicating that the pathways dysregulated in 18 and 24 months-old mice are comparable. The pathways implicated in inflammatory responses such as response to interferon alpha, response to interferon gamma, allograft rejection and TNFα signaling via NF-κB are significantly upregulated in the 24 months-old group (adjusted p-value < 0.05). Also, the pathways involved in oxidative phosphorylation and MTORC1 signaling are significantly downregulated (adjusted p-value < 0.05) in the 24 months-old group (Figure 3.13).

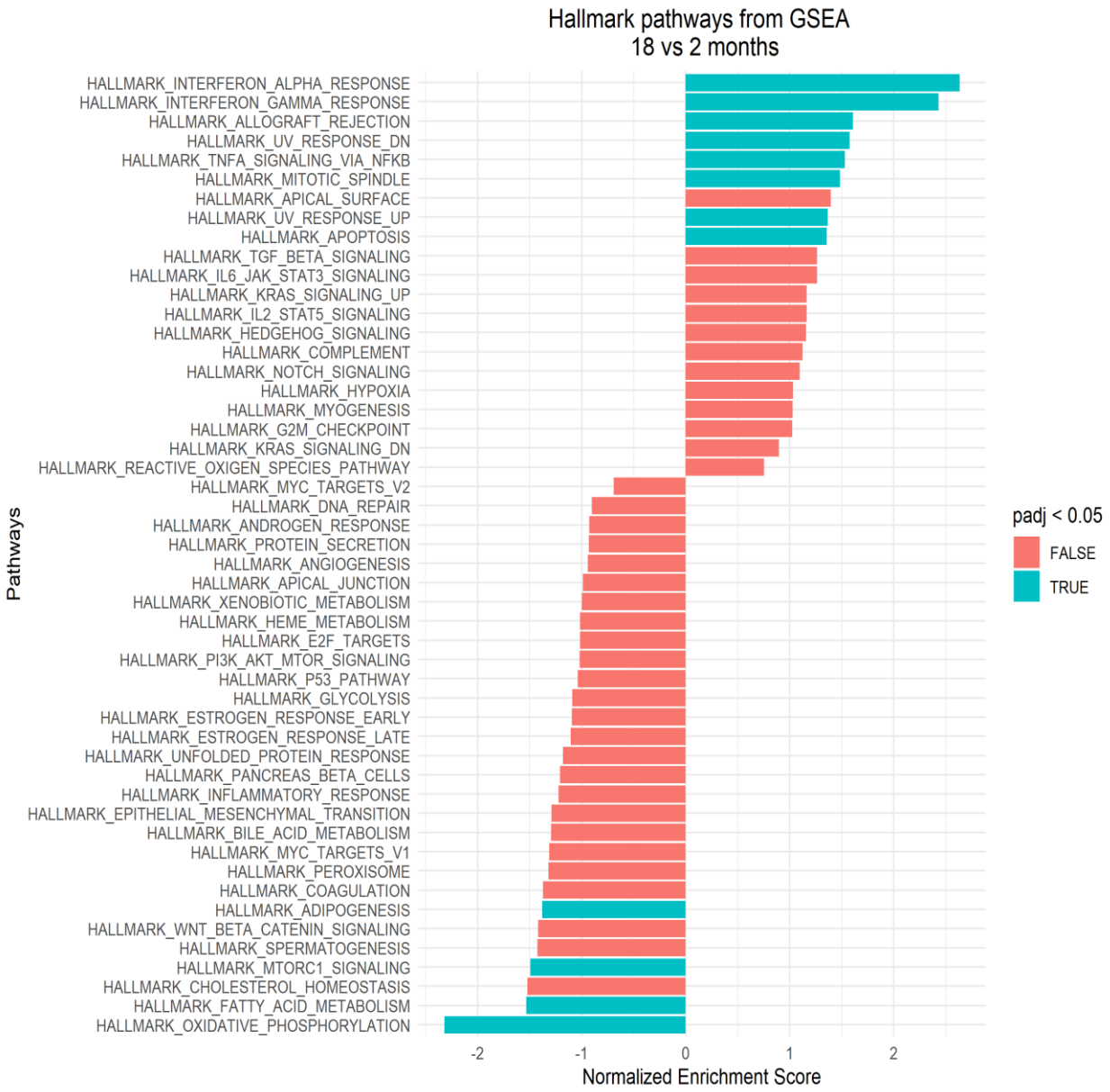

Figure 3.12 | Gene set enrichment analysis reveals significant dysregulation of several pathways in 18 months-old group. The gene set enrichment analysis, performed with FGSEA using hallmark gene sets, on the RNA-seq dataset comparing gene expression profiles of 18 months and 2 months-old groups reveal that a number of pathways associated with inflammatory response, such as response to interferon alpha, interferon gamma, allograft rejection and TNFα signaling via NF-κB are significantly upregulated. The pathways that are significantly downregulated in the ECs of 18 months-old mice include oxidative phosphorylation, fatty acid metabolism and MTORC1 signaling.

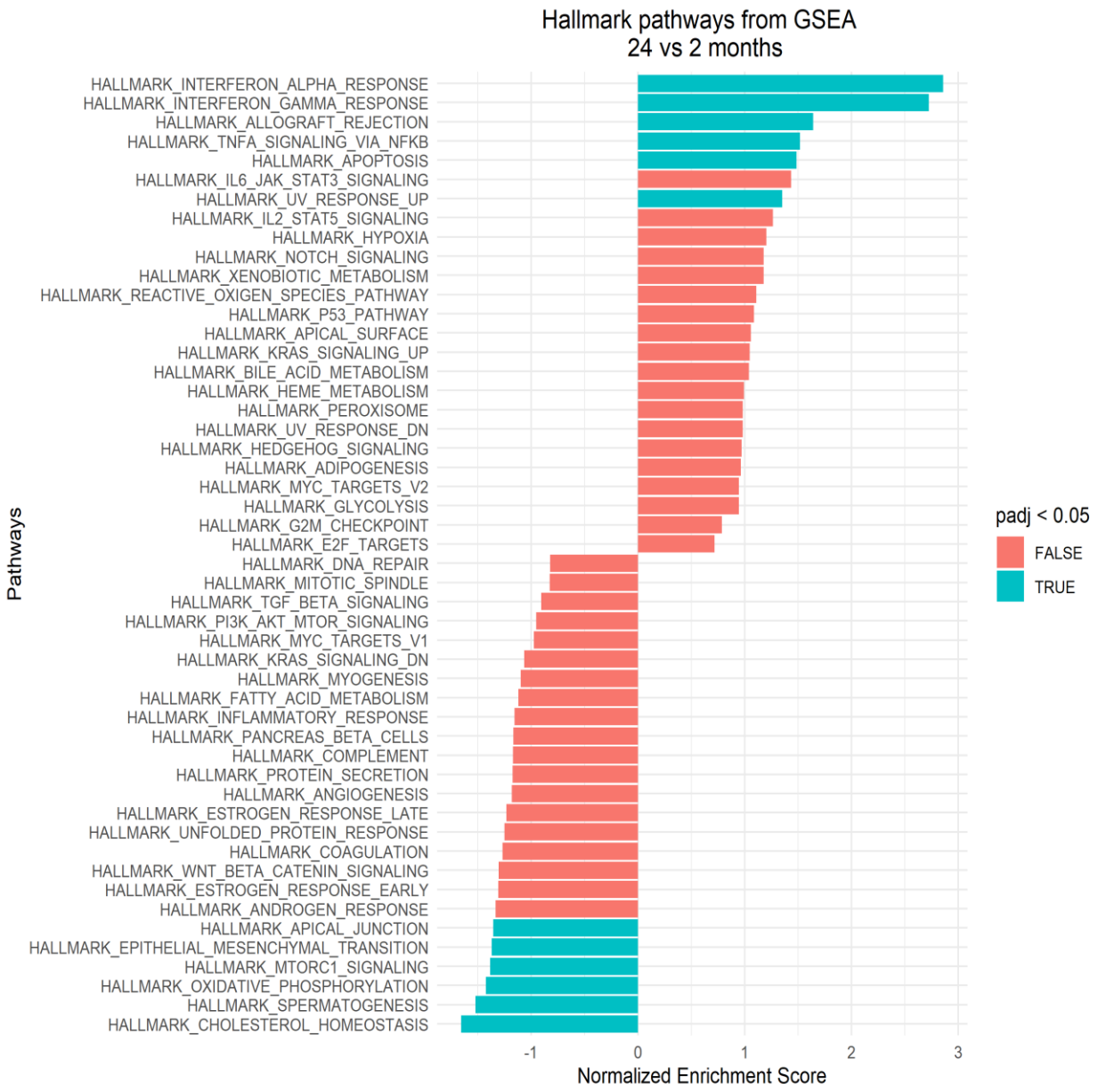

Figure 3.13 | Gene set enrichment analysis reveals significant dysregulation of several pathways in 24 months-old group. The gene set enrichment analysis, performed with FGSEA using hallmark gene sets, on the RNA-seq dataset comparing gene expression profiles of 18 months and 2 months-old groups reveal that a number of pathways associated with inflammatory response, such as response to interferon alpha, interferon gamma, allograft rejection and TNFα signaling via NF-κB are significantly upregulated. The pathways that are significantly downregulated in the ECs of 18 months-old mice include oxidative phosphorylation, fatty acid metabolism and MTORC1 signaling. Interestingly, gene set enrichment analysis indicate that the pathways dysregulated in 18 and 24 months-old mice are similar.

3.10 The expression of *Srf* in the cerebral ECs does not change with age.

Contrary to the starting hypothesis that, in mice, increased intracerebral bleeding with increasing age may be caused by age-dependent downregulation of *Srf/Mrtf* gene expression and associated down-regulation of SRF/MRTF target genes in brain ECs, the expression level of *Srf* transcripts in the murine cerebral ECs does not change with age. The log2-fold change in the expression level of *Srf* in 18 months-old male mice is – 0.15 (adjusted p-value = 0.80) and the log2-fold change in the expression level in 24 months-old male mice is – 0.08 (adjusted p-value = 0.94). There was no significant dysregulation of *Srf* transcripts found in the 6 and 12 months-old mice. Also, the expression levels of *Srf* remained unchanged with age in females, indicating no change in the expression level of *Srf* with age.

The expression level of *Mrtfa* transcripts in the murine cerebral ECs does not change with age. The log2-fold change in *Mrtfa* levels in 18 months-old mice is 0.02 (adjusted p-value = 0.98), while the log2-fold change in the expression levels in 24 months-old mice is –0.23 (adjusted p-value = 0.91). No change in the expression levels of *Mrtfa* was observed in the ECs isolated from 6 and 12 months-old mice as well. Similarly, the expression level of *Mrtfb* transcripts in the murine cerebral ECs does not change with age. The log2-fold change in *Mrtfb* levels in 18 months-old mice is 0.29 (adjusted p-value = 0.35), while the log2-fold change in the expression levels in 24 months-old mice is 0.27 (adjusted p-value = 0.49). Linear regression analysis performed on the RNA-seq dataset also indicated no age-dependent dysregulation of *Srf* and its cofactors *Mrtfa* and *Mrtfb* in cerebral ECs (Figure 3.14).

The list of ~ 1000 known SRF target genes identified in cultured NIH3T3 fibroblasts (Esnault et al., 2014) was used to identify the SRF target genes which were dysregulated with age in our RNA-seq dataset. The genes that were found to be significantly dysregulated with age (adjusted p-value < 0.05) in the linear regression analysis performed on all the samples, adjusted for sex, were considered. Out of 1388 genes that were significantly dysregulated with age, 88 genes (6.34 %) were SRF targets. Among them, 46 SRF target genes were found to be significantly downregulated, while 42 were significantly upregulated with age. Table 3.3 lists all the SRF target genes that were found to be significantly dysregulated with age.

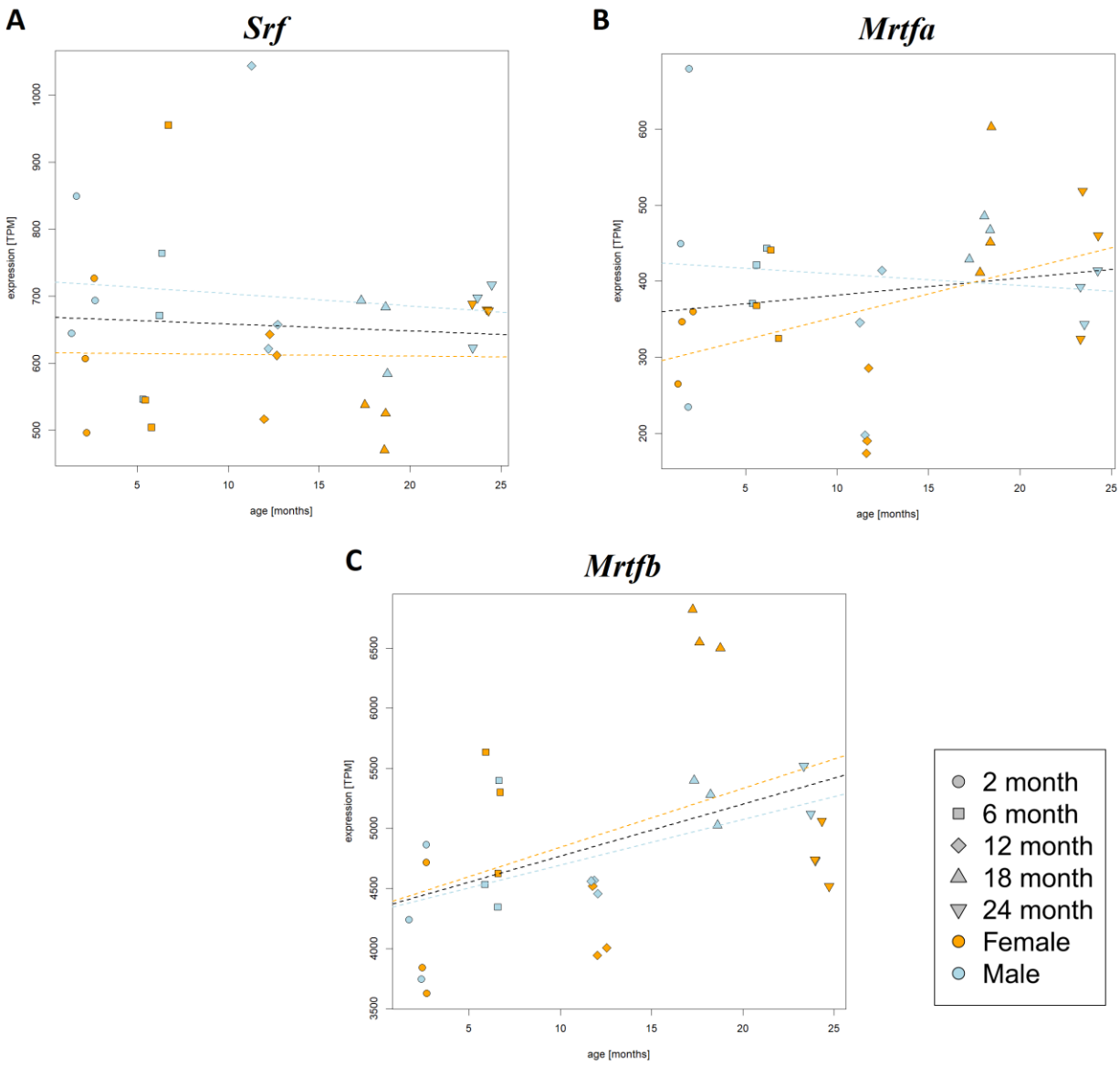

Figure 3.14 | The expression level of *Srf*, *Mrtfa* and *Mrtfb* with age. Linear regression analysis of RNA-seq dataset suggests that the expression of **(A)** *Srf* (adjusted p-value = 0.88), **(B)** *Mrtfa* (adjusted p-value = 0.69) and **(C)** *Mrtfb* (adjusted p-value = 0.15) does not change significantly with age. The linear regression analysis performed on the RNA-seq dataset includes the males and females but corrects for the effects of sex by taking the differences in expression between males and females as covariates. The linear regression analysis was performed on the TPM (transcripts per million) values calculated for all the transcripts in each sample (Calculation of TPM values discussed in Section 2.2.14).

Next, the common genes that were significantly dysregulated (adjusted p-value < 0.05) in both the 18 months-old males and the linear regression analysis were considered. Among the 428 genes that were found to be commonly dysregulated in 18 months-old males and the linear regression analysis performed on all the samples, 32 genes (7.47 %) were SRF targets. Among the 32 SRF target genes that were found to be significantly dysregulated, 10 genes were downregulated while 22 were upregulated (Table 3.4).

The list of 197 SRF and MRTF target genes which are directly implicated in regulating the cellular cytoskeleton (Esnault et al., 2014) was used to identify the SRF and MRTF target genes involved in cytoskeletal dynamics significantly dysregulated with age in cerebral ECs. Linear regression analysis indicated 16 genes (8.12 %) to be significantly dysregulated with age (adjusted p-value < 0.05) in the cerebral ECs. While 10 genes were significantly downregulated, 6 were significantly upregulated (Table 3.5). However, upon considering the common SRF target cytoskeleton genes that were significantly dysregulated (adjusted p-value < 0.05) in both the 18 months-old males and the linear regression analysis, 3 genes (*Fyn*, *Tubb6* and *Dcaf12*) were found to be downregulated and 2 genes (*Trio* and *Myh9*) were upregulated.

Table 3.3 SRF target genes significantly dysregulated with age (Linear regression analysis)

Downregulated genes (46)	*Lims1, Tpst2, Htra1, Cnn3, Bag2, Pank1, Fyn, Leprotl1, Rhoj, Pdia6, Fermt2, Chek2, Tubb6, Kctd5, M6pr, Tm2d2, Tubb5, Tmem33, Xpnpep1, Sirt2, Dcaf12, Sh3gl1, Capzb, Slbp, Klf9, Nasp, Grn, Rell1, Ccdc85b, Tmem98, Gspt1, Slc31a1, Mrps7, Dapk3, Bcl10, Tpm1, Trerf1, Ddah2, Phc2, Map1lc3b, Cpne2, Mtmr14, Gnb1, Arf2, Cpt2, Rgl1*
Upregulated genes (42)	*Zbtb20, Actg1, Fosl2, Ubr4, Trio, Mreg, Smg1, Iqgap1, Myo9a, Maml2, Zfc3h1, Cdc42bpa, Nbeal1, Rab11fip2, Med13l, Palld, Ell2, Ppp2r3a, Zmat1, Erc1, Nfkbiz, Junb, Tnrc6b, Spen, Aff1, Ppp3cb, Ep400, Sfi1, Ahnak, Ptgs2, Zswim6, Tmem117, Chd4, Birc6, Efemp2, Lpp, Myh9, Rev3l, Cdk14, Crim1, Stx11, Pla2g4a*

Table 3.4 SRF target genes that were found to be significantly dysregulated, common to 18 months-old males (vs. 2 months males) and the linear regression analysis.

Downregulated genes (10)	*Htra1, Bag2, Pank1, Fyn, Leprotl1, Chek2, Tubb6, Tm2d2, Dcaf12, Grn*
Upregulated genes (22)	*Trio, Smg1, Myo9a, Zfc3h1, Nbeal1, Med13l, Erc1, Junb, Tnrc6b, Spen, Aff1, Ahnak, Ptgs2, Birc6, Efemp2, Lpp, Myh9, Rev3l, Cdk14, Crim1, Stx11, Pla2g4a*

Table 3.5 SRF and MRTF target genes involved in regulating cellular cytoskeleton that were found to be significantly dysregulated with age (Linear regression analysis)

Downregulated genes (10)	*Lims1, Cnn3, Fyn, Fermt2, Tubb6, Tubb5, Sirt2, Dcaf12, Capzb, Tpm1*
Upregulated genes (6)	*Actg1, Ubr4, Trio, Palld, Sfi1, Myh9*

3.11 *Cldn5* gene is downregulated in the cerebral ECs of 18 months-old mice.

The expression of *Cldn5* gene is significantly downregulated with age. Claudin-5 is the major claudin expressed in the CNS ECs and forms the primary structural component of the endothelial TJ complex. The log2-fold change in the expression level of *Cldn5* in 18 months-old males is – 0.57 (adjusted p-value = 0.03), indicating approximately 1.5-fold reduction in the expression of *Cldn5* gene. However, no significant downregulation in the expression of Cldn5 gene was observed in the 24 months-old group (log2-fold change = – 0.34, adjusted p-value = 0.44). The linear regression analysis suggests an age-dependent downregulation of Cldn5 gene (adjusted p-value = 0.009) with a correlation coefficient (r-squared value) of 0.42, meaning that 42% of the variance in the expression level of Cldn5 gene can be attributed to age (Figure 3.15).

No significant change was observed in the expression of other isoforms of claudins *Cldn1*, *Cldn2*, *Cldn3*, *Cldn10*, *Cldn11* and *Cldn12* in 18 months-old males (adjusted p-values > 0.1). Also, the expression level of the *Ocln* (occluding) gene did not exhibit any age-dependent change. The linear regression analysis also didn't indicate any change in the expression levels of the aforementioned claudin isoforms and occludin, which constitute the key components of the tight junctions at BBB (Figure 3.15).

Among the junctional adhesion molecules, *F11r* gene encoding the JAM-A protein was found to be significantly downregulated (adjusted p-value = 0.0008) in the linear regression analysis. The correlation coefficient (r-squared value) for *F11r* gene is 0.59 which suggests that 59% of the variance in the expression level of *F11r* can be explained by age. No significant age-dependent dysregulation was observed in other important junctional adhesion molecules implicated at the BBB such as *Jam2*, *Jam3* and *Igsf5* (adjusted p-values > 0.1).

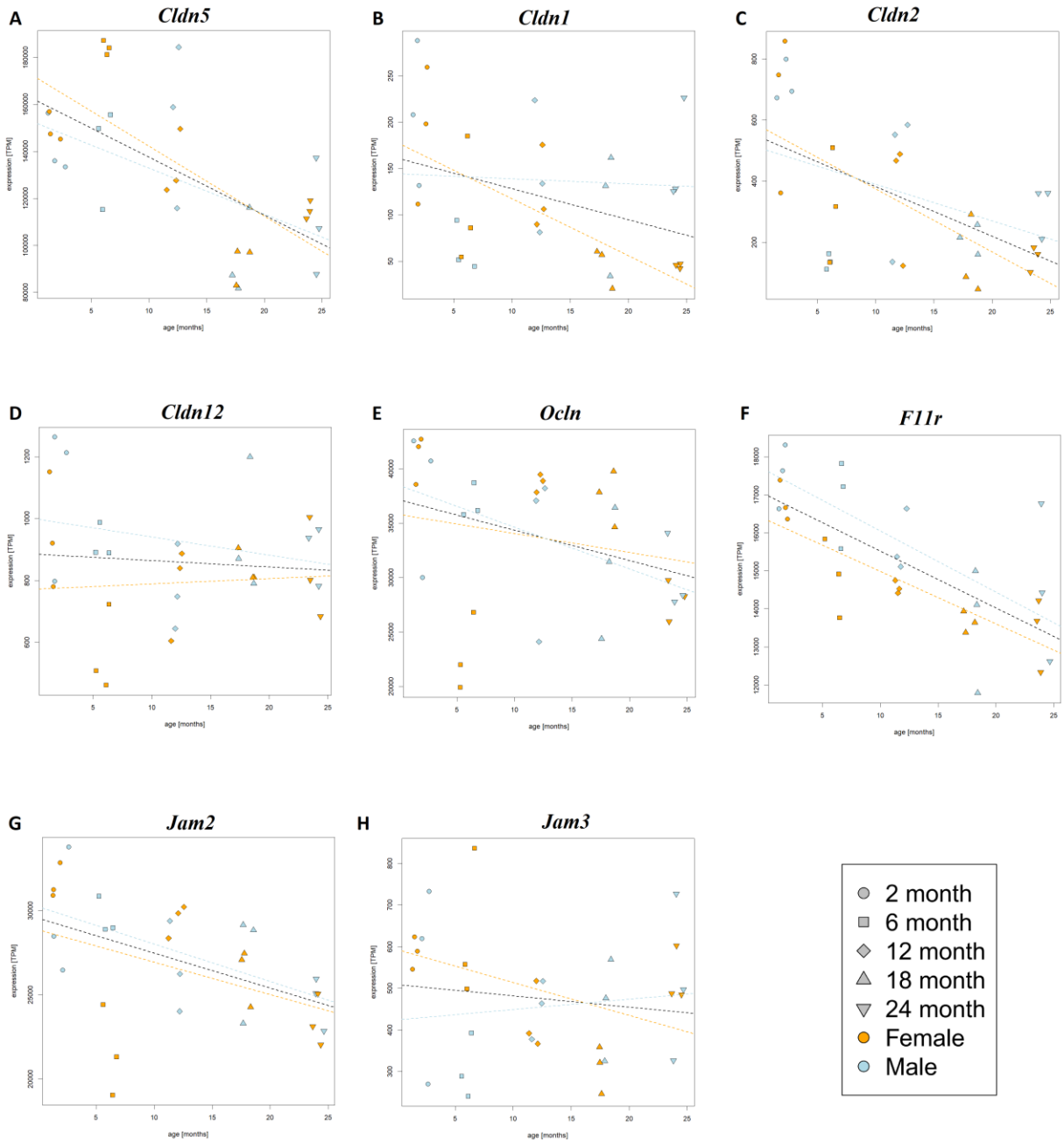

Figure 3.15 | Expression of genes encoding key components of tight junctions across age. The linear regression analysis indicates that among major tight junction proteins at the BBB, *Cldn5* and *F11r* show an age-dependent downregulation, with correlation coefficients of 0.42 (adjusted p-value = 0.009) and 0.59 (adjusted p-value = 0.0008), respectively . However, no age-dependent downregulation of other tight junction components such as *Cldn1*, *Cldn2*, *Cldn12*, *Ocln*, *Jam2* and *Jam3* was observed (adjusted p-values > 0.1). TPM : Transcripts per million.

3.12 The expression of VE-Cadherin (*Cdh5*) does not change with age.

The gene encoding VE-Cadherin – the primary component of the adherens junction at BBB – was not dysregulated in 18 and 24 months-old males. The log2-fold change in the expression levels of *Cdh5* gene was 0.08 (adjusted p-value = 0.93) in the 18 months- old males and – 0.04 (adjusted p-value = 0.98) in the 24 months-old mice. Linear regression analysis (Figure 3.16 A) indicated no age-dependent dysregulation of *Cdh5* over age, with a correlation coefficient (r-squared value) of 0.17 (adjusted p-value = 0.71).

3.13 N-Cadherin (*Cdh2*) is significantly downregulated with age.

Among the other isoforms of cadherins expressed at the BBB, N-Cadherin was significantly downregulated in both 18 and 24 months-old males The log2-fold change in 18 months-old males was – 1.1 (adjusted p-value = 0.0009) and – 1.24 in 24 months-old males (adjusted p-value = 0.0005), indicating an approximately 2.2-fold downregulation of *Cdh2*. The expression of *Cdh2* gene in the cerebral ECs is significantly downregulated with age, as revealed by linear regression analysis (Figure 3.16 B), with a correlation coefficient (r-squared value) of 0.45 and adjusted p-value of 0.006. However, no significant change in the expression of *Cdh1*, β-Catenin (*Ctnnb1*), α-Catenin (*Ctnna1*), p120 (*Ctnnd1*) and plakoglobin (*Jup*) was detected (Figure 3.16 C-G) in 18 months and 24 months-old group (adjusted p-value > 0.1).

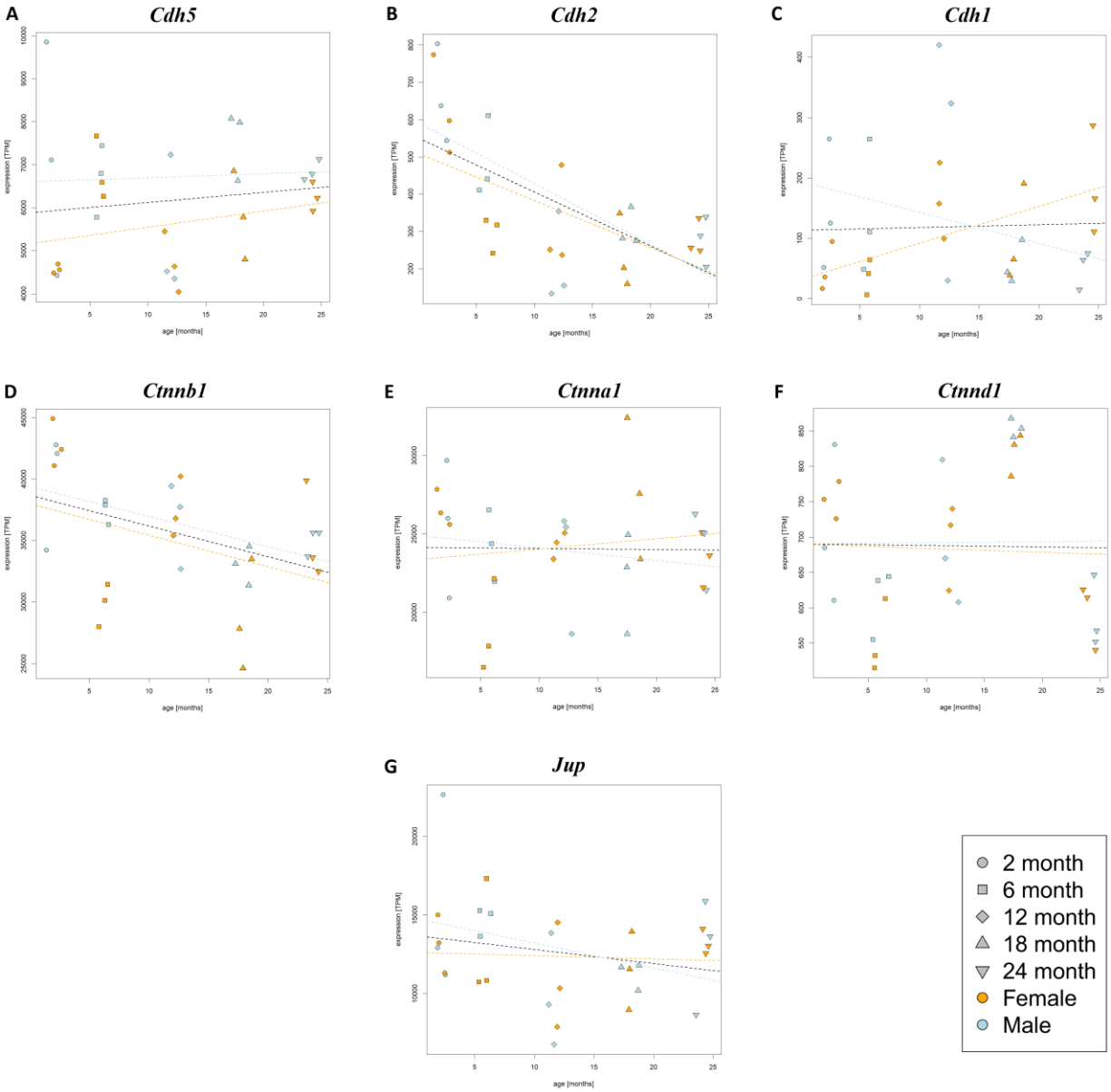

Figure 3.16 | Expression of genes encoding key components of adherens junction across age. The *Cdh5* gene, which encodes VE-Cadherin, was not dysregulated with age. Also, other major components of the adherens junction such as Cdh1, Ctnnb1, Ctnna1, Ctnnd1 and Jup were not dysregulated with age (adjusted p-values > 0.1). However, the expression of Cdh2 gene encoding for neuronal cadherin showed a significant age-dependent downregulation, with correlation coefficient of 0.45 (adjusted p-value = 0.006). TPM : Transcripts per million.

3.14 The expression of genes encoding actin-binding proteins and cytoplasmic plaque proteins at the BBB does not change with age.

No change in the expression of genes encoding various actin-binding proteins was observed in the 18 and 24 months-old males. The expression of *Cdc42*, *RhoA*, *Rac1*, *Vcl*, *Vasp*, *Anln* and *Actn4* was found to be unchanged in both 18 and 24 months-old males (adjusted p-value > 0.1). Linear regression analysis suggests no age-dependent change in the expression of aforementioned genes (adjusted p-value > 0.1).

Among various cytoplasmic plaque proteins present at the BBB and implicated in the maintenance of vascular integrity, the zonula occludens proteins are the key cytoplasmic components of the tight junction complex. The expression of *Tjp1*, *Tjp2*, *Tjp3*, *Cgn* and *Afdn* was not dysregulated in 18 and 24 months-old males (adjusted p-value > 0.1). Linear regression analysis also suggested no age-dependent change in the expression levels of the genes encoding zonula occludens proteins (adjusted p-values > 0.1).

The major scaffolding proteins present at the BBB include *Magi3*, *Magi1*, *Patj*, *Mpp1*, *Mpp5*, *Mpp7*, *Dlg1*, *Mpdz*, *Pard3*, *Pard6a* and *Pard6b*. No change in the expression level of these genes was observed in the 18 and 24 months-old males (adjusted p-values > 0.1). Also, linear regression analysis performed on the RNA-seq dataset doesn't suggest any age-dependent dysregulation of the aforementioned genes encoding major scaffolding proteins (adjusted p-values > 0.1).

3.15 The expression of basal membrane components does not change with age.

Collagen IV is the most important component of the basal membrane at the BBB, with α1 and α2 being the major subunits that together form a heterotrimer. No significant dysregulation of *Col4a1* and *Col4a2* was observed in 18 and 24-months old males. The log2-fold change of *Col4a1* in 18 months-old males was – 0.43 (adjusted p-value = 0.50) and – 0.64 in 24 months-old males (adjusted p-value = 0.22). The log2-fold change of *Col4a2* was – 0.54 (adjusted p-value = 0.22) in 18 months-old and – 0.58 (adjusted p-value = 0.12) in 24 months-old males. Although both *Col4a1* and *Col4a2* show a downregulation of approximately 1.5-times, but the results are not statistically significant. Linear regression analysis suggests that there is no age-dependent change in the expression of Col4a1 (adjusted p-value = 0.53) and Col4a2 (adjusted p-value = 0.44) (Figure 3.17).

Among the laminins, *Lama2*, *Lama5*, *Lamb1* and *Lamc1* are the major laminins present at the extracellular matrix at the BBB. While no significant changes in the expression levels of *Lama2*, *Lama5* and *Lamc1* were observed in the 18 and 24 months-old males (adjusted p values > 0.1), *Lamb1* was significantly downregulated in both 18 and 24 months-old males. The log2-fold change of *Lamb1* was – 1.13 (adjusted p-value = 0.02) in 18 months-old males and –1.17 (adjusted p-value = 0.03) in 24 months-old males. However, no significant age-dependent change in the expression of Lamb1 was observed in the linear regression analysis (Figure 3.17).

There was no significant change in the expression of Nidogen1 (*Nid1*) and Nidogen2 (*Nid2*) in 18 and 24 months-old males. The log2-fold change of *Nid1* was – 0.67 (adjusted p-value = 0.07) in 18 months-old males and –0.76 (adjusted p-value = 0.06) in 24 months-old males. Although there is 1.6-fold downregulation in the expression of *Nid1* in 18 and 24 months-old males, the adjusted p-value is slightly higher than the widely accepted value of 0.05. No significant changes in the expression of *Nid2* were observed in 18 months-old males (log2-fold change = – 0.05, adjusted p-values = 0.96) and 24 months-old males (log2-fold change = – 0.18, adjusted p-value = 0.89).

Integrins αvβ3, α5β1, α6β1, α1β1 and α6β4 are major integrins present at the BBB and have been primarily implicated in angiogenesis. Among integrins, Integrinαv (*Itgav*) was significantly downregulated in the 24 months-old males (log2-fold change = –1.13, adjusted

p-value = 0.03), but was not significantly downregulated in 18 months-old males (log2-fold change = – 0.50, adjusted p-value = 0.52).

Linear regression analysis indicates no age-dependent dysregulation of *Itgav* (adjusted p-value = 0.63). *Itga4* was significantly downregulated in both 18 and 24 months-old males. The log2-fold change of *Itga4* was –2 (adjusted p-value < 0.001) in 18 months-old males and the log2-fold change of *Itga4* in 24 months-old males was –1.94 (adjusted p-value < 0.001), indicating close to 4-fold downregulation in both the older cohorts. Linear regression analysis showed age-dependent downregulation of *Itga4* with a correlation coefficient of 0.44 (adjusted p-value = 0.007). No significant change in the expression of, *Itga5*, *Itgb1* and *Itgb6* were observed in 18 or 24 months-old males (adjusted p-value > 0.1). Linear regression analysis also indicated no age-dependent change in the expression levels of *Itga5*, *Itgb1* and *Itgb6* (adjusted p-value > 0.1).

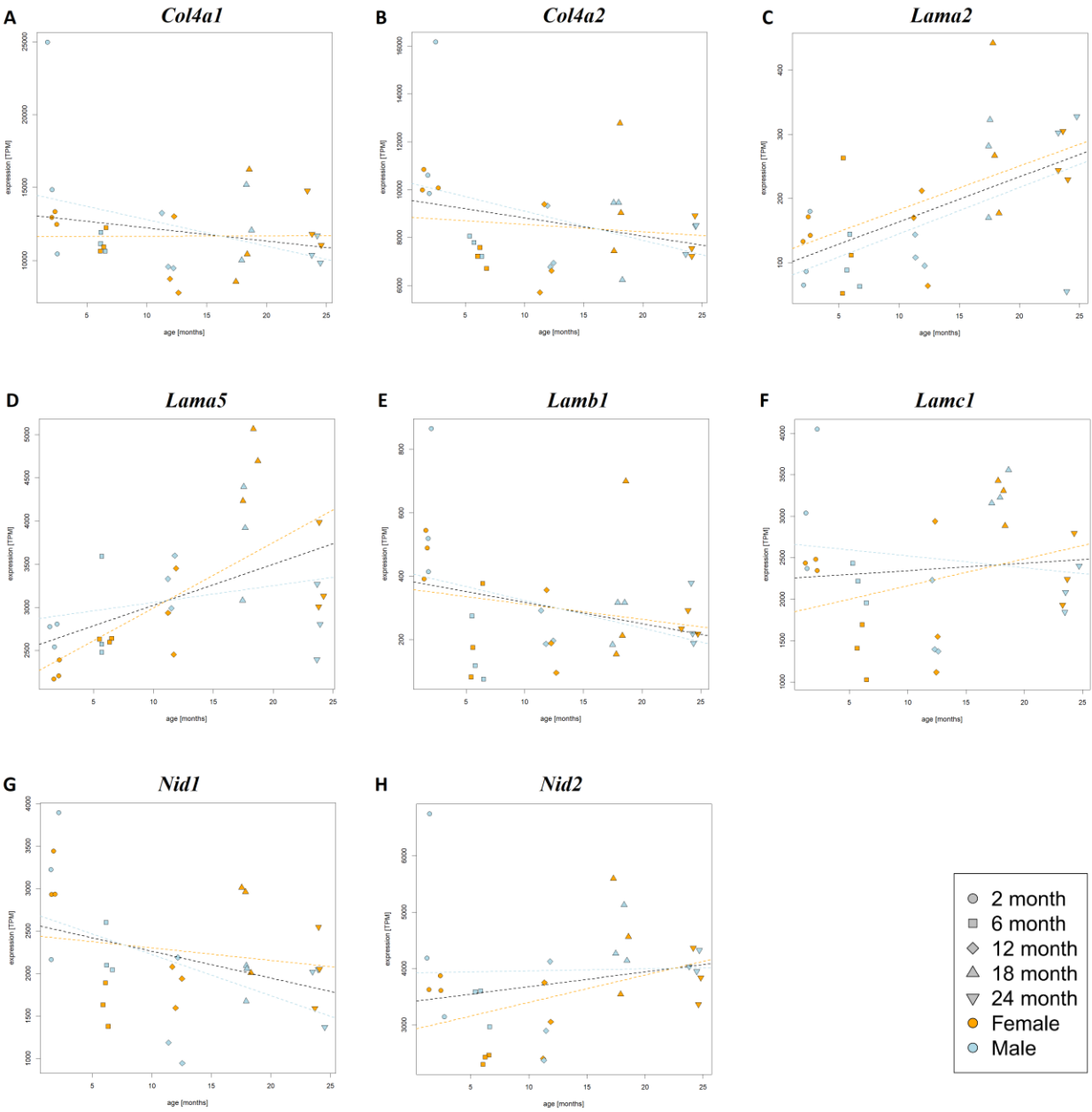

Figure 3.17 | Expression of genes encoding key components of basement membrane across age. The expression levels of transcripts of several major components of basement membrane and extracellular matrix proteins implicated in the maintenance of the BBB were found to be unchanged with age. *Col4a1*, *Col4a2*, *Lama2*, *Lama5*, *Lamb1*, *Lamc1*, *Nid1* and *Nid2* do not exhibit any significant age-dependent dysregulation in the linear regression analysis of the RNA-seq dataset (adjusted p-values > 0.1). TPM : Transcripts per million.

3.16 The expression of *Aplnr* decreases progressively with age.

The expression of *Aplnr* encoding the Apelin receptor, known to play a crucial role in positive regulation of vasodilation, was highly downregulated in the cerebral ECs with age. *Aplnr* showed a progressive decrease in expression with age. The log2-fold change values of *Aplnr* were – 3.18, – 4.10, – 4.51 and – 5.24 (adjusted p-values < 0.001) in 6, 12, 18 and 24 months-old male mice, respectively – as compared to 2 months-old mice. The expression of *Aplnr* also exhibited progressive downregulation with age in the females. The log2-fold change values of *Aplnr* in the females of 6, 12, 18 and 24 months were – 3.30, – 3.47, – 4.54 and – 4.98 (adjusted p-values < 0.001), respectively. Linear regression analysis on the RNA-seq dataset also confirmed the age-dependent downregulation of *Aplnr*, with a correlation coefficient of 0.47 (adjusted p-value = 0.004) (Figure 3.18).

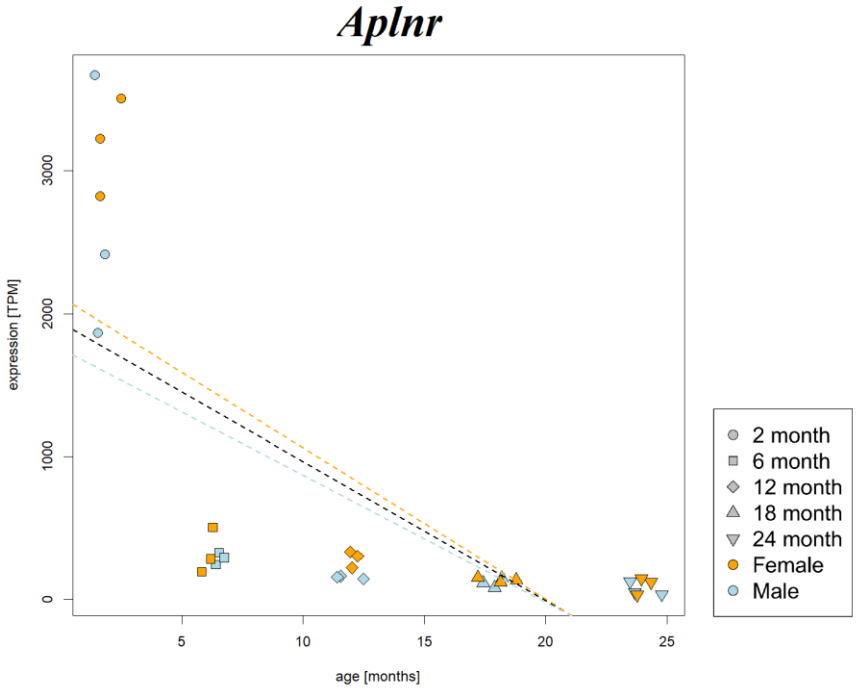

Figure 3.18 | The expression level of *Aplnr* with age. Linear regression analysis suggests that the expression of *Aplnr* decreases with age, with a correlation coefficient (r-squared value) of 0.47 (adjusted p-value = 0.004). The plot showing the normalized counts of *Aplnr* in each sample indicates the downregulation of *Aplnr* is the sharpest between the ages of 2 months and 6 months. TPM : Transcripts per million.

3.17 *Htra1* expression in cerebral ECs decreases with age.

The expression of *Htra1* gene was observed to be significantly downregulated in the 18 and 24 months-old males. The log2-fold change of *Htra1* in 18 months-old males was – 1.5 (adjusted p-value < 0.001) and – 1.31 in 24 months-old males (adjusted p-value < 0.001), indicating approximately 3-fold downregulation in the expression of *Htra1* in the cerebral ECs of old male mice. Linear regression analysis also corroborated an age-dependent downregulation of Htra1 in the cerebral ECs, with a correlation coefficient of 0.62 (adjusted p-value < 0.001) (Figure 3.19). In human patients, a loss of function mutation in the *HTRA1* gene leads to the development of CARASIL, where patients display stroke-like symptoms. *HTRA1* gene encodes a serine protease that regulates the TGF-β signaling necessary for the maintenance of vascular integrity in the brain.

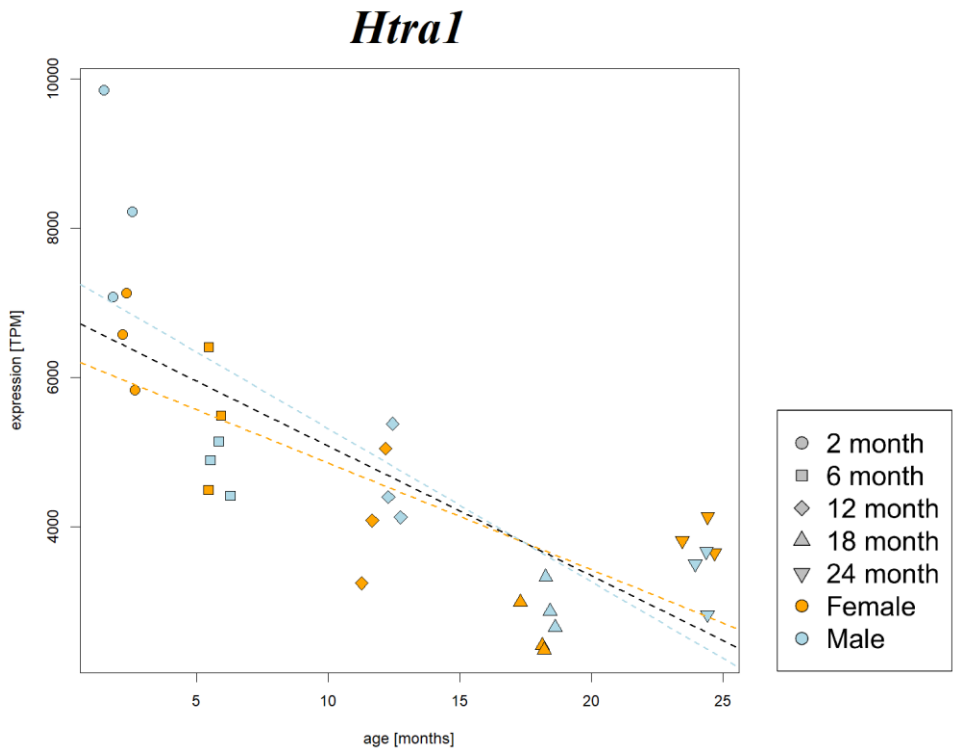

Figure 3.19 | The expression level of *Htra1* with age. Linear regression analysis suggests that the expression of *Htra1* decreases with age, with a correlation coefficient (r-squared value) of 0.62 (adjusted p-value = 0.0001). TPM : Transcripts per million.

3.18 *Mfsd2a*, critical for the formation and maintenance of BBB, is downregulated with age.

The major facilitator super family domain containing 2a protein, encoded by the *Mfsd2a* gene is critical for the formation and maintenance of BBB, and *Mfsd2a*$^{-/-}$ mice exhibit a leaky BBB[189]. The linear regression analysis of the RNA-seq data suggests that *Mfsd2a* is progressively downregulated with age (Figure 3.20) with a correlation coefficient of 0.62 (adjusted p-value = 0.0001), meaning that 62% of the variance in the expression of *Mfsd2a* can be attributed to age. The 24 months-old males showed a significant, 1.5-fold downregulation of *Mfsd2a* expression, (log2-fold change = – 0.58, adjusted p-value = 0.02).

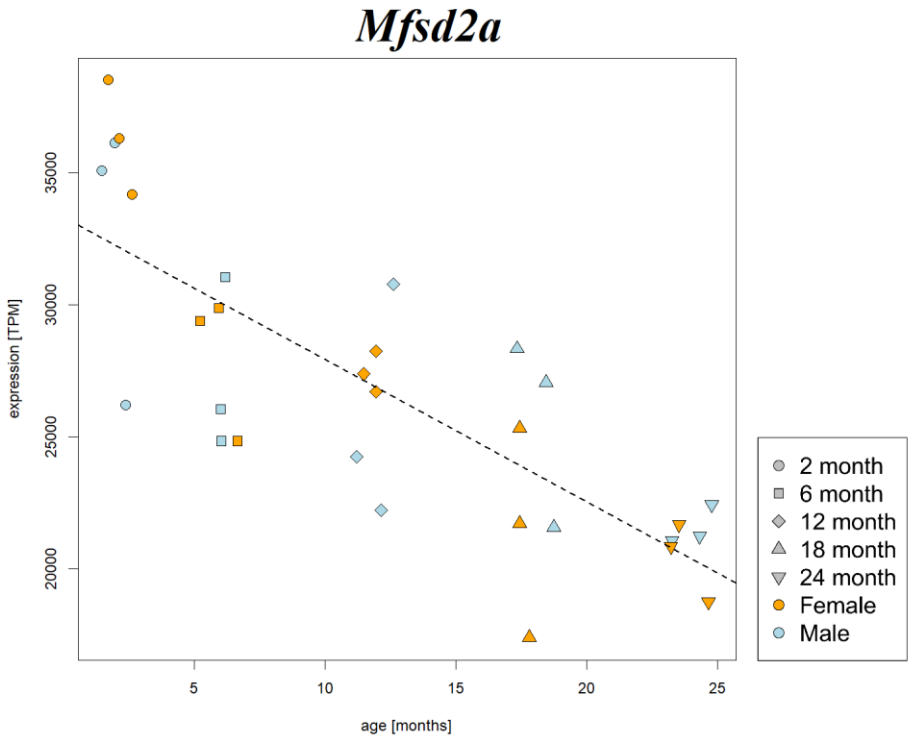

Figure 3.20 | The expression level of *Mfsd2a* with age. Linear regression analysis suggests that the expression of *Mfsd2a* decreases with age, with a correlation coefficient (r-squared value) of 0.62 (adjusted p-value = 0.0001). The 24 months-old males showed a significant, 1.5-fold downregulation of *Mfsd2a* expression, (log2-fold change = -0.58, adjusted p-value = 0.02). TPM : Transcripts per million.

3.19 Reduced representation bisulfite sequencing shows increased CpG methylation level in cerebral ECs from 18 months-old mice.

(*The RRBS study was performed in collaboration with the group of Prof. Dr. Jörn Walter at the University of Saarland, Saarbrücken. The RRBS libraries were prepared by myself. Sequencing and data analysis were performed by Dr. Gilles Gasparoni, Saarbrücken*).

CpG islands are CG-rich regions that are associated with promoters in mammalian genome. As the methylation of CpG islands remarkably influences the expression of genes, reduced representation bisulfite sequencing (RRBS) was used to study the change in CpG methylation with age in the endothelial cells (ECs).

RRBS libraries were prepared from ECs isolated from mice aged 2, 6, 12 and 18 months. Mice aged 2 months (4 males, 6 females), 6 months (2 males, 2 females), 12 months (5 males, 3 females) and 18 months (3 males, 4 females) were considered for data analysis. In the 6 months-age group, one male and one female were excluded from sequencing due to poor library quality.

1000 bp continuous, non-overlapping tiles were considered for the determination of differentially methylated regions (DMRs) using Methylkit[182]. Differentially methylated sites were investigated in the 1000 bp tiles having at least 2 CpGs and a minimum average coverage of 5 across all the samples. CpGs were investigated in total of 163,977 tiles having a length of 1000 bp and linear regression analysis was performed for differential methylation across age in those tiles. The principal component analysis of the samples after the determination of DMRs with Methylkit did not indicate sex-specific differences between the samples. No clear difference between the profiles of males and females were observed in the PCA plot comparing the principal components 1 (PC1) and 2 (PC2), that account for the highest and second highest variance in the data, respectively. Similarly, no clear difference between males and females was observed in the PCA plots comparing principal components 2 and 3, and principal components 3 and 4 (Figure 3.21). Since no difference was observed in the PCA, the males and females of each age group were pooled, and analysis was performed to study the change in methylation with age. Figure 3.22 shows average CpG methylation (in percentage) across all the samples considered for RRBS analysis.

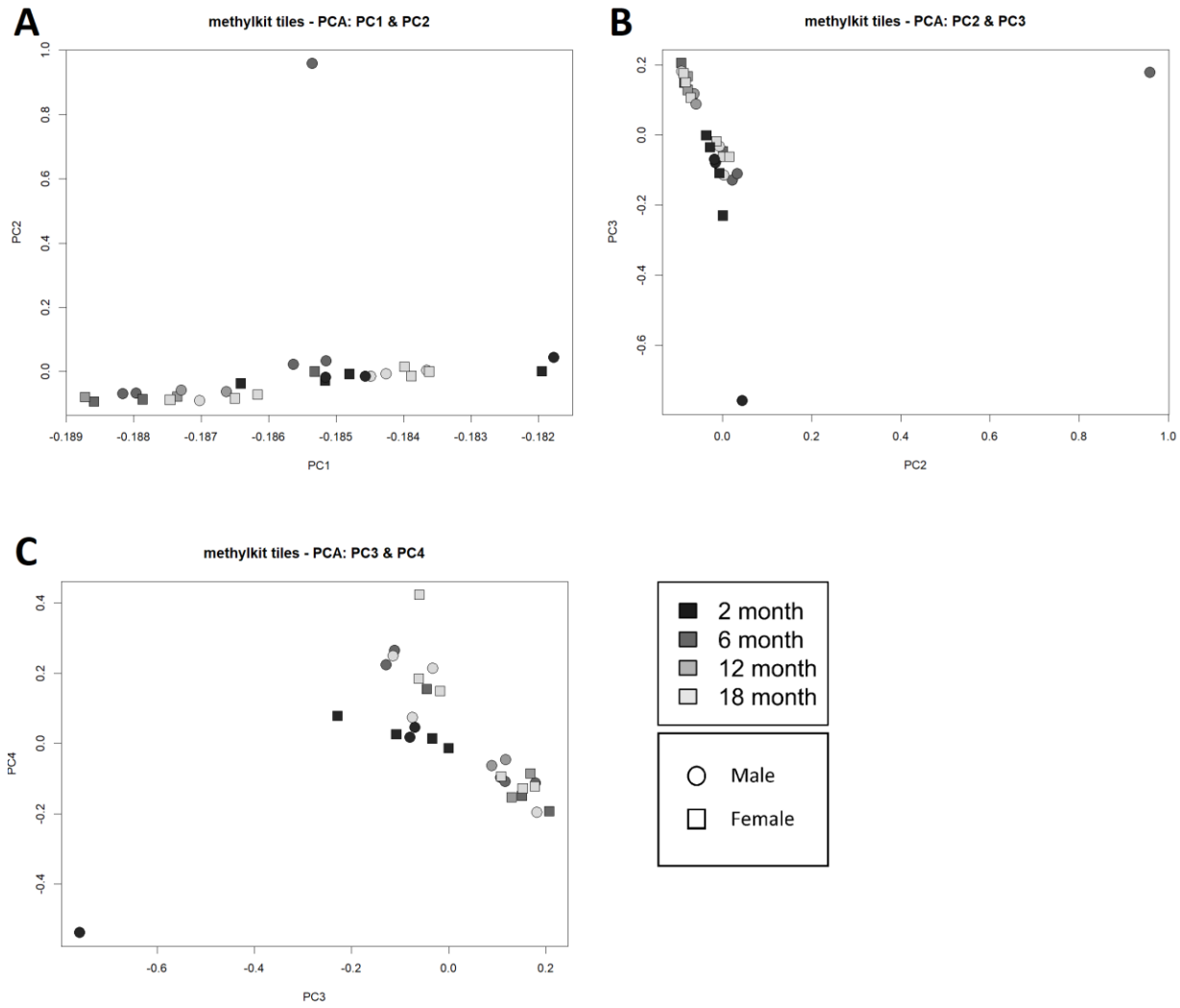

Figure 3.21 | Principal component analysis of samples (RRBS study) after determination of methylation using Methylkit. **(A)** The Principal Component Analysis (PCA) plots showing the principal components 1 and 2 (PC1 and PC2), **(B)** principal components 2 and 3 (PC2 and PC3), and **(C)** principal components 3 and 4 (PC3 and PC4) do not indicate any clear separation between the males and females, suggesting no sex-specific differences in methylation levels. PC1, PC2, PC3 and PC4 account for the largest, second largest, third largest and fourth largest variance in the data, respectively. The RRBS data analysis was performed by Dr. Gilles Gasparoni (University of Saarland, Saarbrücken).

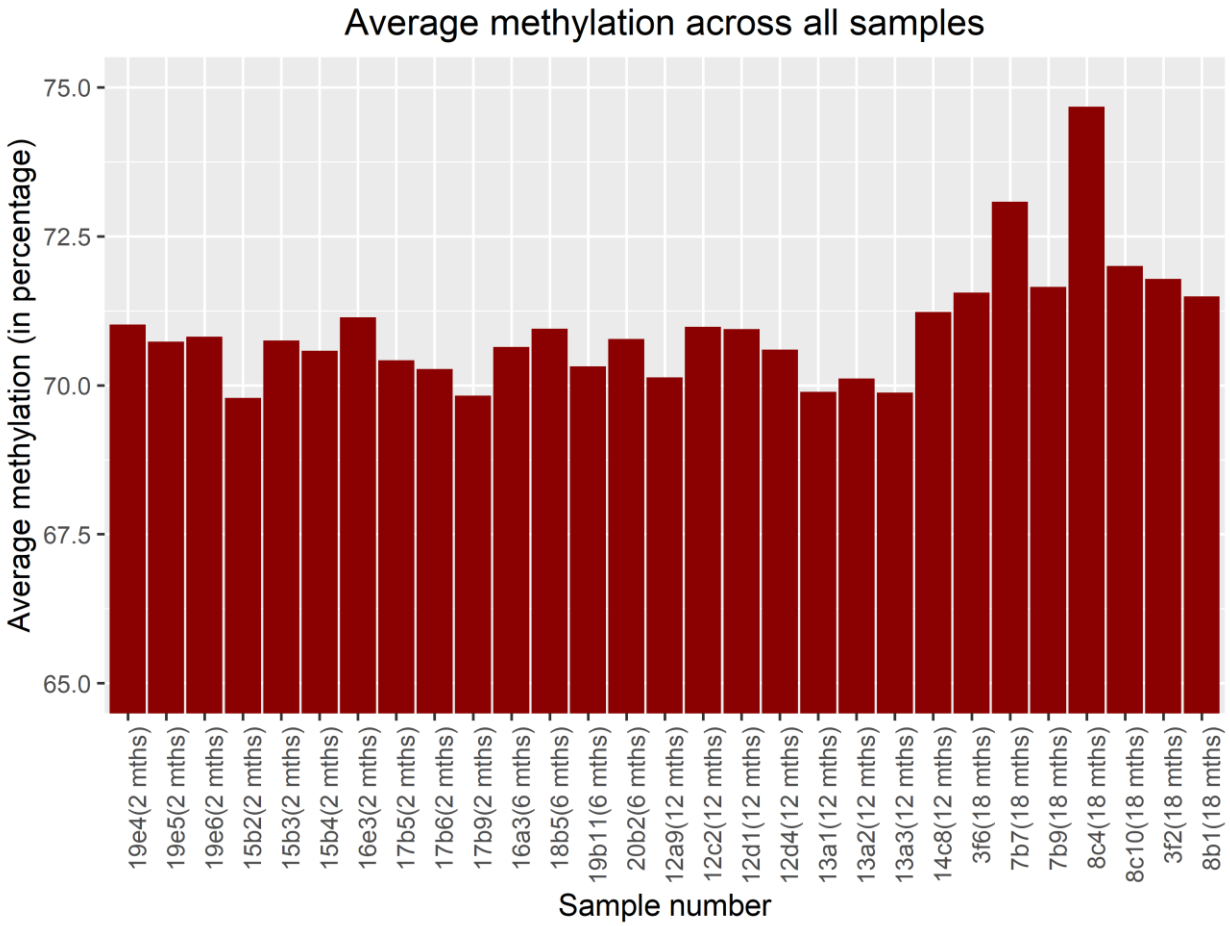

Figure 3.22 | Average methylation across all the samples. The bar plot shows average methylation (in percentage) across all the samples considered for RRBS analysis. The x-axis indicates the name of the mouse and its age in parentheses.

In 163,977 continuous, non-overlapping tiles having a length of 1000 bp, the average methylation level across all the CpGs investigated by RRBS was 70.52 % ± 0.46 (sd) in the 2 months-old mice, 70.66% ± 0.27(sd) in 6 months-old, 70.46% ± 0.53(sd) in 12 months-old and 72.30% ± 1.17(sd) in 18 months-old mice (Figure 3.23). One-way analysis of variance (ANOVA), followed by Tukey's HSD test were performed to compare all the possible pairs and test the statistical significance. Mice belonging to the oldest age-group (18 months) showed a significant increase in average methylation level in comparison to the 2,6 and 12 months-old mice, with an adjusted p-value less than 0.01 in each of the cases. However, no significant change in the level of methylation was observed between 2 months and 6 months (adjusted p-value = 0.987), 6 months and 12 months (adjusted p-value = 0.965), and 2 months and 12 months (adjusted p-value = 0.997) (Figure 3.24).

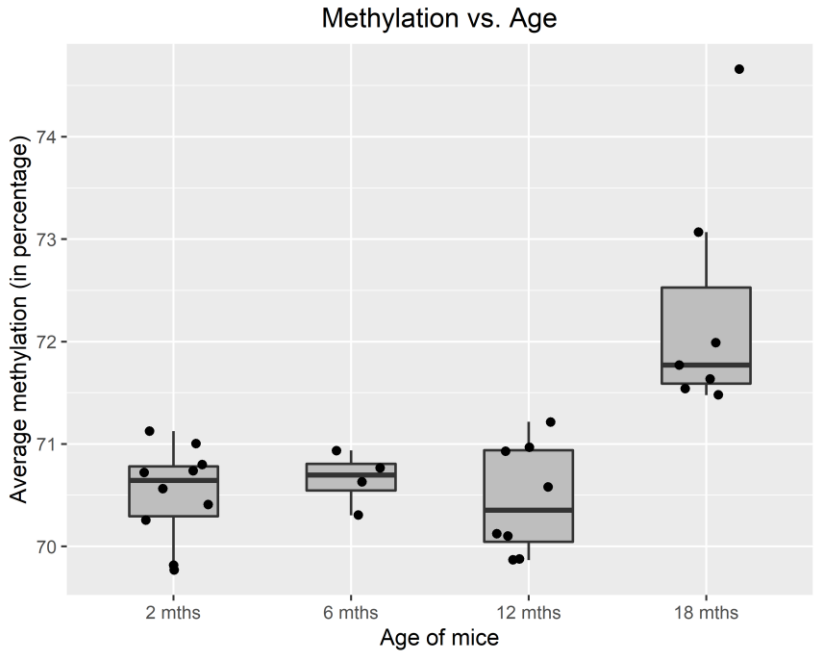

Figure 3.23 | Boxplot showing average CpG methylation percentage (RRBS study) in the samples of different age-groups. Each dot represents a sample. The lower and upper hinges in the box correspond to the first and third quartiles (25th and 75th percentiles, respectively), the horizontal bar in the box denotes median and the whiskers denote 1.5 x IQR (interquartile range is the difference between the third and first quartile). The average methylation level in 18 months-old group is significantly higher than the younger groups (adjusted p-value = 0.0001. Determined by ANOVA, followed by Tukey's HSD test).

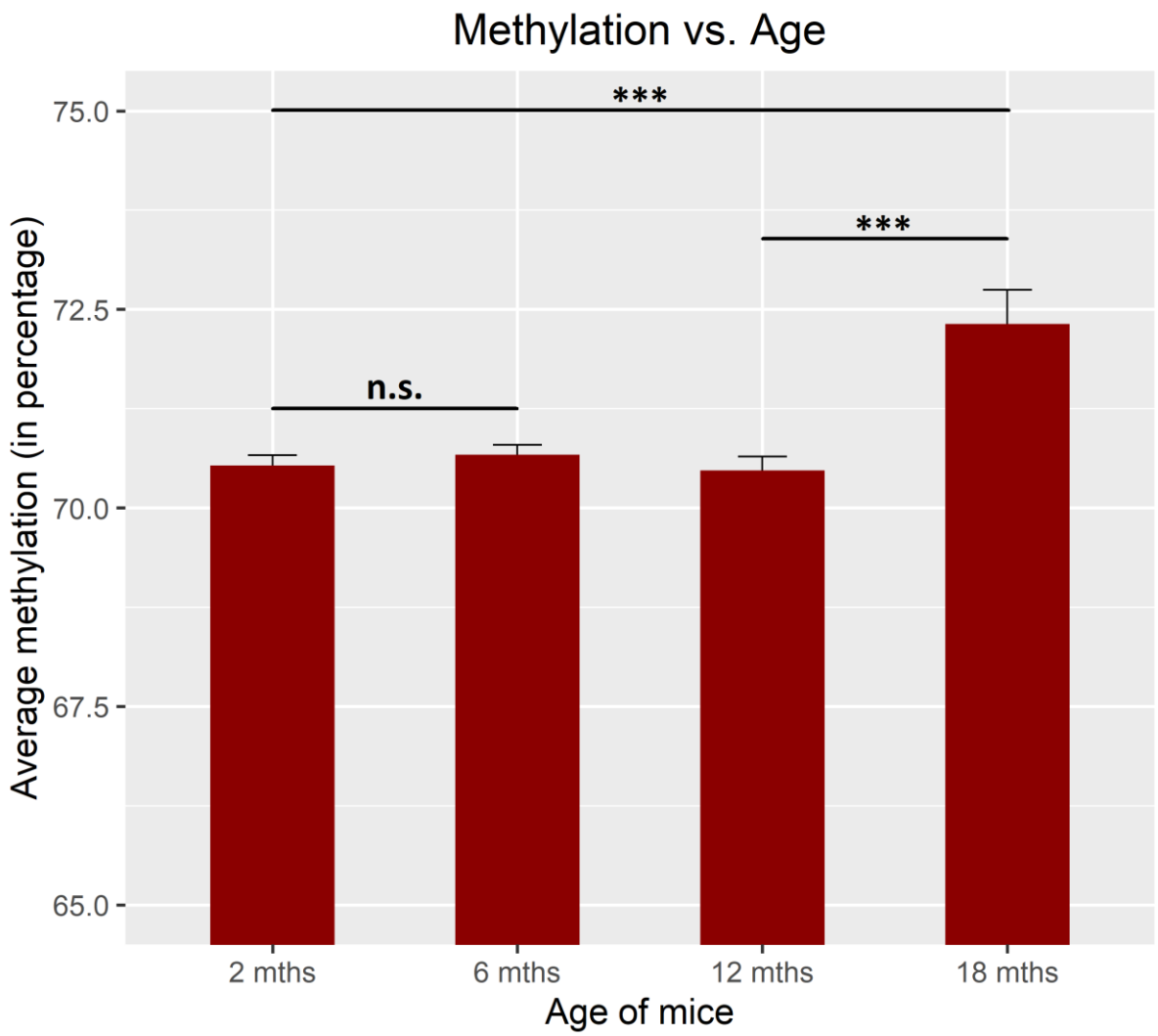

Figure 3.24 | ECs isolated from the brains of 18 months-old mice show increased methylation level compared to the 2, 6 and 12 months-old mice. The average methylation level across all the CpGs investigated by RRBS was 70.52 % (sd = 0.46) in the 2 months-old mice, 70.66% (sd = 0.27) in 6 months-old, 70.46% (sd = 0.53) in 12 months-old and 72.30% (sd = 1.17) in 18 months-old mice. The average methylation level of CpGs in the ECs isolated from 18 months-old mice is significantly higher in comparison to the 2, 6 and 12 months-old mice (adjusted p-values < 0.01). However, no significant change in the level of methylation is observed in the 6 or 12 months-old mice in comparison to the 2 months-old mice. Error bars represent mean ± se (standard error of the mean). One-way analysis of variance (ANOVA), followed by Tukey's HSD test were performed to compare all the possible pairs. (**n.s.** : non-significant, ******* : $p < 0.001$)

3.20 Linear regression analysis on RRBS data reveals genomic loci annotated to *Arid5b* and *Adgrg1* genes undergo change in methylation level with age.

To determine the differentially methylated regions, the genome was divided into a sliding window of 1000 base pair (bp) long, non-overlapping tiles using Methylkit, an R based software for DNA methylation analysis. Differentially methylated sites were investigated in the 1000 bp tiles having at least 2 CpGs and a minimum average coverage of 5 across all the samples. Linear regression analysis across all timepoints (2 months, 6 months, 12 months and 18 months) was performed on these 1000 bp non-overlapping tiles. The linear regression analysis on the data included the correction for sex and technical parameters such as coverage and batch. Out of the 163,977 tiles having a length of 1000 bp, only two tiles showed a statistically significant change (adjusted p-value < 0.05) in methylation with age.

The first tile that shows an age-dependent change in methylation level corresponds to chromosome 10, with the coordinates being 68120001 – 68121000. The closest gene associated with this 1000 bp tile was annotated, both computationally and using manual inspection of publicly available genome browsers, to *Arid5b.* The *Arid5b* gene is located 157727 bp downstream of this 1000 bp tile. The average methylation of CpGs in the tile displays a progressive reduction with a correlation coefficient of 0.875 (Figure 3.25), suggesting that 87.5% of the variance in the level of CpG methylation in the tile can be attributed to age (adjusted p-value = 0.007).

Another tile that shows a significant age-dependent change in methylation level corresponds to chromosome 8, with the coordinates spanning from position 94985001 to 94986000. The closest gene associated with this 1000 bp tile was annotated, both computationally and using manual inspection of publicly available genome browsers, to *Adgrg1*. The *Adgrg1* gene is situated 602 bp upstream of the tile. The average methylation of CpGs in the tile displays a progressive reduction with a correlation coefficient of 0.815 (Figure 3.25), suggesting that 81.5% of the variance in the level of CpG methylation in the tile can be attributed to age (adjusted p-value = 0.036).

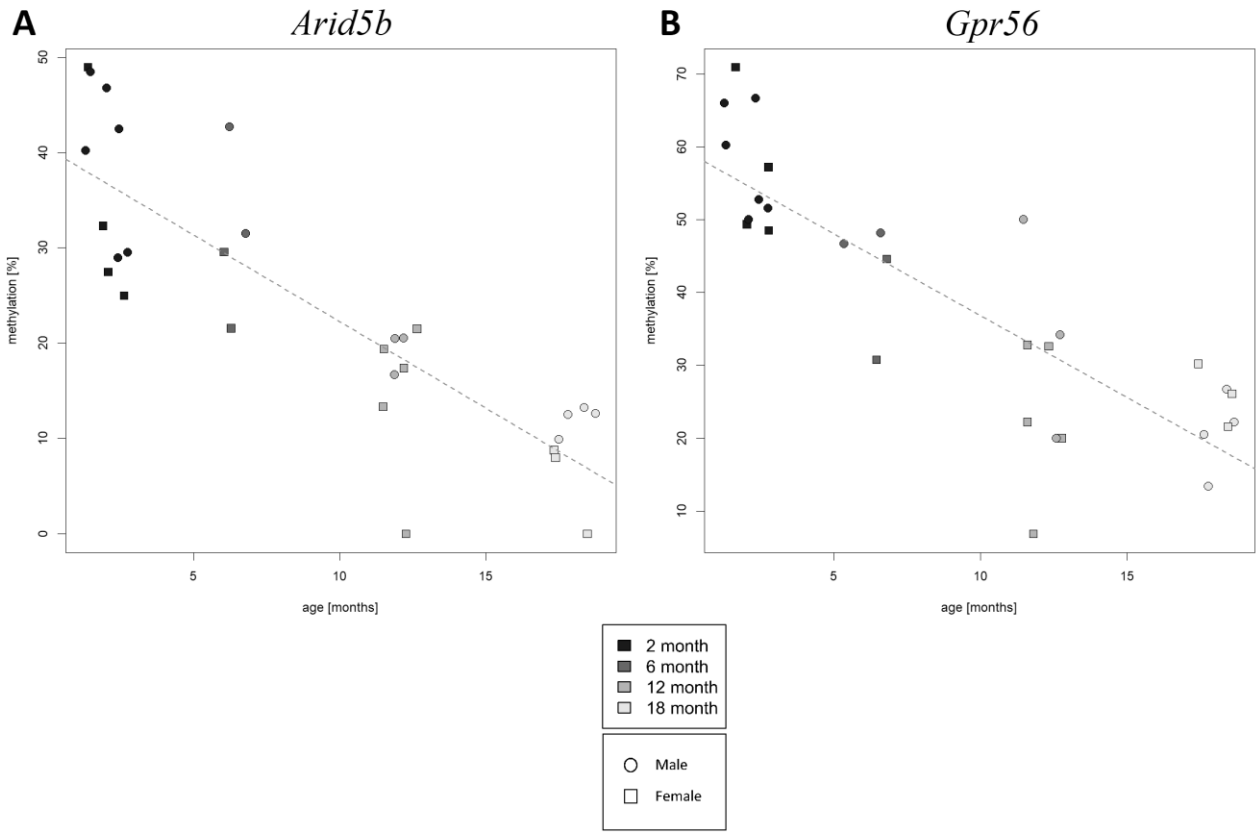

Figure 3.25 | Genomic loci associated with *Arid5b* and *Adgrg1* (Gpr56) undergo reduction in methylation level with age. (A) The 1000 bp tile with coordinates 68120001 – 68121000 on chromosome 10 shows age-dependent reduction in the methylation levels of CpGs. The closest gene annotated to the tile is *Arid5b,* which is located 157727 bp to the downstream of the tile. The correlation coefficient is 0.875 (adjusted p-value = 0.007). **(B)** The 1000 bp tile with coordinates 94985001 – 94986000 on chromosome 8 also shows age-dependent reduction in the methylation levels of CpGs. The closest gene annotated to the tile is *Adgrg1,* which is situated 602 bp upstream to this tile. The correlation coefficient is 0.815 (adjusted p-value = 0.036). No other tile among the 163,977 continuous, non-overlapping 1000 bp tiles exhibited any significant age-dependent change in methylation levels. The RRBS analysis was performed by Dr. Gilles Gasparoni (University of Saarland, Saarbrücken).

3.21 ATAC-seq analysis reveals age-dependent decrease in chromatin accessibility.

(*The ATAC-seq study was performed in collaboration with the group of Prof. Dr. Jörn Walter at the University of Saarland, Saarbrücken. The ATAC-seq libraries were prepared by myself; sequencing was performed by Dr. Gilles Gasparoni; data analysis and interpretation were performed by Abdulrahman Salhab, Saarbrücken*).

Chromatin remodeling is a major process which plays an important role in regulation of transcription. The regions of open chromatin indicate access to the transcription machinery suggesting active transcription, while closed chromatin indicates repression of transcription. Assay for transposase-accessible chromatin sequencing (ATAC-seq) was performed to detect the age-dependent changes in chromatin accessibility, which depicts regions of active transcription (open chromatin) and inactive transcription (condensed chromatin).

ATAC-seq library was prepared from ECs isolated from mice aged 2, 6, 12 and 18 months. Mice aged 2 months (1 male, 3 females), 6 months (2 males, 3 females), 12 months (2 males, 3 females) and 18 months (3 males, 3 females) were considered for ATAC-seq data analysis. Two males belonging to the 2 months-old group, one male from each of the 6 and 12 months-old groups were excluded from sequencing due to poor library quality. The excluded samples had a very low FriP score, defined as the fraction of reads that fall into a peak.

An average of 51.6 million total mapped reads per sample were obtained, of which 26.1 million reads mapped without duplication and 94.48% of the reads in each sample mapped to the genome. On average, 33254 called peaks were identified across all the samples sequenced. The samples cluster according to their ages in the principal component analysis plot (Figure 3.26), with the younger mice (2 and 6 months) showing a clear separation from the older group (12 and 18 months). However, the PCA plots of the samples did not indicate differences between the ATAC profiles of males and females. Since no difference was observed between the sexes in the PCA, the males and females of each age group were pooled, and ATAC-seq analysis was performed to study the change in chromatin accessibility with age.

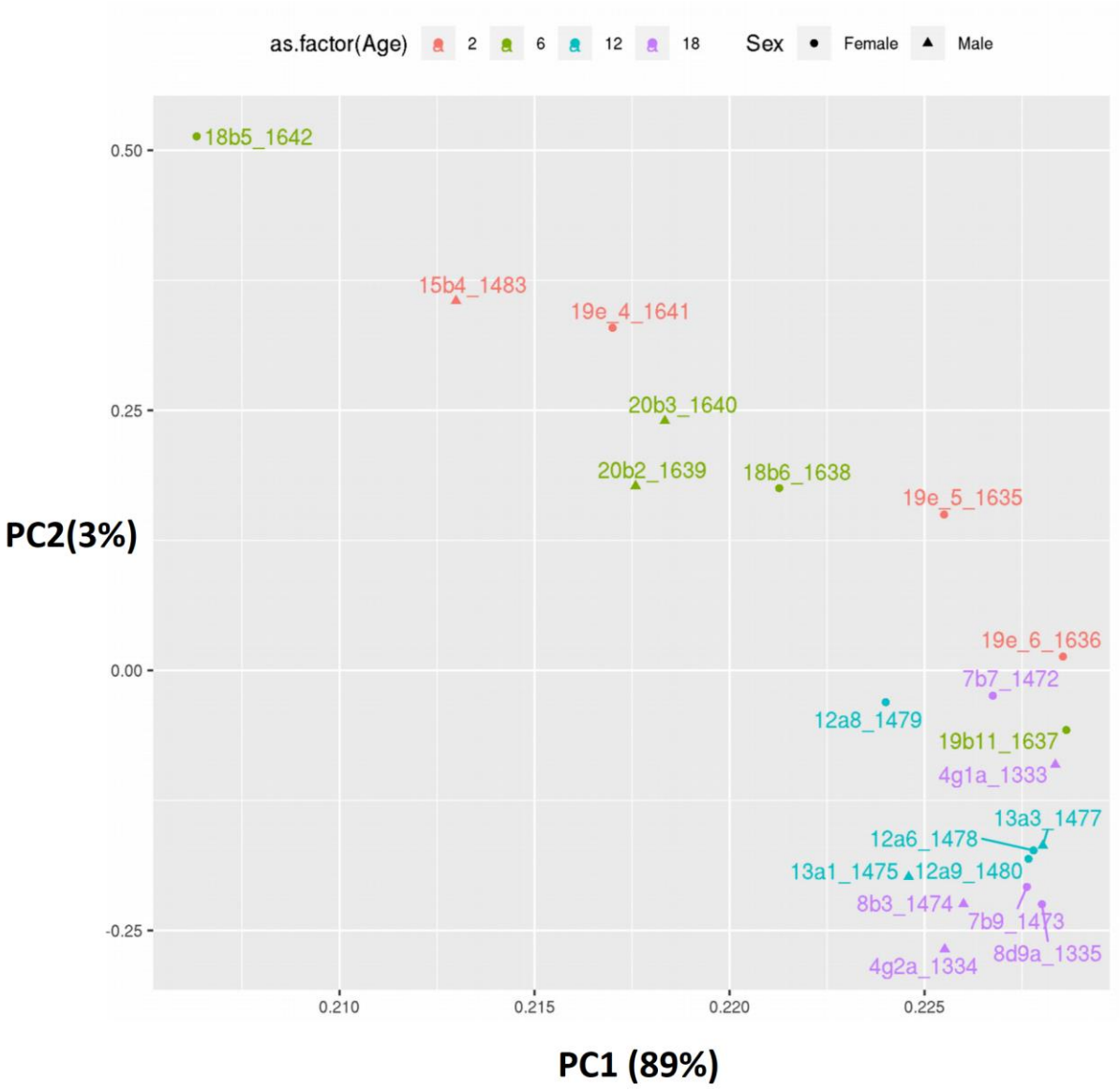

Figure 3.26 | Principal component analysis of samples (ATAC-seq study). The Principal Component Analysis (PCA) plot indicates that the ATAC-seq profiles of the older mice (12 and 18 months) are different from the profiles of the younger mice (2 and 6 months) as the younger and the older groups cluster separately. However, no clear difference between the ATAC profiles of males and females is visible. The ATAC-seq analysis was performed by Abdulrahman Salhab (University of Saarland, Saarbrücken).

To investigate the differential chromatin accessibility with age, linear regression analysis was performed after peak calling with MACS2. To visualize age-dependent changes in the chromatin accessibility, TCseq – an R based package to analyze the sequencing data over a time course – was used. The differential analysis of ATAC-seq data to investigate the age-dependent changes in the chromatin accessibility revealed that majority of called peaks show a decrease in chromatin accessibility with age.

A total of 2290 peaks were found to have significantly differential age-dependent changes in chromatin structure. These peaks include promoters, intergenic regions, introns, CDS (coding sequence) and exons. Of the 2290 peaks found to show significant age-dependent changes in the chromatin structure, TCseq analysis segregated them in six clusters based on how the chromatin accessibility at those peaks change with age (Figure 3.27). The peaks belonging to clusters 1 – 5 become more accessible at 6 months in comparison to 2 months, and then become less accessible (i.e. 'close') in the older mice belonging to 12 and 18 months-old groups. However, the peaks in cluster 6 show a trend completely opposite to the clusters 1 – 5. In cluster 6, the peaks show reduced accessibility at 6 months of age as compared to the 2 months. The chromatin accessibility (i.e. opening of regions) increases in the older mice aged 12 months, and again reduces in the 18 months-old mice. Overall, ATAC-seq data reveal two broad patterns of age-dependent changes in chromatin structure and the peaks belonging to five clusters 1 – 5 that follow a similar trend, can be combined together into a single cluster (Figure 3.28).

A total of 2013 peaks belong to cluster 1 – 5 (425 in cluster 1, 244 in cluster 2, 486 in cluster 3, 406 in cluster 4 and 452 in cluster 5) and 277 in cluster 6. Overall, the differential analysis of ATAC-seq data suggest that the majority of the peaks (2013/2290) become less accessible (i.e. close) in the cerebral ECs of older mice (12 and 18 months-old), while the remaining (277/2290) become more accessible (i.e. open) in the older mice.

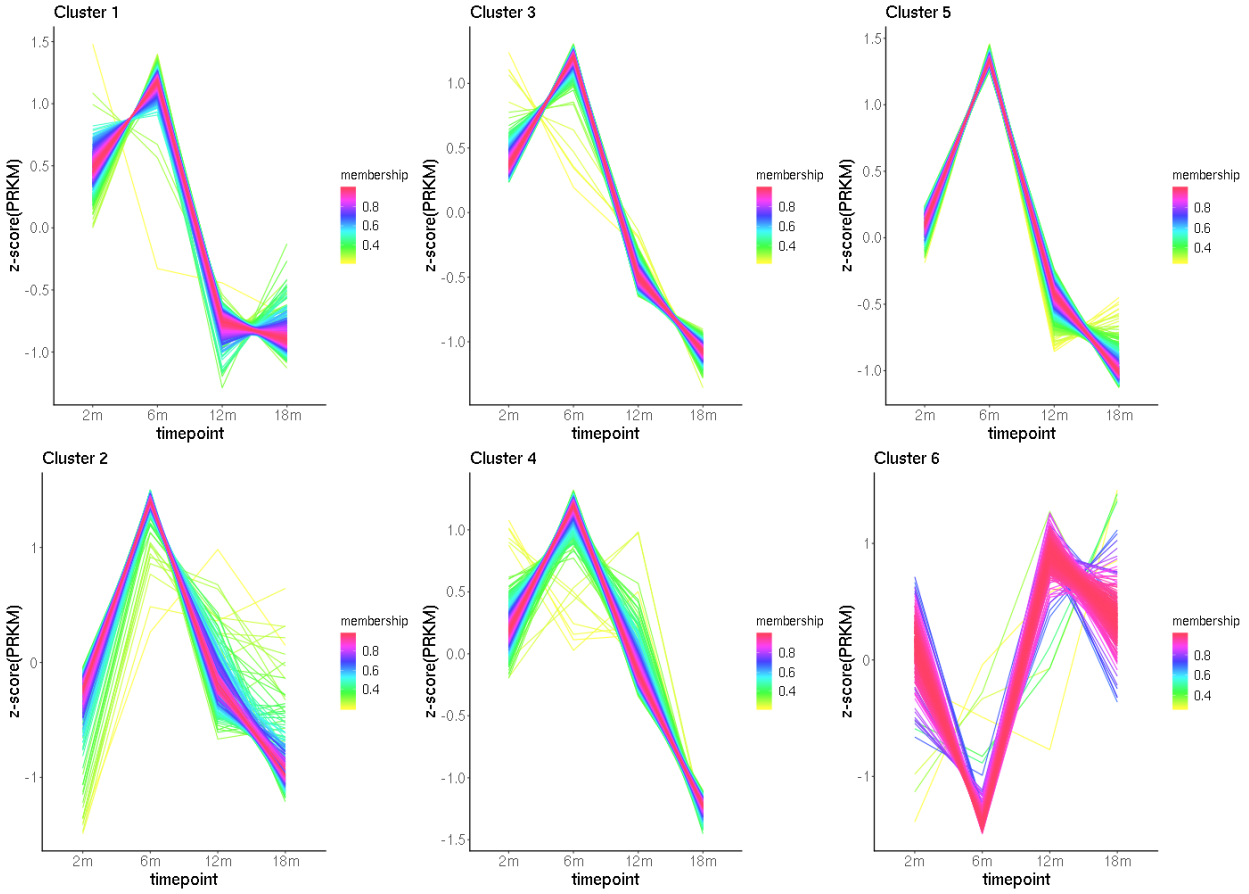

Figure 3.27 | ATAC-seq analysis reveals age-dependent change in chromatin accessibility. The differential analysis of ATAC-seq data using TCseq to investigate the age-dependent changes in the chromatin accessibility reveals that majority of called peaks show a decrease in chromatin accessibility with age, suggesting that the majority of regions change from ‘open’ in younger age-groups to ‘closed’ in the older mice. The peaks have been segregated into six clusters depending on the age-dependent changes in chromatin accessibility. While the peaks belonging to the clusters 1-5 show an overall similar trend, i.e. open in the younger group and closed in the older group, the regions in cluster 6 show a tendency of increase in chromatin accessibility, i.e. opening of regions in the older groups (12 and 18 months). While a positive z-score value indicates that the region is ‘open’, a negative z-score means a closed region. The analysis was performed by Abdulrahman Salhab (University of Saarland, Saarbrücken).

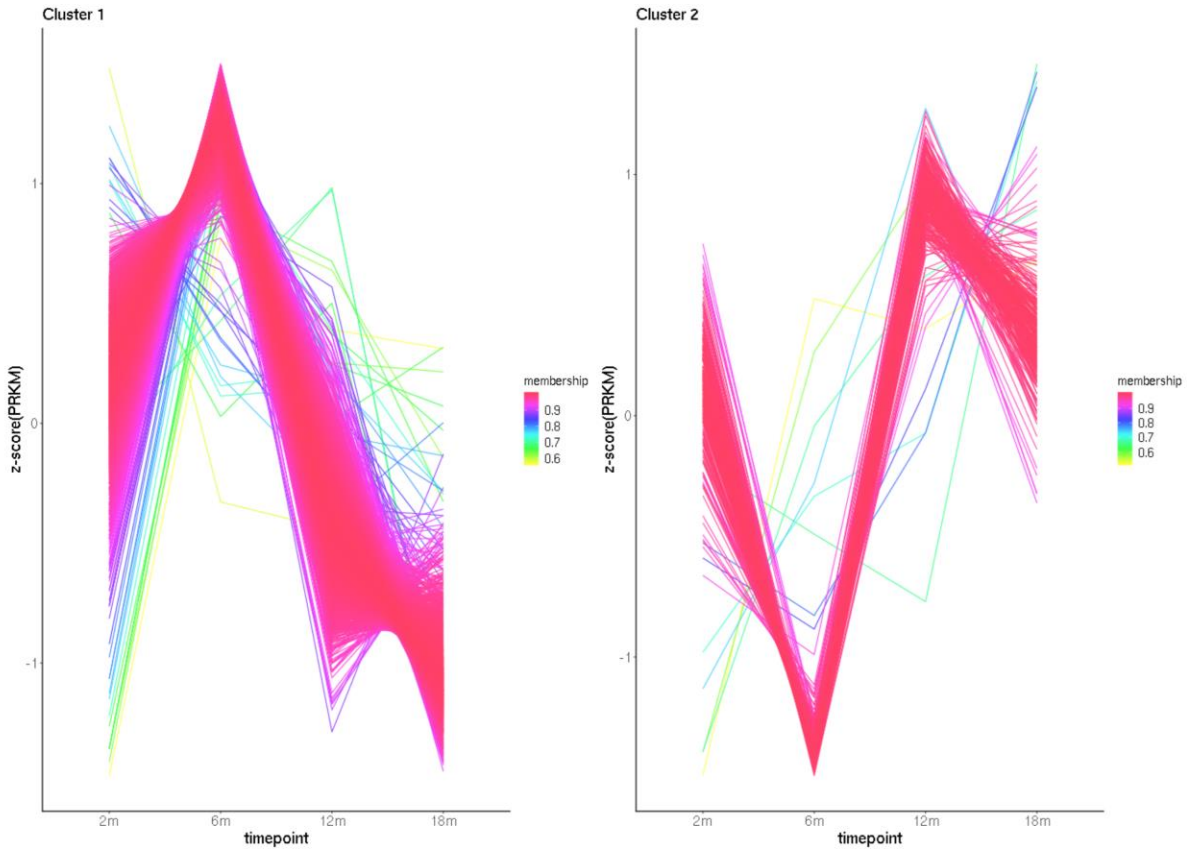

Figure 3.28 | TCseq analysis of ATAC-seq data reveals two broad patterns of age-dependent changes in chromatin structure. The differential analysis of ATAC-seq data to investigate the age-dependent changes in the chromatin accessibility reveals two major patterns of age-dependent differential chromatin structure. The peaks belonging to five clusters 1 – 5 in the initial TCseq analysis (Figure 3.27) follow a similar trend and have been combined together into a single cluster. In the above figure, the peaks in cluster 1 have enhanced chromatin accessibility, i.e. 'open' in the younger group and show reduced chromatin accessibility, i.e. become 'closed' in the older group. The peaks belonging to cluster 2 show a tendency of increase in chromatin accessibility, i.e. opening of regions in the older groups (12 and 18 months) and is the same as cluster 6 in the previous TCseq analysis (Figure 3.27). While a positive z-score value indicates that the region is 'open', a negative z-score means a closed region. The analysis was performed by Abdulrahman Salhab (University of Saarland, Saarbrücken).

3.22 Combining ATAC-seq and RNA-seq analysis does not reveal a definitive relationship between genome structure and gene expression in cerebral ECs.

Since the changes in chromatin structure are known to regulate gene expression, ATAC-seq and RNA-seq analysis were combined to investigate the relationship between chromatin accessibility and transcription in the cerebral ECs. To study the correlation between the two processes, peaks in cluster 1 and 2 from the ATAC-seq data were considered and those peaks that overlap repeats were removed. These peaks were then compared with the expression of the associated genes. The comparison does not suggest a definitive relationship between gene expression and the chromatin accessibility in cerebral ECs (Figure 3.29). While the peaks belonging to cluster 1 of ATAC-seq data show a reduction in chromatin accessibility with age, most of the corresponding genes associated with the peaks do not show a progressive decrease in gene expression with age. Also, the peaks belonging to cluster 2 of ATAC-seq data show an increase in chromatin opening with age. However, there are very few genes associated with the peaks and the change in expression of those genes do not show any definitive relationship with the age-dependent changes in the chromatin structure (Figure 3.30).

The correlation between the RNA-seq and ATAC-seq data was also investigated manually. The list of peaks belonging to cluster 1 and 2 from the ATAC-seq data were compared with the list of 1388 dysregulated genes obtained by the linear regression analysis of the RNA-seq data. Out of 2013 peaks belonging to cluster 1 that show an age-dependent reduction in chromatin accessibility, i.e. closing of chromatin with age, there are 22 peaks associated with 20 genes that associate with age-dependent downregulation of gene expression. These genes include *Gnb4*, *Serpine2*, *Casp8*, *Aplnr*, *Cacna1e*, *Pdia6*, *Tspan13*, *St3gal6*, *Tyw1*, *Tsn*, *Arhgap28*, *Tmsb10*, *Prnp*, *Ptprd*, *Zwint*, *Klhl6*, *Rgl1*, *Pcca* and *Lrrfip1*.

On the other hand, out of 277 peaks in cluster 2 that show an age-dependent increase in chromatin accessibility, i.e. opening with age, there are 5 peaks associated with 5 genes belonging to cluster 2 that associate with age-dependent upregulation of gene expression. These genes include *Arrdc3*, *Zc3h12b*, *Cdk14*, *Chd9* and *Ric3*.

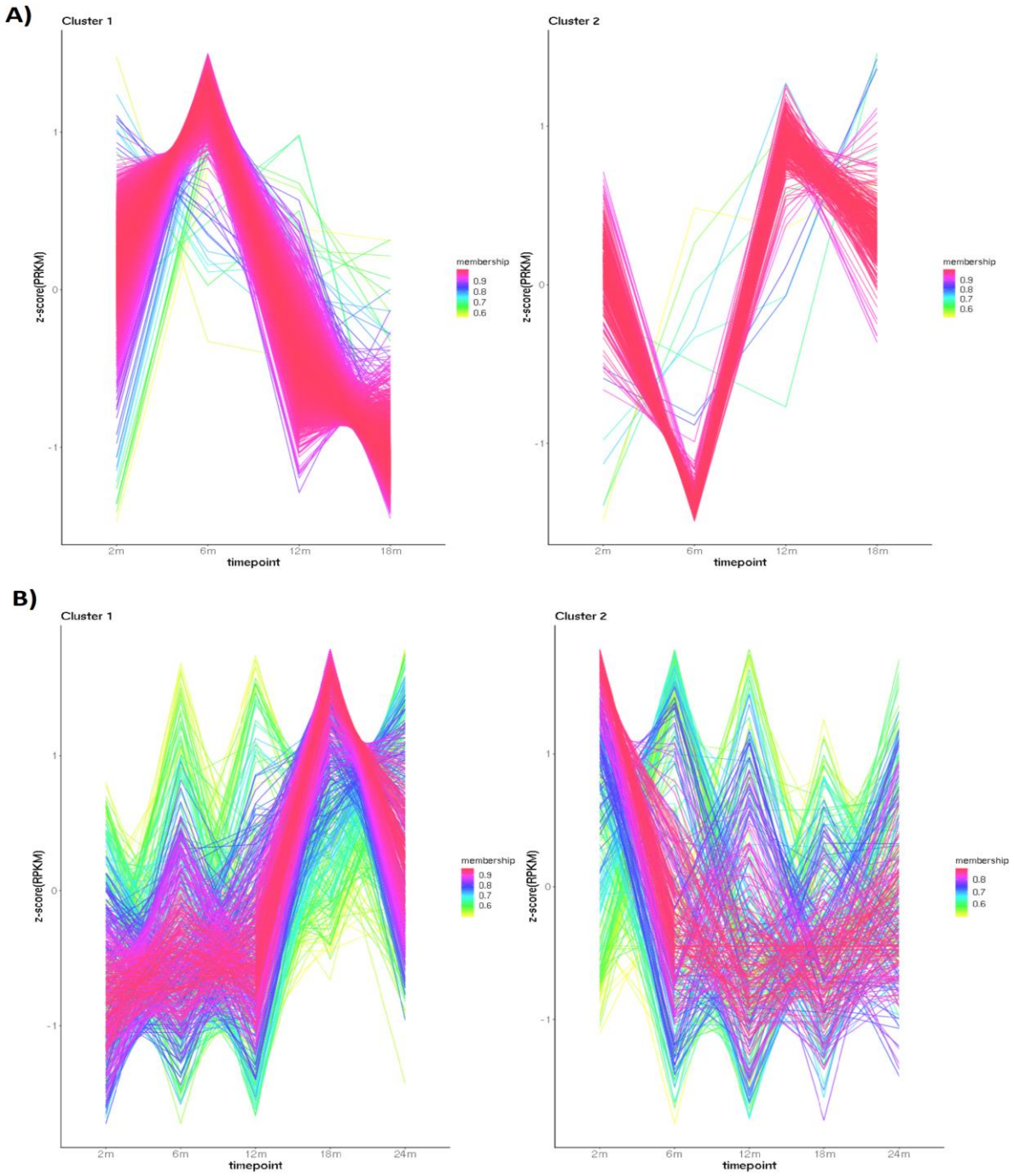

Figure 3.29 | TCseq analysis of ATAC-seq and RNA-seq data. The time course analysis performed on **(A)** ATAC-seq and **(B)** RNA-seq data classify peaks and genes into two clusters based on age-dependent changes in chromatin accessibility and gene expression, respectively. There is more dynamism in the age-dependent changes in the gene expression than changes in chromatin structure. However, there is no definitive relationship between the genome structure and gene expression in the cerebral ECs. TCseq analysis was performed by Abdulrahman Salhab (University of Saarland, Saarbrücken)

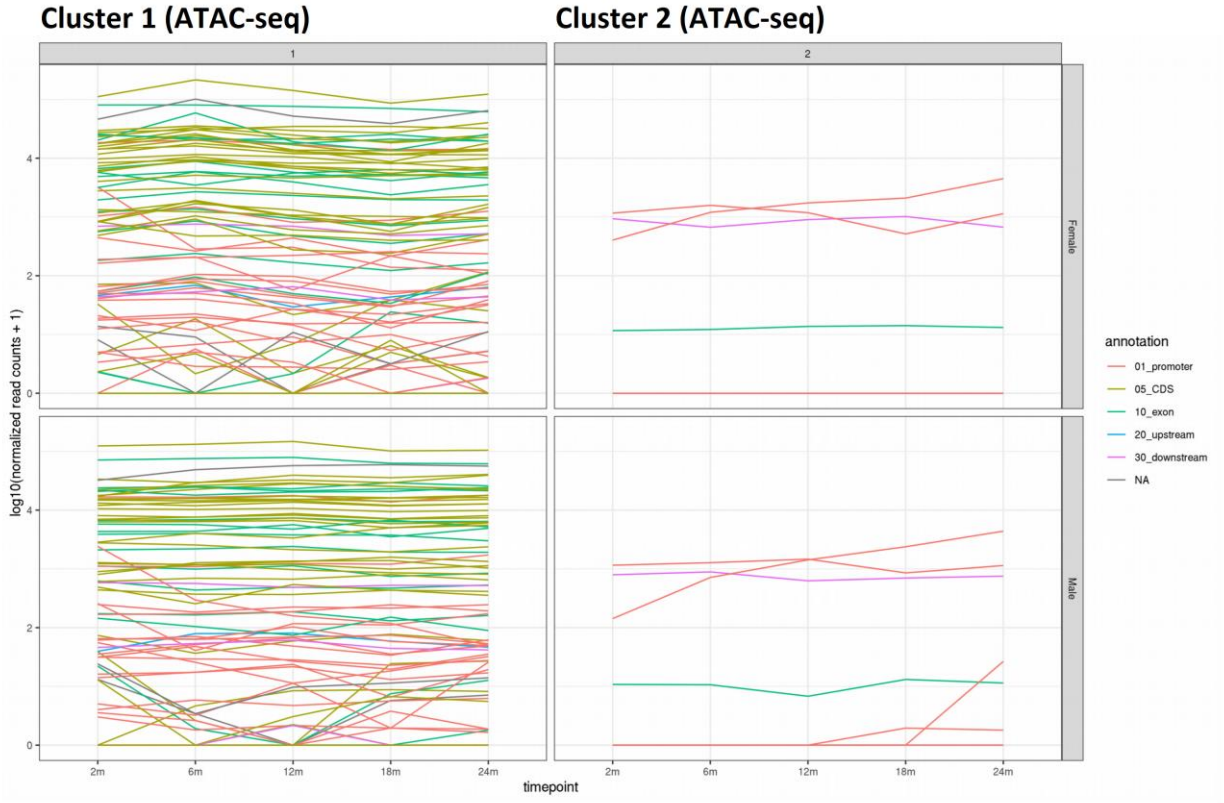

Figure 3.30 | ATAC-seq and RNA-seq analyses do not suggest a definitive relationship between genome structure and gene expression in cerebral ECs. Peaks in cluster 1 and 2 from the ATAC-seq data were considered and after removing the peaks that overlap repeats, were then compared with the expression of the associated genes. Out of 2013 peaks belonging to cluster 1 of ATAC-seq data that show a reduction in chromatin accessibility with age, most of the corresponding genes associated with the peaks do not show a progressive decrease in gene expression with age. There are 22 peaks associated with 20 genes that associate with age-dependent downregulation of gene expression. Similarly, among 277 peaks belonging to cluster 2 of ATAC-seq data that show an increase in chromatin opening with age, there are 5 genes associated with 5 peaks that show an age-dependent upregulation of gene expression. The comparison between ATAC-seq and RNA-seq was performed by Abdulrahman Salhab (University of Saarland, Saarbrücken).

3.23 Expression of apelin receptor protein in mouse brains decreases with age.

A significant observation in the RNA-seq data obtained from the cerebral ECs of mice belonging to different age-groups (2,6,12,18 and 24 months) was the age-dependent strong downregulation of *Aplnr* gene, encoding the apelin receptor protein. Interestingly, ATAC-seq data revealed age-dependent reduced chromatin accessibility of the peak that was annotated as the promoter region of *Aplnr* gene. The age-dependent strong downregulation of *Aplnr* gene in the cerebral ECs becomes significant given that the peak mapped to the promoter of *Aplnr* since reduced chromatin accessibility at the promoter region is associated with reduced transcription.

To investigate the expression levels of apelin receptor protein in the brains of ageing mice, western blotting was performed on the whole brain lysates prepared from 2 months- and 18 months-old mice. Whole brain lysates were prepared from 3 male mice (littermates) belonging to each of the 2 months- and 18 months-old age groups. While the average signal intensity of apelin receptor (normalized to the signal intensity of GAPDH used as a loading control) was 0.89 (sd = 0.44) in the brain lysates prepared from the 2 months-old mice, the average signal intensity of apelin receptor (normalized to the signal intensity of GAPDH used as a loading control) was 0.58 (sd = 0.19) in the 18 months-old age group. Western blot analysis showed a significant reduction (p value < 0.05) in the expression of apelin receptor in the brains of 18 months-old mice as compared to the 2 months-old mice (Figure 3.31).

Similarly, western blot was also performed to investigate the levels of claudin-5 (CLDN5) and integral membrane protein 2a (ITM2A) in the brain lysates of 2 and 18 months-old mice. However, no definitive conclusion could be deduced due to inconsistent signals of CLDN5 and ITM2A in the western blot analysis (images not shown).

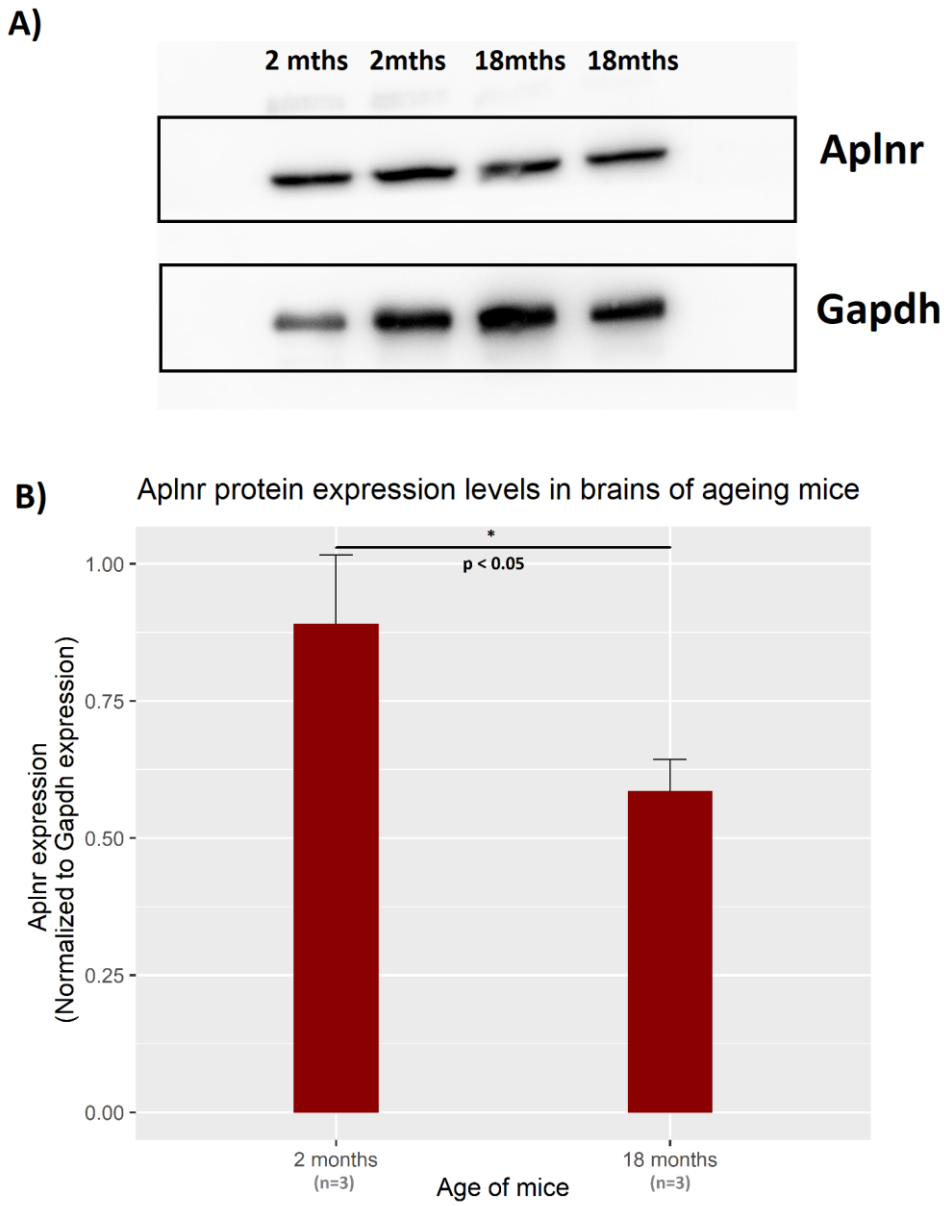

Figure 3.31 | Aged mice exhibit reduced levels of apelin receptor protein in the brain. **(A)** Immunoblot showing the expression of APLNR and GAPDH proteins in brain lysates prepared from the brains of 2 months-old and 18 months-old mice. **(B)** Western blot analysis showed a significant reduction (p value < 0.05) in the expression of apelin receptor in the brains of 18 months-old mice as compared to the 2 months-old mice. The average signal intensity of apelin receptor (normalized to the signal intensity of GAPDH) is 0.89 (sd = 0.44) and 0.58 (sd = 0.19) in the brain lysates prepared from the 2 months- and 18 months-old mice, respectively. Lysates prepared from three mice belonging to both the age-groups were used for western blot studies and the experiment was repeated four times.

Chapter 4

Discussion

4. Discussion

4.1 The incidents of cerebral bleedings in mice increase with age.

The study was performed on wild-type mice and mice having floxed, yet non-recombined *Srf* and *Mrtf* alleles, thereby having functional *Srf* and *Mrtf* genes (wild-type phenotype) belonging to different age-groups, to establish the correlation between incidents of bleedings in the brain with advancement in age. Hematoxylin-eosin (H&E) staining was performed to investigate and quantify the number of fresh incidents of cerebral bleedings in mice. The use of H&E staining to detect fresh cerebral bleedings concurs with the study conducted by Liu et al. (2014)[190]. In their study, Liu et al. concluded that H&E staining is effective in identifying fresh hemorrhages, while the Prussian Blue staining detects old pre-existing hemorrhages.

This study reveals that the incidents of cerebral bleedings in mice progressively increase with ageing. The bleedings were observed in all the regions of the brain and were not restricted to any specific region. In human patients, increasing age is the biggest risk factor for intracerebral hemorrhage (ICH) with the incidence of ICH increasing progressively with age[5]. These observations in ageing mice reflect the increased incidents of ICH in elderly human patients. ICH is associated with disruption of the blood-brain barrier (BBB) and rupture of blood vessels, leading to the leakage of blood into brain tissues. Several studies in mice have demonstrated the breakdown of BBB with age, leading to increased BBB permeability[149, 191]. Since endothelial cells (EC) form the core component of the BBB in the central nervous system vasculature and provide a physical barrier, this study characterized the age-dependent transcriptomic and epigenetic changes in ECs implicated in BBB breakdown and development of cerebral bleedings with age.

4.2 The transcript profile of cerebral ECs changes with age.

Naturally ageing Cdh5-mT H2B-GFP mice were used as a model to investigate the age-dependent transcriptomic and epigenetic changes occurring in the cerebral ECs. These mice express – with high specificity in the ECs – green fluorescence in the nuclei and tomato fluorescence in cell membrane, thereby assisting in FACS-based sorting of pure EC population. The changes in the EC transcriptome with age were characterized using RNA-seq analysis performed on the cerebral ECs isolated from 2,6,12,18 and 24 months-old mice.

The gene expression profiles of older mice (18 and 24 months-old) are markedly different from the profiles of younger mice (2 and 6 months-old), as revealed by the principal component analysis of the RNA-seq data (Figure 3.10), suggesting dysregulation of gene expression with ageing. The age-dependent dysregulation of genes in ECs observed in this study is in agreement with various studies on humans and mice which have demonstrated dysregulation of gene expression with ageing in a number of tissues and cells[192-196].

Pairwise comparisons of each of the 6, 12, 18 and 24 months-old with 2 months-old group, considering the males and females of each age-group separately, were performed to characterize the change in gene expression profiles in the cerebral ECs of mice with advancement of age. Interestingly, the number of dysregulated genes in females is much larger than the number of genes dysregulated in the males of the corresponding age-groups. The large bias in the results obtained from the differential expression analysis depending on the inclusion or exclusion of female mice may be attributed to asynchronized estrous cycle in the littermates. The fluctuating levels of hormones in female littermates at any particular time may affect the expression levels of various genes, resulting in the bias between the males and females. Therefore, in all further pairwise analysis to identify the candidate genes whose dysregulation may contribute to the age-dependent increase in the incidents of cerebral bleedings, only males were considered, and females were excluded from analysis.

In addition to the pairwise comparison of gene expression between different age-groups, linear regression analysis was also performed on RNA-seq datasets to identify genes that are progressively dysregulated with age. Linear regression analysis was performed on RNA-seq data for all the thirty samples across all time points (2,6,12,18 and 24 months), adjusting for the sex-specific effects. A total of 1388 genes were found to be significantly dysregulated. While 675 genes were found to be significantly downregulated (t.value.age < 0) with age, 713 were upregulated (t.value.age > 0) with age in the linear regression analysis performed on RNA-seq data.

4.3 The pathways associated with inflammatory response and apoptosis are upregulated with age in the cerebral ECs.

Gene set enrichment analysis (GSEA) performed on the RNA-seq dataset revealed that several pathways implicated in inflammatory response were significantly upregulated with age in the cerebral ECs. These include the pathways involving interferon alpha response, interferon gamma response, allograft rejection and TNFα signaling via NF-κB. Pierce et al. (2009) have demonstrated that the activation of NF-κB pathway leads to the stimulation of oxidative stress in older humans, leading to vascular endothelial dysfunction[197]. Other studies have suggested age-dependent increase in oxidative stress due to mitochondrial dysfunction, dysregulation of renin-angiotensin system and multiple pro-inflammatory pathways activate the NF-κB signaling, resulting in cerebrovascular diseases (reviewed by Csiszar et al., 2008)[198]. Furthermore, the observation that the pathways associated with inflammation in the cerebral ECs of older mice are in agreement with the study conducted by Elahy et al. (2015)[191]. In their study, Elahy et al. demonstrated that naturally aged mice (24 months-old) exhibit BBB disruption and increased capillary permeability as compared to 3 months-old mice, strikingly similar to the observations of age-dependent increase in the cerebral bleedings in this study. Furthermore, Elahy et al. demonstrated that the older mice show significantly enhanced inflammation and higher levels of NF-κB in the vasculature. Other studies have also confirmed the age-dependent increase in expression of NF-κB in the ECs and the vascular endothelium developing a pro-inflammatory profile with age[199, 200].

Apoptosis is a distinctive feature of ageing, and more importantly in age-related loss of cells in several organs. Wang et al. have established that ageing leads to increased apoptosis in the capillary ECs in skeletal muscle[198]. The study further demonstrated that age-dependent increase in the apoptosis of capillary ECs leads to altered levels of critical angiogenic regulators, thereby leading to impaired functionality of the vasculature. Interestingly, the GSEA in this study reveals upregulation in the pathways associated with apoptosis in the cerebral ECs of 18 and 24 months-old mice. An interesting observation of the study has been reduction in the yield of cerebral ECs with ageing, which can be attributed to technical reasons. Much larger amounts of myelin and cellular debris are obtained during the process of preparing single-cell suspension from the brains of 18 and 24 months-old mice (visual observation, not quantified). A plausible explanation for reduced yield of cerebral ECs

from older mice is loss of ECs during the step of myelin and cellular debris removal. Also, the lesser yield of ECs from 18 and 24 months-old mice might be due to the reduction in the total number of ECs in the brain of ageing mouse as a result of age-dependent increase in apoptosis. Whether age-dependent increase in apoptosis plays a role in the dysfunction of cerebral microvessels by the reduction in cerebral EC coverage remains to be investigated.

4.4 *Srf* and *Mrtf* expression levels in cerebral ECs do not change with age.

Weinl et al. (2015) have shown that both postnatal and adult EC-specific deletion of SRF, as well as its cofactors MRTF-A and MRTF-B, result in intracerebral hemorrhaging, accompanied by stroke-like symptoms in these knock-out animals. *Srf* ^{iECKO} mice had significantly reduced mRNA levels of proteins encoding components of TJ, AJ and basement membrane. These findings suggested that SRF directly or indirectly regulates the expression of target genes encoding proteins that are components of TJs, AJs, basement membranes and other structures involved in endothelial cell-cell adhesion, thereby playing an important role in the formation and maintenance of a functional BBB[169].

This study was undertaken with the initial hypothesis that an increase in the incidents of bleedings in the brains of normally aged mice may be due to the age-dependent downregulation of *Srf/Mrtf* function, the dysregulation of SRF/MRTF target genes and other genes responsible for maintenance of BBB and vascular integrity in cerebral ECs. However, no age-dependent significant dysregulation of *Srf* or *Mrtf* was observed in this study. Although no age-dependent changes in the transcript levels of *Srf* or *Mrtf* were found in the cerebral ECs, unaltered mRNA levels do not necessarily correlate with the expression and activity levels of the corresponding proteins. Whether the expression of SRF and MRTF proteins, and their activity also remain unchanged in the cerebral ECs of ageing mice need to be further investigated.

To characterize the SRF target genes that are dysregulated with age in cerebral ECs, this study compared the 1388 differentially expressed genes with the list of ~1000 known SRF target genes in the cultured NIH3T3 cells (Esnault et al. 2014)[164]. Among 1388 genes that were significantly dysregulated with age in cerebral ECs, 88 genes (~6 %) were SRF targets. While 46 SRF target genes were found to be significantly downregulated, 42 were significantly upregulated with age. Furthermore, the study identified 16 SRF target genes involved in cytoskeletal dynamics to be significantly dysregulated with age in cerebral ECs.

While 10 genes were significantly downregulated, 6 were significantly upregulated (Tables 3.3 – 3.5). Upon considering the common SRF target genes regulating cytoskeletal dynamics that were significantly dysregulated in both the 18 months vs. 2 months-old pairwise comparison and linear regression analysis, 3 genes (*Fyn*, *Tubb6* and *Dcaf12*) were found to be downregulated and 2 genes (*Trio* and *Myh9*) were upregulated. Further studies are required to understand if these SRF target genes involved in cytoskeletal dynamics also play a role in the maintenance of BBB.

Weinl et al. had reported significantly reduced transcript levels of proteins encoding components of TJ, AJ and basement membrane in *Srf* ^{iECKO} mice. Interestingly, this study finds a number of key genes implicated in the maintenance of BBB to be downregulated with age (discussed in 4.5 – 4.7). Since the list of ~1000 SRF target genes by Esnault et al. (2014) are based on studies in the cultured NIH3T3 fibroblasts, there could be cerebral EC-specific SRF target genes which we do not know about.

4.5 Among genes that constitute the major structural components of the blood-brain barrier, *Cldn5* is downregulated with age.

The study identified age-dependent downregulation of claudin-5 in the cerebral ECs. Claudin-5 was downregulated in the cerebral ECs isolated from 18 months-old mice (as compared to 2 months-old mice) and also showed significant age-dependent downregulation in the linear regression analysis performed on RNA-seq dataset from all the age-groups (2,6,12,18 and 24 months). Claudin-5 is an endothelial-specific, highly expressed, vital component of the tight junctions in the cerebral ECs and plays a crucial role in imparting the barrier properties to the BBB. Several studies have demonstrated the disruption of BBB and impaired vascular integrity with loss of claudin-5[56, 201]. The age-dependent downregulation of *Cldn5* in the cerebral ECs of mice and increased BBB permeability with ageing is also demonstrated by Elahy et al. (2015)[191].

Weinl et al. (2015) demonstrated that the expression of claudin-5 protein was significantly downregulated in the brain lysates from *Srf*^{iECKO} mice. They also showed that the expression of *Cldn5* gene was downregulated in the cultured mouse ECs (mECs) transfected with siRNA against *Srf* [169], suggesting that claudin-5 could potentially be regulated by

SRF/MRTF in the ECs. However, further studies are needed to conclusively establish whether *Cldn5* is an SRF target gene in the cerebral ECs.

A number of *in vitro* and *in vivo* studies have suggested that inflammatory cytokines downregulate the expression of the components of TJ, as well as induce the degradation of the TJ complex[202, 203]. In humans, ageing leads to enhanced circulation of cytokines and inflammatory molecules including TNF-α and interleukins in the blood[204]. The GSEA showing upregulation of inflammatory pathways and the downregulation of *Cldn5* in the ageing mice, leading to BBB impairment, is consistent with several studies discussed here.

No age-dependent dysregulation of other key components of the TJ such as the other claudins, ZOs and cytoplasmic plaque proteins associated with TJ complex was seen in this study. Furthermore, the study shows that there is no change in the expression of the major constituents of the key structural components of the BBB, such as the AJ proteins, actin binding proteins, adaptor proteins and basement membrane proteins. Since the upregulation of inflammatory pathways involving cytokines, TNF-α and NF-κB are known to disrupt the assembly of TJ complex, a possible explanation for impaired BBB integrity may be inflammation-mediated breakdown of the TJ complex. Collectively, they suggest a possible mechanism of age-dependent increase in inflammatory pathways that may be associated with the downregulation and/or degradation of proteins of the TJ complex, leading to compromised vascular integrity.

Itm2a is an endothelial-specific, one of the highly expressed transcripts in cerebral ECs. In this study, we observe an age-dependent downregulation of *Itm2a* gene, encoding the integral membrane protein 2A, with log2-fold change values of – 0.64 in 18 months-old males. Linear regression analysis also suggests an age-dependent downregulation of *Itm2a*. However, the role and function of integral membrane protein 2A in human or murine endothelial cells has not been well characterized and any effect of dysregulation of *Itm2a* on BBB needs to be investigated.

4.6 Apelin receptor is strongly downregulated in cerebral ECs with age.

This study showed that *Aplnr* gene, encoding the apelin receptor, showed a strong, progressive, downregulation with log2-fold change values of – 3.18, – 4.10, – 4.51 and – 5.24 (adjusted p-values < 0.001) in 6, 12, 18 and 24 months-old male mice, respectively – as compared to 2 months-old mice. The linear regression analysis confirmed the age-dependent progressive downregulation of *Aplnr*, one of the most strongly downregulated genes in this study. Although the reduction in the expression of apelin receptor with age in various tissues of mice have been demonstrated (Rai et al. 2017)[160], this is the first study where age-dependent downregulation of *Aplnr* in ECs has been shown. Furthermore, western blot analysis also confirmed reduced expression of apelin receptor protein in the brain lysates of aged mice (18 months-old) as compared to the younger mice (2 months-old).

The result is very significant as apelin receptor is known to play a crucial role in positive regulation of vasodilation by heterodimerizing with angiotensin II type 1 receptor (AT1R) leading to its inhibition, thereby negatively regulating the renin-angiotensin system and promoting vasodilation[155, 156]. In their study, Rai et al. (2017) established the negative regulation of blood pressure by apelin receptor. They demonstrated that *Aplnr*$^{-/-}$ mice have normal blood pressure at birth, which starts to rise around 9 months and develop hypertension by the age of 12 months. In human patients, apelin/apelin receptor system has been implicated in vascular health, patients suffering from cardiovascular diseases exhibiting reduced levels of apelin in tissues and circulating blood[159]. Rai et al. (2017) also demonstrated the association of ageing with the downregulation of apelinergic axis as *Apln*$^{-/-}$ and *Aplnr*$^{-/-}$ mice show pathological signs of accelerated ageing. *In vitro* studies have established the role of apelin receptor in regulating biomechanical and morphological properties of ECs. Apelin receptor is located at the cellular junctions and its activation regulates signaling pathways that mediate adaptation of ECs to the flow conditions by modulating EC morphology, elasticity, adhesion and spreading[161].

It has been established that the blood pressure increases with age in both male and female mice, reflecting the pattern observed in humans[205]. Also, hypertension is an established major risk factor of ICH in humans. These studies suggest that the age-dependent downregulation of *Aplnr* in the cerebral ECs may lead to the activation of the RAAS and inhibition of vasodilation, resulting in increased blood pressure in the capillaries.

Furthermore, since apelin receptor has been associated with the maintenance of elasticity, adhesion and EC morphology in response to the flow conditions, altered blood pressure and reduced expression of apelin receptor may be the possible explanation of age-dependent endothelial dysfunction, and BBB impairment with age.

The activity of SRF/MRTF is known to be regulated by mechanical stress-mediated changes in actin dynamics. Age-dependent alteration in the blood pressure may induce changes in the actin cytoskeleton as a consequence of mechanosensing and regulate the SRF/MRTF signaling pathway in the cerebral ECs. However, the effect of altered blood pressure on actin cytoskeleton dynamics and SRF activity in the cerebral ECs need to be investigated.

4.7 *Htra1* gene is downregulated in ECs with age.

Cerebral autosomal recessive arteriopathy with subcortical infarcts and leukoencephalopathy (CARASIL) is an extremely rare autosomal-recessive disease with the symptoms getting progressively worse with age. These patients suffer from stroke before the age of 40 and the incidence of strokes increases progressively, with some patients developing intracerebral hemorrhage[135, 136]. CARASIL has been associated with loss of function mutations in high-temperature requirement-A serine peptidase gene (*HTRA1)*, encoding a serine protease. Interestingly, this study reveals age-dependent downregulation of *Htra1* gene in the 18 and 24 months-old males with log2-fold change values of – 1.5 and – 1.31 in 18 and 24 months-old males, respectively, indicating approximately 3-fold downregulation in the expression of *Htra1* in the cerebral ECs of old male mice. Linear regression analysis also corroborated an age-dependent downregulation of *Htra1* in the cerebral ECs.

Htra1 is known to regulate TGF-β signaling, which is necessary for maintenance of vascular integrity. However, the mechanism of *Htra1* regulating the TGF-β signaling pathway is controversial. While studies by Graham et al. (2013) and Shiga et al. (2011) have demonstrated that Htra1 negatively regulates TGF-β signaling pathway[206, 207], the study by Beaufort et al. showed the activation of TGF-β signaling pathway by *Htra1*[208]. Also, there is no unanimity on the mechanism by which HTRA1 acts on the TGF-β pathway. The different proposed mechanisms for antagonization of TGF-β signaling pathway by HTRA1 include HTRA1-mediated cleavage of TGF-β molecule and HTRA1-mediated cleavage of TGF-β receptor, whereas the proposed mechanism for activation of TGF-β signaling pathway by

HTRA1 involves cleaving latent TGF-β binding protein 1 (LTBP-1) – an extracellular matrix protein – to increase the bioavailability of TGF-β.

The detailed molecular pathways underlying *HTRA1* mutation and the role of HTRA1 in development of CARASIL in human patients is not known. In the study where we observe age-dependent downregulation of *Htra1*, it may be possible that HTRA1-mediated dysregulation of TGF-β signaling pathway could lead to vascular impairment in the central nervous system. However, the detailed mechanisms elucidating the association between HTRA1 and TGF-β in cerebral ECs, and the impact of *Htra1* downregulation on the maintenance of BBB needs to be investigated.

Htra1 is one of the 46 SRF-target genes that has been found to be downregulated with age in our RNA-seq dataset. Since loss of function mutation in *HTRA1* gene is associated with the development of CARASIL, age-dependent downregulation of *Htra1* in the cerebral ECs may be due to altered activity levels of SRF.

4.8 Genes involved in cerebral amyloid angiopathy are not dysregulated with age in the cerebral ECs.

In addition to ageing and hypertension, cerebral amyloid angiopathy (CAA) is another significant risk factor for the development of ICH in humans, with ~ 30 % of all incidences of ICH being attributed to CAA[3]. It is characterized by the deposition of Amyloid-beta (Aβ) plaques in the walls of small vessels, leading to the degeneration of the vasculature, resulting in the formation of microaneurysms and microhemorrhages[10]. In human patients, loss of function mutation in *APP, BRI2, CST3, TTR* and *GSN* genes have been implicated in development of cerebral amyloid angiopathy[120-124].

In this study, *Ttr* was found to be highly expressed in the ECs and significantly downregulated in ECs isolated from 18 months-old mice, with a log2-fold change of – 1.36 in males and – 2.23 in females. However, *Ttr* was not found to be dysregulated in ECs isolated from 24 months. Also, linear regression analysis did not suggest any age-dependent downregulation of *Ttr*. TTR forms a tetrameric complex and binds to the amyloid precursor protein, thus inhibiting the aggregation of amyloid-β in cerebral vasculature. In humans, mutation in *TTR* gene hampers the binding of the amyloid precursor protein with TTR, leading to the aggregation of amyloid- β in the vasculature. Also, Choi et al. (2007) have shown that

mice having only one copy of *Ttr* exhibit an increased amyloid-β levels in both brain and plasma, in comparison to mice having two copies of *Ttr*[209]. These studies have suggested that transthyretin may be associated with the clearance of amyloid-β in both mice and humans.

Other genes implicated in CAA pathology such as *App, Bri2, Cst3* and *Gsn* were not found to be dysregulated with age in mice in this study. The reduced expression of *Ttr* with advancement of age, as observed in this study, may contribute towards impaired amyloid-β in the brains and vasculature, increasing the risk for BBB breakdown.

4.9 CpG methylation levels in cerebral ECs remain stable with age.

This study investigated age-dependent changes in CpG methylation levels in the ECs isolated from the brains of 2, 6, 12 and 18 months-old mice. While ageing leads to a decrease in global methylation levels, specific regions are found to be hypermethylated or hypomethylated with age[171]. In this study, no significant change in global methylation levels were observed in the cerebral ECs isolated from 2, 6 and 12 months-old mice. However, cerebral ECs from 18 months-old mice, showed a subtle (~2%) but significant increase in global methylation levels, indicating an increase in global methylation levels. The observation is consistent with recent age-associated methylation studies in the central nervous system of mice. Hadad et al. (2019) showed that global methylation levels remain stable with age in hippocampus[210]. Earlier, Wagner et al. (2015) had reported that methylation levels in cerebrum of adult mice brain does not change with age, with a subtle increase in the methylation levels observed in the 18 months-old mice. Also, the methylation levels in the human brain was observed to be stable with age[211].

In the study, differentially methylated regions (DMRs) were investigated in continuous, non-overlapping 1000 bp tiles and linear regression analysis was performed to study age-dependent changes in methylation levels in the tiles. Age-dependent differential methylation level was observed in only two tiles, which were annotated to the intronic regions of *Arid5b* and *Adgrg1* genes. These two tiles show a significant age-dependent decrease in methylation. However, no age-dependent dysregulation of Arid5b and Adgrg1 expression was observed in the RNA-seq dataset. Collectively, the data does not suggest any relation between the changes in methylation levels and gene expression levels in the cerebral ECs. This study agrees with the findings of Hadad et al. (2019), who demonstrated that there was

no relationship between age-dependent changes in gene expression and changes in methylation levels in hippocampus of mice. Interestingly, they found that the age-dependent differential gene expression was associated with the level of methylation in young mice. Higher levels of methylation in the promoters and gene bodies of younger mice were associated with increased gene expression with age, while the regions with low level of methylation in young mice showed reduced gene expression with advancement in age[210]. Whether age-dependent changes in gene expression in cerebral ECs can also be explained by the methylation levels established at a young age needs to be further investigated. The further bioinformatic analysis of methylation data may provide more insights in the relationship between methylation levels and age-dependent differential gene expression in the cerebral ECs.

4.10 ATAC-seq reveals changes in chromatin accessibility with age.

Several studies have demonstrated that chromatin accessibility changes with age across species and cell types. The epigenetic changes at the chromatin level have been widely associated with the regulation of gene expression[212]. To study the regulation of gene expression by the changes at chromatin level, ATAC-seq was used to investigate changes in the chromatin accessibility in the cerebral ECs isolated from 2, 6, 12 and 18 months-old mice. The study revealed 2290 peaks which showed change in chromatin structure with ageing, of which 2013 peaks exhibit a decrease in chromatin accessibility with age, suggesting that the majority of chromatin regions change from ‘open’ in younger age-groups to ‘closed’ in the older mice. An interesting observation was that the peaks in cluster 1 show an increased chromatin accessibility before becoming ‘closed’ at the age of 12 and 18 months. Similarly, the peaks belonging to cluster 2 show a reduced chromatin accessibility before ‘opening’ at 12 and 18 months (Figure 3.30 A). A likely explanation of the observation may be that the patterns of chromatin structure in the cerebral ECs may still be getting established till the age of 6 months and any effect of ageing starts after that.

The study compared the RNA-seq and ATAC-seq datasets to find the association between peaks that exhibit differential chromatin accessibility with age and genes that are differentially regulated with age. Among the peaks which show a reduced chromatin accessibility with age, 22 peaks mapped to 20 genes that are significantly downregulated with age. These genes include *Gnb4*, *Serpine2*, *Casp8*, *Aplnr*, *Cacna1e*, *Pdia6*, *Tspan13*, *St3gal6*,

Tyw1, *Tsn*, *Arhgap28*, *Tmsb10*, *Prnp*, *Ptprd*, *Zwint*, *Klhl6*, *Rgl1*, *Pcca* and *Lrrfip1*. The age-dependent downregulation of *Aplnr* at transcript and protein levels, as observed in the RNA-seq and western blot studies, respectively, becomes significant given that the peak mapped to *Aplnr* was annotated as its promoter and reduced chromatin accessibility at the promoter region is associated with reduced transcription.

Also, the study observed age-dependent increase in chromatin accessibility in 5 peaks, which mapped to 5 genes that are upregulated with age, namely – *Arrdc3*, *Zc3h12b*, *Cdk14*, *Chd9* and *Ric3*. Further analysis of the ATAC-seq data to study the age-dependent changes in chromatin structure and the relationship between chromatin accessibility and regulation of gene expression in cerebral ECs is still in progress and is expected to improve our understanding.

4.11 Future perspectives

The main aim of the study was to understand the molecular mechanisms that contribute towards increased cerebral bleedings in aging mice and to gain insights into the basic mechanisms underlying intracerebral hemorrhage in human patients, which may have important clinical and therapeutic implications.

The study was based on the hypothesis that the increase in the incidents of bleedings in the brains of normally aged mice may be due to the age-dependent downregulation of *Srf/Mrtf* function, the dysregulation of SRF/MRTF target genes. Although RNA-seq data did not indicate any dysregulation in the expression of *Srf* and *Mrtf* genes, unchanged transcript levels do not necessarily correlate with reduced protein levels or protein activity. It would be interesting to study the changes in expression levels of SRF and MRTF proteins in the cerebral ECs with age. To characterize the SRF target genes that are dysregulated with age in cerebral ECs, this study compared the dysregulated genes with the list of ~1000 known SRF target genes identified in the cultured NIH3T3 cells by Esnault et al. (2014)[164]. Since there could be cerebral EC-specific SRF target genes which we do not know about, it would be worthwhile to characterize SRF target genes that are specific to cerebral endothelial cells. It would be of particular interest to investigate if the genes encoding proteins that form structural components of the BBB and responsible for its maintenance are SRF target genes.

A novel finding of this study was strong, age-dependent downregulation of the *Aplnr* gene, encoding the apelin receptor. The brain lysates obtained from 18 months-old mice also showed reduced expression of apelin receptor protein as compared to the younger 2 months-old mice, indicating reduced level of apelin receptor protein in the ageing mouse brain. Rai et al. (2017) showed that apelin receptor negatively regulates blood pressure in mice. They found that *Aplnr*$^{-/-}$ mice had normal blood pressure at birth, which started to rise around 9 months and developed into hypertension when mice attained the age of 12 months. They also demonstrated the association of ageing with the downregulation of apelinergic axis as *Apln*$^{-/-}$ and *Aplnr*$^{-/-}$ mice showed pathological signs of accelerated ageing. Infusion of apelin ameliorated age-associated organ impairments and reduced age-associated cardiovascular pathologies in old mice[160]. Our results, along with the study by Rai et al. (2017), suggest an important role of apelinergic axis in ageing and age-associated diseases, specifically, diseases involving the vascular system. The neuroprotective role of apelin in protecting the brain from BBB damage and ischemic stroke is already well known[157, 213].

This study also showed an age-dependent reduction in chromatin accessibility at the promoter region of *Aplnr* gene, suggesting that the reduced chromatin accessibility of the promoter region associated with *Aplnr* gene could be the reason for the downregulation of *Aplnr*. The RRBS study didn't find age-dependent changes in the CpG methylation levels associated with any genomic region annotated to the *Aplnr* gene, indicating that other epigenetic modifications could be regulating the expression of *Aplnr*. These epigenetic changes could most likely include histone modifications that repress transcription, such as deacetylation, methylation and ubiquitylation. Understanding the epigenetic changes that lead to the age-dependent reduction in chromatin accessibility of *Aplnr* promoter and subsequent downregulation will provide more insight into age-associated downregulation of apelin receptor. Also, pharmacological restoration of the apelinergic axis functionality could reverse the effects of ageing and provide a protection from age-associated intracerebral hemorrhage.

5. Bibliography

1. Feigin VL, Lawes CM, Bennett DA, Barker-Collo SL, Parag V. Worldwide stroke incidence and early case fatality reported in 56 population-based studies: A systematic review. *The Lancet. Neurology*. 2009;8:355-369

2. Feigin VL, Krishnamurthi RV, Parmar P, Norrving B, Mensah GA, Bennett DA, et al. Update on the global burden of ischemic and hemorrhagic stroke in 1990-2013: The gbd 2013 study. *Neuroepidemiology*. 2015;45:161-176

3. Elliott J, Smith M. The acute management of intracerebral hemorrhage: A clinical review. *Anesthesia and analgesia*. 2010;110:1419-1427

4. van Asch CJ, Luitse MJ, Rinkel GJ, van der Tweel I, Algra A, Klijn CJ. Incidence, case fatality, and functional outcome of intracerebral haemorrhage over time, according to age, sex, and ethnic origin: A systematic review and meta-analysis. *The Lancet. Neurology*. 2010;9:167-176

5. Jolink WM, Klijn CJ, Brouwers PJ, Kappelle LJ, Vaartjes I. Time trends in incidence, case fatality, and mortality of intracerebral hemorrhage. *Neurology*. 2015;85:1318-1324

6. Matsukawa H, Shinoda M, Fujii M, Takahashi O, Yamamoto D, Murakata A, et al. Factors associated with lobar vs. Non-lobar intracerebral hemorrhage. *Acta neurologica Scandinavica*. 2012;126:116-121

7. Woo D, Broderick JP. Spontaneous intracerebral hemorrhage: Epidemiology and clinical presentation. *Neurosurgery clinics of North America*. 2002;13:265-279, v

8. Harvey A, Montezano AC, Touyz RM. Vascular biology of ageing-implications in hypertension. *Journal of molecular and cellular cardiology*. 2015;83:112-121

9. Fisher CM. Pathological observations in hypertensive cerebral hemorrhage. *Journal of neuropathology and experimental neurology*. 1971;30:536-550

10. Viswanathan A, Greenberg SM. Cerebral amyloid angiopathy in the elderly. *Annals of neurology*. 2011;70:871-880

11. Aronowski J, Zhao X. Molecular pathophysiology of cerebral hemorrhage: Secondary brain injury. *Stroke*. 2011;42:1781-1786

12. Broderick JP, Diringer MN, Hill MD, Brun NC, Mayer SA, Steiner T, et al. Determinants of intracerebral hemorrhage growth: An exploratory analysis. *Stroke*. 2007;38:1072-1075

13. Brott T, Broderick J, Kothari R, Barsan W, Tomsick T, Sauerbeck L, et al. Early hemorrhage growth in patients with intracerebral hemorrhage. *Stroke*. 1997;28:1-5

14. Feigin VL, Norrving B, George MG, Foltz JL, Roth GA, Mensah GA. Prevention of stroke: A strategic global imperative. *Nature reviews. Neurology*. 2016;12:501-512

15. Xi G, Keep RF, Hoff JT. Mechanisms of brain injury after intracerebral haemorrhage. *The Lancet. Neurology*. 2006;5:53-63

16. Wagner KR, Sharp FR, Ardizzone TD, Lu A, Clark JF. Heme and iron metabolism: Role in cerebral hemorrhage. *J Cereb Blood Flow Metab*. 2003;23:629-652

17. Qureshi AI, Ali Z, Suri MF, Shuaib A, Baker G, Todd K, et al. Extracellular glutamate and other amino acids in experimental intracerebral hemorrhage: An in vivo microdialysis study. *Critical care medicine*. 2003;31:1482-1489

18. Steiner T, Kaste M, Forsting M, Mendelow D, Kwiecinski H, Szikora I, et al. Recommendations for the management of intracranial haemorrhage - part i: Spontaneous intracerebral haemorrhage. The european stroke initiative writing committee and the writing committee for the eusi executive committee. *Cerebrovascular diseases (Basel, Switzerland)*. 2006;22:294-316

19. Goldstein LB, Simel DL. Is this patient having a stroke? *Jama*. 2005;293:2391-2402

20. Panagos PD, Jauch EC, Broderick JP. Intracerebral hemorrhage. *Emergency medicine clinics of North America*. 2002;20:631-655

21. Murai Y, Ikeda Y, Teramoto A, Goldstein JN, Greenberg SM, Smith EE, et al. Contrast extravasation on ct angiography predicts hematoma expansion in intracerebral hemorrhage. *Neurology*. 2007;69:617; author reply 617

22. Kidwell CS, Chalela JA, Saver JL, Starkman S, Hill MD, Demchuk AM, et al. Comparison of mri and ct for detection of acute intracerebral hemorrhage. *Jama*. 2004;292:1823-1830

23. Zhu XL, Chan MS, Poon WS. Spontaneous intracranial hemorrhage: Which patients need diagnostic cerebral angiography? A prospective study of 206 cases and review of the literature. *Stroke*. 1997;28:1406-1409

24. Gujjar AR, Deibert E, Manno EM, Duff S, Diringer MN. Mechanical ventilation for ischemic stroke and intracerebral hemorrhage: Indications, timing, and outcome. *Neurology*. 1998;51:447-451

25. Liu Q, Hu T, He L, Huang X, Tian X, Zhang H, et al. Genetic targeting of sprouting angiogenesis using apln-creer. *Nature communications*. 2015;6:6020

26. Broderick J, Connolly S, Feldmann E, Hanley D, Kase C, Krieger D, et al. Guidelines for the management of spontaneous intracerebral hemorrhage in adults: 2007 update: A guideline from the american heart association/american stroke association stroke council, high blood pressure research council, and the quality of care and outcomes in research interdisciplinary working group. *Circulation*. 2007;116:e391-413

27. Aguilar MI, Hart RG, Kase CS, Freeman WD, Hoeben BJ, Garcia RC, et al. Treatment of warfarin-associated intracerebral hemorrhage: Literature review and expert opinion. *Mayo Clinic proceedings*. 2007;82:82-92

28. Appelboam R, Thomas EO. The headache over warfarin in british neurosurgical intensive care units: A national survey of current practice. *Intensive care medicine*. 2007;33:1946-1953

29. Goldstein JN, Rosand J, Schwamm LH. Warfarin reversal in anticoagulant-associated intracerebral hemorrhage. *Neurocritical care*. 2008;9:277-283

30. Morgenstern LB, Hemphill JC, 3rd, Anderson C, Becker K, Broderick JP, Connolly ES, Jr., et al. Guidelines for the management of spontaneous intracerebral hemorrhage: A guideline for healthcare professionals from the american heart association/american stroke association. *Stroke*. 2010;41:2108-2129

31. Mendelow AD, Gregson BA, Fernandes HM, Murray GD, Teasdale GM, Hope DT, et al. Early surgery versus initial conservative treatment in patients with spontaneous supratentorial intracerebral haematomas in the international surgical trial in intracerebral haemorrhage (stich): A randomised trial. *Lancet (London, England)*. 2005;365:387-397

32. Hyder F, Rothman DL, Bennett MR. Cortical energy demands of signaling and nonsignaling components in brain are conserved across mammalian species and activity levels. *Proc Natl Acad Sci U S A*. 2013;110:3549-3554

33. Iadecola C. The neurovascular unit coming of age: A journey through neurovascular coupling in health and disease. *Neuron*. 2017;96:17-42

34. Obermeier B, Daneman R, Ransohoff RM. Development, maintenance and disruption of the blood-brain barrier. *Nature medicine*. 2013;19:1584-1596

35. Montagne A, Zhao Z, Zlokovic BV. Alzheimer's disease: A matter of blood-brain barrier dysfunction? *The Journal of experimental medicine*. 2017;214:3151-3169

36. Sweeney MD, Ayyadurai S, Zlokovic BV. Pericytes of the neurovascular unit: Key functions and signaling pathways. *Nature neuroscience*. 2016;19:771-783

37. Abbott NJ, Ronnback L, Hansson E. Astrocyte-endothelial interactions at the blood-brain barrier. *Nat Rev Neurosci*. 2006;7:41-53

38. Aird WC. Phenotypic heterogeneity of the endothelium: I. Structure, function, and mechanisms. *Circulation research*. 2007;100:158-173

39. Crone C, Christensen O. Electrical resistance of a capillary endothelium. *The Journal of general physiology*. 1981;77:349-371

40. Coomber BL, Stewart PA. Morphometric analysis of cns microvascular endothelium. *Microvascular research*. 1985;30:99-115

41. Henninger DD, Panes J, Eppihimer M, Russell J, Gerritsen M, Anderson DC, et al. Cytokine-induced vcam-1 and icam-1 expression in different organs of the mouse. *Journal of immunology (Baltimore, Md. : 1950)*. 1997;158:1825-1832

42. Betz AL, Firth JA, Goldstein GW. Polarity of the blood-brain barrier: Distribution of enzymes between the luminal and antiluminal membranes of brain capillary endothelial cells. *Brain research*. 1980;192:17-28

43. Betz AL, Goldstein GW. Polarity of the blood-brain barrier: Neutral amino acid transport into isolated brain capillaries. *Science (New York, N.Y.)*. 1978;202:225-227

44. Vallon M, Chang J, Zhang H, Kuo CJ. Developmental and pathological angiogenesis in the central nervous system. *Cellular and molecular life sciences : CMLS*. 2014;71:3489-3506

45. Leinenga G, Langton C, Nisbet R, Götz J. Ultrasound treatment of neurological diseases — current and emerging applications. *Nature Reviews Neurology*. 2016;12:161

46. Mittapalli RK, Manda VK, Adkins CE, Geldenhuys WJ, Lockman PR. Exploiting nutrient transporters at the blood-brain barrier to improve brain distribution of small molecules. *Therapeutic delivery*. 2010;1:775-784

47. Abbott NJ, Patabendige AA, Dolman DE, Yusof SR, Begley DJ. Structure and function of the blood-brain barrier. *Neurobiology of disease*. 2010;37:13-25

48. Morris ME, Rodriguez-Cruz V, Felmlee MA. Slc and abc transporters: Expression, localization, and species differences at the blood-brain and the blood-cerebrospinal fluid barriers. *AAPS J*. 2017;19:1317-1331

49. Bazzoni G. Endothelial tight junctions: Permeable barriers of the vessel wall. *Thrombosis and haemostasis*. 2006;95:36-42

50. Prasain N, Stevens T. The actin cytoskeleton in endothelial cell phenotypes. *Microvascular research*. 2009;77:53-63

51. Luissint A-C, Artus C, Glacial F, Ganeshamoorthy K, Couraud P-O. Tight junctions at the blood brain barrier: Physiological architecture and disease-associated dysregulation. *Fluids and barriers of the CNS*. 2012;9:23-23

52. Mineta K, Yamamoto Y, Yamazaki Y, Tanaka H, Tada Y, Saito K, et al. Predicted expansion of the claudin multigene family. *FEBS letters*. 2011;585:606-612

53. Günzel D, Yu ASL. Claudins and the modulation of tight junction permeability. *Physiol Rev*. 2013;93:525-569

54. Heiskala M, Peterson PA, Yang Y. The roles of claudin superfamily proteins in paracellular transport. *Traffic (Copenhagen, Denmark)*. 2001;2:93-98

55. Morita K, Sasaki H, Furuse M, Tsukita S. Endothelial claudin: Claudin-5/tmvcf constitutes tight junction strands in endothelial cells. *The Journal of cell biology*. 1999;147:185-194

56. Nitta T, Hata M, Gotoh S, Seo Y, Sasaki H, Hashimoto N, et al. Size-selective loosening of the blood-brain barrier in claudin-5-deficient mice. *The Journal of cell biology*. 2003;161:653-660

57. Ohtsuki S, Yamaguchi H, Katsukura Y, Asashima T, Terasaki T. Mrna expression levels of tight junction protein genes in mouse brain capillary endothelial cells highly purified by magnetic cell sorting. *Journal of neurochemistry*. 2008;104:147-154

58. Daneman R, Zhou L, Agalliu D, Cahoy JD, Kaushal A, Barres BA. The mouse blood-brain barrier transcriptome: A new resource for understanding the development and function of brain endothelial cells. *PloS one*. 2010;5:e13741

59. Berndt P, Winkler L, Cording J, Breitkreuz-Korff O, Rex A, Dithmer S, et al. Tight junction proteins at the blood–brain barrier: Far more than claudin-5. *Cellular and Molecular Life Sciences*. 2019;76:1987-2002

60. Derada Troletti C, de Goede P, Kamermans A, de Vries HE. Molecular alterations of the blood-brain barrier under inflammatory conditions: The role of endothelial to mesenchymal transition. *Biochimica et biophysica acta*. 2016;1862:452-460

61. Greene C, Kealy J, Humphries MM, Gong Y, Hou J, Hudson N, et al. Dose-dependent expression of claudin-5 is a modifying factor in schizophrenia. *Molecular psychiatry*. 2018;23:2156-2166

62. Furuse M, Hirase T, Itoh M, Nagafuchi A, Yonemura S, Tsukita S, et al. Occludin: A novel integral membrane protein localizing at tight junctions. *The Journal of cell biology*. 1993;123:1777-1788

63. Nusrat A, Brown GT, Tom J, Drake A, Bui TT, Quan C, et al. Multiple protein interactions involving proposed extracellular loop domains of the tight junction protein occludin. *Molecular biology of the cell*. 2005;16:1725-1734

64. Cording J, Berg J, Kading N, Bellmann C, Tscheik C, Westphal JK, et al. In tight junctions, claudins regulate the interactions between occludin, tricellulin and marveld3, which, inversely, modulate claudin oligomerization. *Journal of cell science*. 2013;126:554-564

65. Stamatovic SM, Johnson AM, Keep RF, Andjelkovic AV. Junctional proteins of the blood-brain barrier: New insights into function and dysfunction. *Tissue barriers*. 2016;4:e1154641

66. Williams LA, Martin-Padura I, Dejana E, Hogg N, Simmons DL. Identification and characterisation of human junctional adhesion molecule (jam). *Molecular immunology*. 1999;36:1175-1188

67. Ebnet K, Aurrand-Lions M, Kuhn A, Kiefer F, Butz S, Zander K, et al. The junctional adhesion molecule (jam) family members jam-2 and jam-3 associate with the cell polarity protein par-3: A possible role for jams in endothelial cell polarity. *Journal of cell science*. 2003;116:3879-3891

68. Itoh M, Sasaki H, Furuse M, Ozaki H, Kita T, Tsukita S. Junctional adhesion molecule (jam) binds to par-3: A possible mechanism for the recruitment of par-3 to tight junctions. *The Journal of cell biology*. 2001;154:491-497

69. Wegmann F, Petri B, Khandoga AG, Moser C, Khandoga A, Volkery S, et al. Esam supports neutrophil extravasation, activation of rho, and vegf-induced vascular permeability. *The Journal of experimental medicine*. 2006;203:1671-1677

70. Stamatovic SM, Keep RF, Andjelkovic AV. Brain endothelial cell-cell junctions: How to "open" the blood brain barrier. *Current neuropharmacology*. 2008;6:179-192

71. Gonzalez-Mariscal L, Betanzos A, Nava P, Jaramillo BE. Tight junction proteins. *Progress in biophysics and molecular biology*. 2003;81:1-44

72. McNeil E, Capaldo CT, Macara IG. Zonula occludens-1 function in the assembly of tight junctions in madin-darby canine kidney epithelial cells. *Molecular biology of the cell*. 2006;17:1922-1932

73. Gonzalez-Mariscal L, Betanzos A, Avila-Flores A. Maguk proteins: Structure and role in the tight junction. *Seminars in cell & developmental biology*. 2000;11:315-324

74. Daneman R, Prat A. The blood-brain barrier. *Cold Spring Harbor perspectives in biology*. 2015;7:a020412

75. Van Itallie CM, Anderson JM. Claudin interactions in and out of the tight junction. *Tissue barriers*. 2013;1:e25247

76. Itoh M, Furuse M, Morita K, Kubota K, Saitou M, Tsukita S. Direct binding of three tight junction-associated maguks, zo-1, zo-2, and zo-3, with the cooh termini of claudins. *The Journal of cell biology*. 1999;147:1351-1363

77. Utepbergenov DI, Fanning AS, Anderson JM. Dimerization of the scaffolding protein zo-1 through the second pdz domain. *The Journal of biological chemistry*. 2006;281:24671-24677

78. Tornavaca O, Chia M, Dufton N, Almagro LO, Conway DE, Randi AM, et al. Zo-1 controls endothelial adherens junctions, cell-cell tension, angiogenesis, and barrier formation. *The Journal of cell biology*. 2015;208:821-838

79. Beatch M, Jesaitis LA, Gallin WJ, Goodenough DA, Stevenson BR. The tight junction protein zo-2 contains three pdz (psd-95/discs-large/zo-1) domains and an alternatively spliced region. *The Journal of biological chemistry*. 1996;271:25723-25726

80. Cordenonsi M, D'Atri F, Hammar E, Parry DA, Kendrick-Jones J, Shore D, et al. Cingulin contains globular and coiled-coil domains and interacts with zo-1, zo-2, zo-3, and myosin. *The Journal of cell biology*. 1999;147:1569-1582

81. McEwen AE, Escobar DE, Gottardi CJ. Signaling from the adherens junction. *Subcell Biochem*. 2012;60:171-196

82. Abbruscato TJ, Davis TP. Protein expression of brain endothelial cell e-cadherin after hypoxia/aglycemia: Influence of astrocyte contact. *Brain research*. 1999;842:277-286

83. Gory-Faure S, Prandini MH, Pointu H, Roullot V, Pignot-Paintrand I, Vernet M, et al. Role of vascular endothelial-cadherin in vascular morphogenesis. *Development (Cambridge, England)*. 1999;126:2093

84. Crosby CV, Fleming PA, Argraves WS, Corada M, Zanetta L, Dejana E, et al. Ve-cadherin is not required for the formation of nascent blood vessels but acts to prevent their disassembly. *Blood*. 2005;105:2771

85. Carmeliet P, Lampugnani MG, Moons L, Breviario F, Compernolle V, Bono F, et al. Targeted deficiency or cytosolic truncation of the ve-cadherin gene in mice impairs vegf-mediated endothelial survival and angiogenesis. *Cell*. 1999;98:147-157

86. Luo Y, Radice GL. N-cadherin acts upstream of ve-cadherin in controlling vascular morphogenesis. *The Journal of cell biology*. 2005;169:29-34

87. Nagafuchi A. Molecular architecture of adherens junctions. *Current opinion in cell biology*. 2001;13:600-603

88. Lai CH, Kuo KH, Leo JM. Critical role of actin in modulating bbb permeability. *Brain research. Brain research reviews*. 2005;50:7-13

89. Harzheim M, Stepien-Mering M, Schroder R, Schmidt S. The expression of microfilament-associated cell-cell contacts in brain endothelial cells is modified by ifn-beta1a (rebif). *Journal of interferon & cytokine research : the official journal of the International Society for Interferon and Cytokine Research*. 2004;24:711-716

90. Dudek SM, Garcia JG. Cytoskeletal regulation of pulmonary vascular permeability. *Journal of applied physiology (Bethesda, Md. : 1985)*. 2001;91:1487-1500

91. Birukova AA, Birukov KG, Smurova K, Adyshev D, Kaibuchi K, Alieva I, et al. Novel role of microtubules in thrombin-induced endothelial barrier dysfunction. *FASEB journal : official publication of the Federation of American Societies for Experimental Biology*. 2004;18:1879-1890

92. Verin AD, Birukova A, Wang P, Liu F, Becker P, Birukov K, et al. Microtubule disassembly increases endothelial cell barrier dysfunction: Role of mlc phosphorylation. *American journal of physiology. Lung cellular and molecular physiology*. 2001;281:L565-574

93. Van Itallie CM, Tietgens AJ, Krystofiak E, Kachar B, Anderson JM. A complex of zo-1 and the bar-domain protein toca-1 regulates actin assembly at the tight junction. *Molecular biology of the cell*. 2015;26:2769-2787

94. Etienne-Manneville S, Hall A. Rho gtpases in cell biology. *Nature*. 2002;420:629-635

95. Zhong Y, Zhang B, Eum SY, Toborek M. Hiv-1 tat triggers nuclear localization of zo-1 via rho signaling and camp response element-binding protein activation. *The Journal of neuroscience : the official journal of the Society for Neuroscience*. 2012;32:143-150

96. Park M, Kim HJ, Lim B, Wylegala A, Toborek M. Methamphetamine-induced occludin endocytosis is mediated by the arp2/3 complex-regulated actin rearrangement. *The Journal of biological chemistry*. 2013;288:33324-33334

97. Millard TH, Sharp SJ, Machesky LM. Signalling to actin assembly via the wasp (wiskott-aldrich syndrome protein)-family proteins and the arp2/3 complex. *The Biochemical journal*. 2004;380:1-17

98. Thomsen MS, Routhe LJ, Moos T. The vascular basement membrane in the healthy and pathological brain. *Journal of cerebral blood flow and metabolism : official journal of the International Society of Cerebral Blood Flow and Metabolism*. 2017;37:3300-3317

99. Hallmann R, Horn N, Selg M, Wendler O, Pausch F, Sorokin LM. Expression and function of laminins in the embryonic and mature vasculature. *Physiol Rev*. 2005;85:979-1000

100. Chistiakov DA, Orekhov AN, Bobryshev YV. Endothelial barrier and its abnormalities in cardiovascular disease. *Frontiers in physiology*. 2015;6:365

101. Pöschl E, Schlötzer-Schrehardt U, Brachvogel B, Saito K, Ninomiya Y, Mayer U. Collagen iv is essential for basement membrane stability but dispensable for initiation of its assembly during early development. *Development (Cambridge, England)*. 2004;131:1619

102. Gould DB, Phalan FC, Breedveld GJ, van Mil SE, Smith RS, Schimenti JC, et al. Mutations in col4a1 cause perinatal cerebral hemorrhage and porencephaly. *Science (New York, N.Y.)*. 2005;308:1167

103. Jeanne M, Labelle-Dumais C, Jorgensen J, Kauffman WB, Mancini GM, Favor J, et al. Col4a2 mutations impair col4a1 and col4a2 secretion and cause hemorrhagic stroke. *American journal of human genetics*. 2012;90:91-101

104. Gould DB, Phalan FC, van Mil SE, Sundberg JP, Vahedi K, Massin P, et al. Role of col4a1 in small-vessel disease and hemorrhagic stroke. *The New England journal of medicine*. 2006;354:1489-1496

105. Durbeej M. Laminins. *Cell and tissue research*. 2010;339:259-268

106. Xu L, Nirwane A, Yao Y. Basement membrane and blood–brain barrier. *Stroke and Vascular Neurology*. 2019;4:78

107. Thyboll J, Kortesmaa J, Cao R, Soininen R, Wang L, Iivanainen A, et al. Deletion of the laminin alpha4 chain leads to impaired microvessel maturation. *Molecular and cellular biology*. 2002;22:1194-1202

108. Song J, Zhang X, Buscher K, Wang Y, Wang H, Di Russo J, et al. Endothelial basement membrane laminin 511 contributes to endothelial junctional tightness and thereby inhibits leukocyte transmigration. *Cell reports*. 2017;18:1256-1269

109. Dong L, Chen Y, Lewis M, Hsieh JC, Reing J, Chaillet JR, et al. Neurologic defects and selective disruption of basement membranes in mice lacking entactin-1/nidogen-1. *Lab Invest*. 2002;82:1617-1630

110. Bader BL, Smyth N, Nedbal S, Miosge N, Baranowsky A, Mokkapati S, et al. Compound genetic ablation of nidogen 1 and 2 causes basement membrane defects and perinatal lethality in mice. *Molecular and cellular biology*. 2005;25:6846-6856

111. Arikawa-Hirasawa E, Watanabe H, Takami H, Hassell JR, Yamada Y. Perlecan is essential for cartilage and cephalic development. *Nature genetics*. 1999;23:354-358

112. Hynes RO. Integrins: Bidirectional, allosteric signaling machines. *Cell*. 2002;110:673-687

113. Edwards DN, Bix GJ. Roles of blood-brain barrier integrins and extracellular matrix in stroke. *American journal of physiology. Cell physiology*. 2019;316:C252-c263

114. De Arcangelis A, Georges-Labouesse E. Integrin and ecm functions: Roles in vertebrate development. *Trends in genetics : TIG*. 2000;16:389-395

115. Schaffner F, Ray AM, Dontenwill M. Integrin alpha5beta1, the fibronectin receptor, as a pertinent therapeutic target in solid tumors. *Cancers*. 2013;5:27-47

116. Milner R, Campbell IL. Increased expression of the beta4 and alpha5 integrin subunits in cerebral blood vessels of transgenic mice chronically producing the pro-inflammatory cytokines il-6 or ifn-alpha in the central nervous system. *Molecular and cellular neurosciences*. 2006;33:429-440

117. Karschnia P, Nishimura S, Louvi A. Cerebrovascular disorders associated with genetic lesions. *Cellular and molecular life sciences : CMLS*. 2019;76:283-300

118. Joutel A, Corpechot C, Ducros A, Vahedi K, Chabriat H, Mouton P, et al. Notch3 mutations in cadasil, a hereditary adult-onset condition causing stroke and dementia. *Nature*. 1996;383:707-710

119. Hara K, Shiga A, Fukutake T, Nozaki H, Miyashita A, Yokoseki A, et al. Association of htra1 mutations and familial ischemic cerebral small-vessel disease. *The New England journal of medicine*. 2009;360:1729-1739

120. Rovelet-Lecrux A, Hannequin D, Raux G, Le Meur N, Laquerriere A, Vital A, et al. App locus duplication causes autosomal dominant early-onset alzheimer disease with cerebral amyloid angiopathy. *Nature genetics*. 2006;38:24-26

121. Vidal R, Barbeito AG, Miravalle L, Ghetti B. Cerebral amyloid angiopathy and parenchymal amyloid deposition in transgenic mice expressing the danish mutant form of human bri2. *Brain pathology (Zurich, Switzerland)*. 2009;19:58-68

122. Ghiso J, Jensson O, Frangione B. Amyloid fibrils in hereditary cerebral hemorrhage with amyloidosis of icelandic type is a variant of gamma-trace basic protein (cystatin c). *Proc Natl Acad Sci U S A*. 1986;83:2974-2978

123. Brett M, Persey MR, Reilly MM, Revesz T, Booth DR, Booth SE, et al. Transthyretin leu12pro is associated with systemic, neuropathic and leptomeningeal amyloidosis. *Brain : a journal of neurology*. 1999;122 (Pt 2):183-190

124. Ghiso J, Haltia M, Prelli F, Novello J, Frangione B. Gelsolin variant (asn-187) in familial amyloidosis, finnish type. *The Biochemical journal*. 1990;272:827-830

125. Richards A, van den Maagdenberg AM, Jen JC, Kavanagh D, Bertram P, Spitzer D, et al. C-terminal truncations in human 3'-5' DNA exonuclease trex1 cause autosomal dominant retinal vasculopathy with cerebral leukodystrophy. *Nature genetics*. 2007;39:1068-1070

126. Taguchi A, Maruyama H, Nameta M, Yamamoto T, Matsuda J, Kulkarni AB, et al. A symptomatic fabry disease mouse model generated by inducing globotriaosylceramide synthesis. *The Biochemical journal*. 2013;456:373-383

127. Laberge-le Couteulx S, Jung HH, Labauge P, Houtteville JP, Lescoat C, Cecillon M, et al. Truncating mutations in ccm1, encoding krit1, cause hereditary cavernous angiomas. *Nature genetics*. 1999;23:189-193

128. Liquori CL, Berg MJ, Siegel AM, Huang E, Zawistowski JS, Stoffer T, et al. Mutations in a gene encoding a novel protein containing a phosphotyrosine-binding domain cause type 2 cerebral cavernous malformations. *American journal of human genetics*. 2003;73:1459-1464

129. Bergametti F, Denier C, Labauge P, Arnoult M, Boetto S, Clanet M, et al. Mutations within the programmed cell death 10 gene cause cerebral cavernous malformations. *American journal of human genetics*. 2005;76:42-51

130. Bilguvar K, Yasuno K, Niemela M, Ruigrok YM, von Und Zu Fraunberg M, van Duijn CM, et al. Susceptibility loci for intracranial aneurysm in european and japanese populations. *Nature genetics*. 2008;40:1472-1477

131. Yasuno K, Bilguvar K, Bijlenga P, Low SK, Krischek B, Auburger G, et al. Genome-wide association study of intracranial aneurysm identifies three new risk loci. *Nature genetics*. 2010;42:420-425

132. Yasuno K, Bakircioglu M, Low SK, Bilguvar K, Gaal E, Ruigrok YM, et al. Common variant near the endothelin receptor type a (ednra) gene is associated with intracranial aneurysm risk. *Proc Natl Acad Sci U S A*. 2011;108:19707-19712

133. Papakonstantinou E, Bacopoulou F, Brouzas D, Megalooikonomou V, D'Elia D, Bongcam-Rudloff E, et al. Notch3 and cadasil syndrome: A genetic and structural overview. *EMBnet.journal*. 2019;24

134. Chabriat H, Joutel A, Dichgans M, Tournier-Lasserve E, Bousser MG. Cadasil. *The Lancet. Neurology*. 2009;8:643-653

135. Onodera O, Nozaki H, Fukutake T. Carasil. In: Adam MP, Ardinger HH, Pagon RA, Wallace SE, Bean LJH, Stephens K, et al., eds. *Genereviews((r))*. Seattle (WA): University of Washington, Seattle
University of Washington, Seattle. GeneReviews is a registered trademark of the University of Washington, Seattle. All rights reserved.; 1993.

136. Menezes Cordeiro I, Nzwalo H, Sa F, Ferreira RB, Alonso I, Afonso L, et al. Shifting the carasil paradigm: Report of a non-asian family and literature review. *Stroke*. 2015;46:1110-1112

137. McCormick WF. The pathology of vascular ("arteriovenous") malformations. *Journal of neurosurgery*. 1966;24:807-816

138. Boulday G, Blecon A, Petit N, Chareyre F, Garcia LA, Niwa-Kawakita M, et al. Tissue-specific conditional ccm2 knockout mice establish the essential role of endothelial ccm2 in angiogenesis: Implications for human cerebral cavernous malformations. *Disease models & mechanisms*. 2009;2:168-177

139. Chan AC, Drakos SG, Ruiz OE, Smith AC, Gibson CC, Ling J, et al. Mutations in 2 distinct genetic pathways result in cerebral cavernous malformations in mice. *The Journal of clinical investigation*. 2011;121:1871-1881

140. Cunningham K, Uchida Y, O'Donnell E, Claudio E, Li W, Soneji K, et al. Conditional deletion of ccm2 causes hemorrhage in the adult brain: A mouse model of human cerebral cavernous malformations. *Human molecular genetics*. 2011;20:3198-3206

141. Baranoski JF, Kalani MY, Przybylowski CJ, Zabramski JM. Cerebral cavernous malformations: Review of the genetic and protein-protein interactions resulting in disease pathogenesis. *Frontiers in surgery*. 2016;3:60

142. Hilder TL, Malone MH, Bencharit S, Colicelli J, Haystead TA, Johnson GL, et al. Proteomic identification of the cerebral cavernous malformation signaling complex. *Journal of proteome research*. 2007;6:4343-4355

143. Lakatta EG. The reality of aging viewed from the arterial wall. *Artery research*. 2013;7:73-80

144. Alam MU, Kirton JP, Wilkinson FL, Towers E, Sinha S, Rouhi M, et al. Calcification is associated with loss of functional calcium-sensing receptor in vascular smooth muscle cells. *Cardiovascular research*. 2009;81:260-268

145. McCarty MF, DiNicolantonio JJ. The molecular biology and pathophysiology of vascular calcification. *Postgraduate medicine*. 2014;126:54-64

146. Sindler AL, Delp MD, Reyes R, Wu G, Muller-Delp JM. Effects of ageing and exercise training on enos uncoupling in skeletal muscle resistance arterioles. *The Journal of physiology*. 2009;587:3885-3897

147. Sack MN, Finkel T. Mitochondrial metabolism, sirtuins, and aging. *Cold Spring Harbor perspectives in biology*. 2012;4

148. Hafner AV, Dai J, Gomes AP, Xiao CY, Palmeira CM, Rosenzweig A, et al. Regulation of the mptp by sirt3-mediated deacetylation of cypd at lysine 166 suppresses age-related cardiac hypertrophy. *Aging*. 2010;2:914-923

149. Stamatovic SM, Martinez-Revollar G, Hu A, Choi J, Keep RF, Andjelkovic AV. Decline in sirtuin-1 expression and activity plays a critical role in blood-brain barrier permeability in aging. *Neurobiology of disease*. 2019;126:105-116

150. Chung HY, Cesari M, Anton S, Marzetti E, Giovannini S, Seo AY, et al. Molecular inflammation: Underpinnings of aging and age-related diseases. *Ageing Res Rev*. 2009;8:18-30

151. Montezano AC, Touyz RM. Reactive oxygen species, vascular noxs, and hypertension: Focus on translational and clinical research. *Antioxid Redox Signal*. 2014;20:164-182

152. Fan Q, Chen L, Cheng S, Li F, Lau WB, Wang LF, et al. Aging aggravates nitrate-mediated ros/rns changes. *Oxid Med Cell Longev*. 2014;2014:376515-376515

153. Kokoszka JE, Coskun P, Esposito LA, Wallace DC. Increased mitochondrial oxidative stress in the sod2 (+/-) mouse results in the age-related decline of mitochondrial function culminating in increased apoptosis. *Proceedings of the National Academy of Sciences of the United States of America*. 2001;98:2278-2283

154. Yoon HE, Kim EN, Kim MY, Lim JH, Jang I-A, Ban TH, et al. Age-associated changes in the vascular renin-angiotensin system in mice. *Oxid Med Cell Longev*. 2016;2016:6731093-6731093

155. Siddiquee K, Hampton J, McAnally D, May L, Smith L. The apelin receptor inhibits the angiotensin ii type 1 receptor via allosteric trans-inhibition. *British journal of pharmacology*. 2013;168:1104-1117

156. Wu D, He L, Chen L. Apelin/apj system: A promising therapy target for hypertension. *Molecular biology reports*. 2014;41:6691-6703

157. Chu H, Yang X, Huang C, Gao Z, Tang Y, Dong Q. Apelin-13 protects against ischemic blood-brain barrier damage through the effects of aquaporin-4. *Cerebrovascular diseases (Basel, Switzerland)*. 2017;44:10-25

158. Hwangbo C, Wu J, Papangeli I, Adachi T, Sharma B, Park S, et al. Endothelial aplnr regulates tissue fatty acid uptake and is essential for apelin's glucose-lowering effects. *Science translational medicine*. 2017;9

159. Mughal A, O'Rourke ST. Vascular effects of apelin: Mechanisms and therapeutic potential. *Pharmacology & therapeutics*. 2018;190:139-147

160. Rai R, Ghosh AK, Eren M, Mackie AR, Levine DC, Kim SY, et al. Downregulation of the apelinergic axis accelerates aging, whereas its systemic restoration improves the mammalian healthspan. *Cell reports*. 2017;21:1471-1480

161. Strohbach A, Pennewitz M, Glaubitz M, Palankar R, Gross S, Lorenz F, et al. The apelin receptor influences biomechanical and morphological properties of endothelial cells. *Journal of cellular physiology*. 2018;233:6250-6261

162. Shore P, Sharrocks AD. The mads-box family of transcription factors. *European journal of biochemistry*. 1995;229:1-13

163. Treisman R. Identification of a protein-binding site that mediates transcriptional response of the c-fos gene to serum factors. *Cell*. 1986;46:567-574

164. Esnault C, Stewart A, Gualdrini F, East P, Horswell S, Matthews N, et al. Rho-actin signaling to the mrtf coactivators dominates the immediate transcriptional response to serum in fibroblasts. *Genes Dev*. 2014;28:943-958

165. Olson EN, Nordheim A. Linking actin dynamics and gene transcription to drive cellular motile functions. *Nat Rev Mol Cell Biol*. 2010;11:353-365

166. Posern G, Treisman R. Actin' together: Serum response factor, its cofactors and the link to signal transduction. *Trends in cell biology*. 2006;16:588-596

167. Arsenian S, Weinhold B, Oelgeschlager M, Ruther U, Nordheim A. Serum response factor is essential for mesoderm formation during mouse embryogenesis. *The EMBO journal*. 1998;17:6289-6299

168. Miano JM. Role of serum response factor in the pathogenesis of disease. *Lab Invest*. 2010;90:1274-1284

169. Weinl C, Castaneda Vega S, Riehle H, Stritt C, Calaminus C, Wolburg H, et al. Endothelial depletion of murine srf/mrtf provokes intracerebral hemorrhagic stroke. *Proc Natl Acad Sci U S A*. 2015;112:9914-9919

170. Bird A. DNA methylation patterns and epigenetic memory. *Genes Dev*. 2002;16:6-21

171. Xiao FH, Kong QP, Perry B, He YH. Progress on the role of DNA methylation in aging and longevity. *Briefings in functional genomics*. 2016;15:454-459

172. Meissner A, Gnirke A, Bell GW, Ramsahoye B, Lander ES, Jaenisch R. Reduced representation bisulfite sequencing for comparative high-resolution DNA methylation analysis. *Nucleic acids research*. 2005;33:5868-5877

173. Buenrostro JD, Wu B, Chang HY, Greenleaf WJ. Atac-seq: A method for assaying chromatin accessibility genome-wide. *Current protocols in molecular biology*. 2015;109:21.29.21-29

174. Martin M. Cutadapt removes adapter sequences from high-throughput sequencing reads. *2011*. 2011;17:3

175. Dobin A, Davis CA, Schlesinger F, Drenkow J, Zaleski C, Jha S, et al. Star: Ultrafast universal rna-seq aligner. *Bioinformatics (Oxford, England)*. 2013;29:15-21

176. Ewels P, Magnusson M, Lundin S, Käller M. Multiqc: Summarize analysis results for multiple tools and samples in a single report. *Bioinformatics (Oxford, England)*. 2016;32:3047-3048

177. Love MI, Huber W, Anders S. Moderated estimation of fold change and dispersion for rna-seq data with deseq2. *Genome biology*. 2014;15:550

178. Li H, Durbin R. Fast and accurate short read alignment with burrows-wheeler transform. *Bioinformatics (Oxford, England)*. 2009;25:1754-1760

179. Hovestadt V, Jones DT, Picelli S, Wang W, Kool M, Northcott PA, et al. Decoding the regulatory landscape of medulloblastoma using DNA methylation sequencing. *Nature*. 2014;510:537-541

180. Li H, Handsaker B, Wysoker A, Fennell T, Ruan J, Homer N, et al. The sequence alignment/map format and samtools. *Bioinformatics (Oxford, England)*. 2009;25:2078-2079

181. Liu Y, Siegmund KD, Laird PW, Berman BP. Bis-snp: Combined DNA methylation and snp calling for bisulfite-seq data. *Genome biology*. 2012;13:R61

182. Akalin A, Kormaksson M, Li S, Garrett-Bakelman FE, Figueroa ME, Melnick A, et al. Methylkit: A comprehensive r package for the analysis of genome-wide DNA methylation profiles. *Genome biology*. 2012;13:R87

183. Quinlan AR, Hall IM. Bedtools: A flexible suite of utilities for comparing genomic features. *Bioinformatics (Oxford, England)*. 2010;26:841-842

184. Marco-Sola S, Sammeth M, Guigo R, Ribeca P. The gem mapper: Fast, accurate and versatile alignment by filtration. *Nature methods*. 2012;9:1185-1188

185. Zhang Y, Liu T, Meyer CA, Eeckhoute J, Johnson DS, Bernstein BE, et al. Model-based analysis of chip-seq (macs). *Genome biology*. 2008;9:R137

186. Jaric I, Rocks D, Greally JM, Suzuki M, Kundakovic M. Chromatin organization in the female mouse brain fluctuates across the oestrous cycle. *Nature communications*. 2019;10:2851

187. Sergushichev AA. An algorithm for fast preranked gene set enrichment analysis using cumulative statistic calculation. *bioRxiv*. 2016:060012

188. Liberzon A, Birger C, Thorvaldsdóttir H, Ghandi M, Mesirov Jill P, Tamayo P. The molecular signatures database hallmark gene set collection. *Cell Systems*. 2015;1:417-425

189. Ben-Zvi A, Lacoste B, Kur E, Andreone BJ, Mayshar Y, Yan H, et al. Mfsd2a is critical for the formation and function of the blood-brain barrier. *Nature*. 2014;509:507-511

190. Liu S, Grigoryan MM, Vasilevko V, Sumbria RK, Paganini-Hill A, Cribbs DH, et al. Comparative analysis of h&e and prussian blue staining in a mouse model of cerebral microbleeds. *The journal of histochemistry and cytochemistry : official journal of the Histochemistry Society*. 2014;62:767-773

191. Elahy M, Jackaman C, Mamo JC, Lam V, Dhaliwal SS, Giles C, et al. Blood-brain barrier dysfunction developed during normal aging is associated with inflammation and loss of tight junctions but not with leukocyte recruitment. *Immunity & ageing : I & A*. 2015;12:2

192. Yang J, Huang T, Petralia F, Long Q, Zhang B, Argmann C, et al. Synchronized age-related gene expression changes across multiple tissues in human and the link to complex diseases. *Scientific reports*. 2015;5:15145

193. Glass D, Viñuela A, Davies MN, Ramasamy A, Parts L, Knowles D, et al. Gene expression changes with age in skin, adipose tissue, blood and brain. *Genome biology*. 2013;14:R75

194. Somel M, Khaitovich P, Bahn S, Paabo S, Lachmann M. Gene expression becomes heterogeneous with age. *Current biology : CB*. 2006;16:R359-360

195. Hickman SE, Kingery ND, Ohsumi TK, Borowsky ML, Wang LC, Means TK, et al. The microglial sensome revealed by direct rna sequencing. *Nature neuroscience*. 2013;16:1896-1905

196. Benayoun BA, Pollina EA, Singh PP, Mahmoudi S, Harel I, Casey KM, et al. Remodeling of epigenome and transcriptome landscapes with aging in mice reveals widespread induction of inflammatory responses. *Genome Res*. 2019;29:697-709

197. Pierce GL, Lesniewski LA, Lawson BR, Beske SD, Seals DR. Nuclear factor-{kappa}b activation contributes to vascular endothelial dysfunction via oxidative stress in overweight/obese middle-aged and older humans. *Circulation*. 2009;119:1284-1292

198. Csiszar A, Wang M, Lakatta EG, Ungvari Z. Inflammation and endothelial dysfunction during aging: Role of nf-kappab. *Journal of applied physiology (Bethesda, Md. : 1985)*. 2008;105:1333-1341

199. Donato AJ, Black AD, Jablonski KL, Gano LB, Seals DR. Aging is associated with greater nuclear nfκb, reduced iκbα, and increased expression of proinflammatory cytokines in vascular endothelial cells of healthy humans. *Aging Cell*. 2008;7:805-812

200. Fichtlscherer S, Rosenberger G, Walter DH, Breuer S, Dimmeler S, Zeiher AM. Elevated c-reactive protein levels and impaired endothelial vasoreactivity in patients with coronary artery disease. *Circulation*. 2000;102:1000-1006

201. Greene C, Hanley N, Campbell M. Claudin-5: Gatekeeper of neurological function. *Fluids and Barriers of the CNS*. 2019;16:3

202. Hoffman WH, Stamatovic SM, Andjelkovic AV. Inflammatory mediators and blood brain barrier disruption in fatal brain edema of diabetic ketoacidosis. *Brain research*. 2009;1254:138-148

203. Wu B, Ma Q, Khatibi N, Chen W, Sozen T, Cheng O, et al. Ac-yvad-cmk decreases blood-brain barrier degradation by inhibiting caspase-1 activation of interleukin-1beta in intracerebral hemorrhage mouse model. *Translational stroke research*. 2010;1:57-64

204. Krabbe KS, Pedersen M, Bruunsgaard H. Inflammatory mediators in the elderly. *Experimental gerontology*. 2004;39:687-699

205. Barsha G, Denton KM, Mirabito Colafella KM. Sex- and age-related differences in arterial pressure and albuminuria in mice. *Biol Sex Differ*. 2016;7:57-57

206. Graham JR, Chamberland A, Lin Q, Li XJ, Dai D, Zeng W, et al. Serine protease htra1 antagonizes transforming growth factor-β signaling by cleaving its receptors and loss of htra1 in vivo enhances bone formation. *PloS one*. 2013;8:e74094-e74094

207. Shiga A, Nozaki H, Yokoseki A, Nihonmatsu M, Kawata H, Kato T, et al. Cerebral small-vessel disease protein htra1 controls the amount of tgf-beta1 via cleavage of protgf-beta1. *Human molecular genetics*. 2011;20:1800-1810

208. Beaufort N, Scharrer E, Kremmer E, Lux V, Ehrmann M, Huber R, et al. Cerebral small vessel disease-related protease htra1 processes latent tgf-beta binding protein 1 and facilitates tgf-beta signaling. *Proc Natl Acad Sci U S A*. 2014;111:16496-16501

209. Choi SH, Leight SN, Lee VMY, Li T, Wong PC, Johnson JA, et al. Accelerated abeta deposition in appswe/ps1deltae9 mice with hemizygous deletions of ttr (transthyretin). *The Journal of neuroscience : the official journal of the Society for Neuroscience*. 2007;27:7006-7010

210. Hadad N, Masser DR, Blanco-Berdugo L, Stanford DR, Freeman WM. Early-life DNA methylation profiles are indicative of age-related transcriptome changes. *Epigenetics & Chromatin*. 2019;12:58

211. Wagner M, Steinbacher J, Kraus TF, Michalakis S, Hackner B, Pfaffeneder T, et al. Age-dependent levels of 5-methyl-, 5-hydroxymethyl-, and 5-formylcytosine in human and mouse brain tissues. *Angewandte Chemie (International ed. in English)*. 2015;54:12511-12514

212. Benayoun BA, Pollina EA, Brunet A. Epigenetic regulation of ageing: Linking environmental inputs to genomic stability. *Nat Rev Mol Cell Biol*. 2015;16:593-610

213. Yang Y, Zhang X, Cui H, Zhang C, Zhu C, Li L. Apelin-13 protects the brain against ischemia/reperfusion injury through activating pi3k/akt and erk1/2 signaling pathways. *Neuroscience letters*. 2014;568:44-49

Appendices

Appendix A

Contributions

The work presented in this thesis was performed in collaboration with several research groups and following people contributed to the work:

1. Abdulrahman Salhab: performed ATAC-seq data analysis and interpretation.
2. Dr. Gilles Gasparoni: performed the sequencing of RRBS and ATAC-seq libraries prepared by me,
   performed RRBS data analysis and interpretation,
   performed linear regression analysis on RNA-seq data.
3. Dr. Kristin Bieber: performed FACS for the isolation of ECs
4. Dr. Robert Geffers: prepared RNA-seq library from RNA isolated by me,
   performed sequencing and multivariate analysis.
5. Michael Orlich: sacrificed the mice to harvest the organs.
6. Prof. Dr. Jörn Walter: involved in interpretation of RNA-seq, RRBS and ATAC-seq data.

All the remaining work, including writing the thesis, was performed by me.

Appendix B

Abbreviations

ABC	ATP-binding cassette
ACE	Angiotensin-converting enzyme
AHA/ASA	American Heart Association/American Stroke Association
AJ	Adherens junction
Aplnr	Apelin receptor
ATAC-seq	Assay for transposase-accessible chromatin sequencing
ATP	Adenosine triphosphate
AVM	Arteriovenous malformations
Aβ	Amyloid β
BBB	Blood-brain barrier
BM	Basement membrane
bp	base pair
BSA	Bovine serum albumin
CAA	Cerebral amyloid angiopathy
CADASIL	Cerebral autosomal dominant arteriopathy with subcortical infarcts and leukoencephalopathy
CARASIL	Cerebral autosomal recessive arteriopathy with subcortical infarcts and leukoencephalopathy
CBF	Cerebral blood flow
CCM	Cerebral cavernous malformation
Cdh	Cadherin
Cldn	Claudin
CNS	Central nervous system
CPM	Counts per million
CSVD	Cerebral small vessel disease
CT	Computerized Tomography

CTA	Computerized Tomography Angiography
DAPI	4′,6-diamidino-2-phenylindole
dATP	Deoxyadenosine triphosphate
DMEM	Dulbecco's Modified Eagle Medium
DMR	Differentially methylated region
DMSO	Dimethyl sulfoxide
DNA	Deoxyribonucleic acid
dNTP	Deoxyribonucleotide triphosphate
DPBS	Dulbecco’s phosphate buffered saline
EC	Endothelial cell
ECM	Extracellular matrix
EDTA	Ethylenediaminetetraacetic acid
EGTA	Ethylene glycol tetraacetic acid
ESAM	Endothelial selective adhesion molecule
FACS	Fluorescence-activated cell sorting
FCS	Fetal calf serum
FFP	Fresh frozen plasma
GFP	Green fluorescence protein
GPCR	G-protein coupled receptor
GWAS	Genome-wide association study
H2B	Histone 2B
H&E	Hematoxylin-eosin
Htra	High-temperature requirement A
IA	Intracranial aneurysm
ICAM	Intercellular cell adhesion molecule
ICH	Intracerebral hemorrhage
JAM	Junction adhesion molecule
JACOP	Junction-associated coiled-coil protein

MAGUK	Membrane-associated guanylate kinase
MAPK	Mitogen-activated protein kinase
MEM	Minimum essential medium
Mfsd2a	Major facilitator super family domain containing 2a
MMP	Matrix metalloproteinase
MPP	Membrane palmitoylated protein
mRNA	Messenger RNA
MRI	Magnetic resonance imaging
MRP	Multidrug-resistant protein
MRTF	Myocardin-related transcription factor
NAD	Nicotinamide adenine dinucleotide
NADPH	Nicotinamide adenine dinucleotide phosphate hydrogen
N-Cadherin	Neuronal cadherin
NDR	Nucleosome depleted region
NO	Nitric oxide
NOS	Nitric oxide synthase
NVU	Neurovascular unit
PBS	Phosphate buffered saline
PCA	Principal component analysis
PCC	Prothrombin complex concentrate
PCR	Polymerase chain reaction
PFA	Paraformaldehyde
Pgp	P-glycoprotein
PIC	Protease inhibitor cocktail
PKC	Protein kinase C
RAAS	Renin-angiotensin-aldosterone system
RNA	Ribonucleic acid
RNA-seq	RNA sequencing

ROS	Reactive oxygen species
RRBS	Reduced representation bisulfite sequencing
RVCL	Retinal vasculopathy and cerebral leukodystrophy
sd	Standard deviation
SDS	Sodium dodecyl sulphate
se	Standard error of the mean
SLC	Solute carrier
SMART	Switching mechanism at the 5′ end of the RNA transcript
SNP	Single nucleotide polymorphism
SRF	Serum response factor
STICH	Surgical Trial in Intracerebral Hemorrhage
SVD	Small vessel disease
TCF	Ternary Complex Factors
TGF-β	Transforming growth factor β
TIMP	Tissue inhibitor of metalloproteinase
TJ	Tight junction
TJP	Tight junction protein
TPM	Transcripts per million
VASP	Vasodilator-stimulated phosphoprotein
VCAM	Vascular cell adhesion molecule
VE-Cadherin	Vascular endothelial cadherin
VEGF	Vascular endothelial growth factor
WGBS	Whole-genome bisulfite sequencing
ZO	Zonula occludens

Appendix C

List of Figures

Appendix D

List of Tables

Appendix E

Supplementary Data

Supplementary table 1	List of animals used in the project and the information about the samples. (CD attachment)
Supplementary table 2	Normalized counts of the transcripts in each of the 30 samples. (CD attachment)
Supplementary table 3	List of differentially expressed genes in 6 months vs. 2 months old samples based on the DESeq2 analysis. (Sheet 1) List of differentially expressed genes when only male mice were used. (Sheet 2) List of differentially expressed genes when only female mice were used. (Sheet 3) List of differentially expressed genes when both male and female mice were used. (CD attachment)
Supplementary table 4	List of differentially expressed genes in 12 months vs. 2 months old samples based on the DESeq2 analysis. (Sheet 1) List of differentially expressed genes when only male mice were used. (Sheet 2) List of differentially expressed genes when only female mice were used. (Sheet 3) List of differentially expressed genes when both male and female mice were used. (CD attachment)
Supplementary table 5	List of differentially expressed genes in 18 months vs. 2 months old samples based on the DESeq2 analysis. (Sheet 1) List of differentially expressed genes when only male mice were used. (Sheet 2) List of differentially expressed genes when only female mice were used. (Sheet 3) List of differentially expressed genes when both male and female mice were used. (CD attachment)
Supplementary table 6	List of differentially expressed genes in 24 months vs. 2 months old samples based on the DESeq2 analysis. (Sheet 1) List of differentially expressed genes when only male mice were used. (Sheet 2) List of differentially expressed genes when only female mice were used. (Sheet 3) List of differentially expressed genes when both male and female mice were used. (CD attachment)
Supplementary table 7	List of differentially expressed genes based on the linear regression analysis of the RNA-seq data. (Sheet 1) List of all the differentially expressed genes. (Sheet 2) List of 1388 genes that are significantly dysregulated with age (p.value.age.fdr < 0.05). (CD attachment)

Supplementary table 8	List of differentially methylated regions based on the linear regression analysis of the RRBS data. (Sheet 1) List of all the differentially methylated regions. (Sheet 2) List of top 1000 differentially methylated regions arranged according to the increasing values of fdr. (CD attachment)
Supplementary Table 9	List of peaks showing differential chromatin accessibility with age. (Sheet 1) List of peaks distributed into 6 clusters based on patterns of age-dependent changes in chromatin accessibility. (Sheet 2) List of peaks distributed into 2 clusters based on patterns of age-dependent changes in chromatin accessibility. (CD attachment)
FACS sorting data	This folder consists of FACS profiles and settings used in the sorting of ECs from all the samples. (CD attachment)